

# **A Piezoelectric Ultrasonic Micro-Motor for *In Vivo* Micro-Robots**

by

Brett Watson

Submitted in partial fulfilment of the requirements of  
the degree of  
Doctor of Philosophy

Supervisors: Prof. James Friend and Assoc. Prof. Leslie Yeo



Department of Mechanical and Aerospace Engineering  
MONASH UNIVERSITY

August 2010

## Copyright © 2010 Brett Watson

All rights reserved. No part of the publication may be reproduced in any form by print, photoprint, microfilm or any other means without written permission from the author.

Under the Copyright Act 1968, this thesis must be used only under the normal conditions of scholarly fair dealing. In particular no results or conclusions should be extracted from it, nor should it be copied or closely paraphrased in whole or in part without the written consent of the author. Proper written acknowledgement should be made for any assistance obtained from this thesis.

I, Brett Watson, certify that I have made all reasonable efforts to secure copyright permissions for third-party content included in this thesis and have not knowingly added copyright content to my work without the owner's permission.

*To my dearest Sarah. Without you, it would not have been possible.*

# Contents

<b>Abstract</b>	<b>vii</b>
<b>Acknowledgements</b>	<b>xi</b>
<b>1 Introduction</b>	<b>1</b>
1.1 A Need for <i>In Vivo</i> Micro-Robots . . . . .	1
1.2 The DNA of an <i>In Vivo</i> Micro-Robot . . . . .	4
1.3 Micro-motor Requirements . . . . .	5
1.4 Background on Micro/Milli-Scale Actuators . . . . .	6
1.5 Research Goals . . . . .	26
1.6 Thesis Outline . . . . .	28
<b>2 Proof of Concept</b>	<b>31</b>
<b>3 Modelling of Stator Resonant Frequencies</b>	<b>41</b>
<b>4 Piezoelectric Motor for an <i>In Vivo</i> Micro-Robot</b>	<b>55</b>
<b>5 Conclusions and Future Work</b>	<b>92</b>

5.1	Conclusions . . . . .	92
5.2	Future Work . . . . .	95
	<b>Bibliography</b>	<b>98</b>
<b>A</b>	<b>Publications</b>	<b>103</b>
A.1	List of Publications . . . . .	103
A.2	ICQNM – Paper . . . . .	105
A.3	ICRA – Paper . . . . .	111
<b>B</b>	<b>Supplementary Material for Chapter 4</b>	<b>118</b>

## Abstract

A need for improvement in minimally invasive surgical techniques is well documented. A method of achieving this improvement is through the development of a tetherless micro-robot capable of conducting medical procedures *in vivo*. Such a device could circumvent many of the problems associated with current minimally invasive procedures, and ultimately, may carry out procedures previously impossible and open up new areas of treatment.

A key obstacle that must be overcome in the development of such a device is the realisation of a motor capable of acting as the drive system. Such a motor needs to be approximately  $200\text{ }\mu\text{m}$  in diameter, produce a start-up torque in excess of  $15\text{ nNm/mm}^2$ , and produce an output power of more than  $65\text{ }\mu\text{W/mm}^2$ . Existing micro-motors have separately met the geometric or performance requirements, but never both.

In this thesis, we report a design methodology that results in a piezoelectric ultrasonic resonant micro-motor that, for the first time, effectively meets these requirements. The design methodology of the motor uses the piezoelectric element as a vibration generator, rather than as an integral part of the stator design. This simplifies the design, resulting in a reduction in size compared with existing micro-motor designs. The application of this methodology requires a stator de-

sign that can produce an elliptical stator tip motion from a single excitation source through resonant frequency matching. The design of such a stator is achieved through the development of three novel modelling techniques, which facilitate an understanding of how the system geometric parameters affect the resonant frequencies of interest, and affect the generation of the desired elliptical stator tip motion.

The resulting motor has a stator dimension of  $241\text{ }\mu\text{m}$  and an overall diameter of  $400\text{ }\mu\text{m}$ , the larger dimension resulting from the commercial availability of magnetic elements. The peak measured start-up torque was  $230.4\text{ nNm/mm}^2$ , with a peak output power of  $72.4\text{ }\mu\text{W/mm}^2$ . This exceeded the requirements for torque and power to drive a tetherless micro-robot by 15-times and 10%, respectively. By overcoming the challenge of the drive system design, this work has opened up the opportunity to progress to the next stage of research in *in vivo* micro-robotics, full prototype development.

## General Declaration

In accordance with Monash University Doctorate Regulation 17/ Doctor of Philosophy and Master of Philosophy (MPhil) regulations the following declarations are made:

I hereby declare that this thesis contains no material which has been accepted for the award of any other degree or diploma at any university or equivalent institution and that, to the best of my knowledge and belief, this thesis contains no material previously published or written by another person, except where due reference is made in the text of the thesis.

This thesis includes two original papers published in peer reviewed journals, one original paper accepted by, and one original paper submitted to, peer reviewed journals, two international conference papers and two provisional patents. The core theme of the thesis is the realisation of a micro-motor capable of being used as the drive system of an *in vivo* tetherless micro-robot. The ideas, development and writing of all the papers in the thesis were the principle responsibility of myself, the candidate, working within the Department of Mechanical and Aerospace Engineering under the supervision of Professor James Friend and Associate Professor Leslie Yeo.

The inclusion of co-authors reflects the fact that the work came from active collaboration between researchers and acknowledges input into team-based research.

In the case of Chapters 1 – 4 my contribution to the work involved the following:



Thesis Chapter	Publication Title	Publication Status	Nature and extent of contribution
1	Piezoelectric ultrasonic micro/milli-scale actuators	Published	I was chief investigator, responsible for the initiation, research, interpretation and writing of the paper
2	Piezoelectric ultrasonic resonant motor with stator diameter less than 250 $\mu\text{m}$ : the <i>Proteus</i> motor	Published	I was chief investigator, responsible for the initiation, design, modelling, experimental work, results interpretation and writing of the paper
3	A study on axial and torsional resonant mode matching for a mechanical system with complex non-linear geometries	Published	I was chief investigator, responsible for the initiation, all modelling, experimental work, results interpretation and writing of the paper
4	Modelling and testing of a piezoelectric ultrasonic micro-motor suitable for <i>in vivo</i> micro-robotic applications	In review	I was chief investigator, responsible for the initiation, design, all modelling, experimental work, results interpretation and writing of the paper

I have not renumbered sections of submitted or published papers, however, additional page numbers have been provided in order to generate a consistent presentation within the thesis.

---

Brett Watson

August 5, 2010

## Acknowledgements

I would like to begin by thanking my supervisors Professor James Friend and Associate Professor Leslie Yeo for taking a chance and giving me the opportunity to work on such an exciting project. I doubt many other students have traversed a greater range of highs, lows and experiences than I have in the past three years, and because of this, what I have learnt from you both will be invaluable whatever I may do in the future.

I would like to thank all of the people who have been a part of the Micro-Nanophysics Research Laboratory during my candidature. They have not only given me invaluable help during the course of my research, but also helped keep me sane. Thank you; Aisha, Anushi, Cheol-Ho, Daniel, Devendra, Dinakar, Geoff, Greg, Haiyan, Jeremy, Mar, Mike, Ming, Nick, Nicole, Priscilla, Richie, Ricky, Rohan and Sasi. Specifically, I thank Geoff for working in tandem with me on the bane of my existence of the last couple of years, the assembly methodology of the motors, Cheol-Ho for his technical expertise and experience, which unfortunately I only had the benefit of for the last six months, and Sasi for our enlightening conversations about the world of academia and research in general.

Outside of my research group I would like to give my greatest appreciation to

Ben Johnston of Laser Micromachining Solutions at Macquarie University. Your talent, persistence and efficiency is a significant part of the reason the motor could go from design to prototype. I would also like to thank Associate Professor Metin Sitti from Carnegie Mellon University for his collaboration on this project. I gained a lot through my visit to your laboratory and by attending ICRA 2009 with you. From your group, I'd like to thank Steven, Chytra and Paul for their help on the determination of the magnetic preload force.

My very special thanks goes to my immediate and extended family. Your support and help have been more than I could ask for and has had a profound impact on my ability to complete this work.

Finally and most importantly, my love and undying gratitude to my dearest Sarah. Your love, support, patience and motivation is the main reason I could even consider undertaking PhD let alone be able to complete it. You are amazing, and as I have promised, the next three years are yours.

Brett Watson

August 5, 2010

# Introduction

*In this chapter, we describe the need for motors that are suitable for in vivo applications. Specifically, we focus on micro-robots that are capable of tetherless motion within the human body and the requirements of motors suitable to drive them. A review of existing motor designs demonstrates that no suitable motor exists for this application and that the piezoelectric ultrasonic class of motor shows the greatest potential to meet the need. This leads to the development of the thesis aim: to demonstrate that through changing the design methodology of current piezoelectric ultrasonic motors we can realise a motor with a geometry and performance suitable to drive a tetherless in vivo micro-robot. The chapter concludes with an outline of the thesis.*

## 1.1 A Need for *In Vivo* Micro-Robots

The United Nations Department of Economic and Social Affairs Population Division has reported that the worldwide population of people older than 60 years will exceed the number of people younger than 15 years for the first time in history by 2050 [1]. More immediately, between 1985 and 1997, the population prevalence of overweight children in Australia increased by 60–70%, with obesity increasing two to four-fold [2]. Such changes to the population will potentially

increase the number [3] and procedural time [4] of surgeries carried out in the coming decades, placing a large strain on the health care system of many nations.

One method to reduce this strain is the increased use of minimally invasive surgery (MIS). MIS is a revolutionary surgical technique [5] performed using viewing apparatus and instruments inserted through small incisions. This contrasts traditional cut and sew techniques which use large incisions to expose the entire operation site to the surgeon. Key benefits of MIS are the reduction in trauma, pain and recovery time for the patient [5–7], resulting in reduced hospital stays [8] that will alleviate some of the increased demand for hospital resources that comes with the described population shifts.

However, the reduced access afforded by the small incisions associated with MIS limit perception, reduce dexterity, and increase strain for the surgeon, whilst also increasing the likelihood of error [9–11]. The operating area is viewed using counter intuitive two-dimensional video displays [10], imposing a significant limitation on vision, with the field of view not encompassing the frequent changes in instrument [12]. A reduction in dexterity is caused by: controlling long instruments from the proximal part outside the body [13], motion limited to four degrees-of-freedom [5], and limitations due to the invariant point of insertion or fulcrum [10]. These have led to accidental injury to organs and vascular structures, whilst limiting the complexity of procedures that can be carried out [12].

To overcome this, researchers are working towards a tetherless micro-robot (microbot) capable of conducting medical procedures within the human body. Initially, these microbots could provide an improved field of view for the surgeon enabling more accurate tool insertion and placement [12] during current

MIS procedures. Further developments may completely eliminate the need for incisions, leading to improved dexterity and reduced fatigue for the surgeon [6].

Ultimately, *in vivo* micro-scale devices have the potential to enable the undertaking of procedures previously impossible due to obesity [14], age [15] or illness [16]. Moreover, the capability to access parts of the body impossible with current medical instruments [6, 17], will pave the way for a range of new procedures involving localised treatments.

A need for access to permit localised treatments has been demonstrated in a range of medical areas: powerful drugs have been developed to cure or benefit some forms of cancer, but with an undesirable toxicity to normal tissue [18]; rapid screening of novel proteins and peptides has been achieved with current genomic and proteomic technologies, however the delivery systems remain a challenge [19]; and invasive procedures are still required to introduce genetic material to the myocardial tissue of the heart as part of gene transfer strategies as current catheters are unsuitable [20].

Non-surgically tetherless microbots also have the benefit of potentially being remotely operated. This coupled with ease of transportation and use, would enable procedures using these devices to be carried out without the need for patients to undergo transport [6]. This would also enable a wider dissemination of medical technology, whether to zones of conflict, isolated areas, or areas of great poverty.

Taking advantage of the benefits of medical microbots will ensure a wider and improved use of MIS, leading to a reduction in hospital stay times for many patients. This ultimately will reduce the growing pressure on the hospital systems

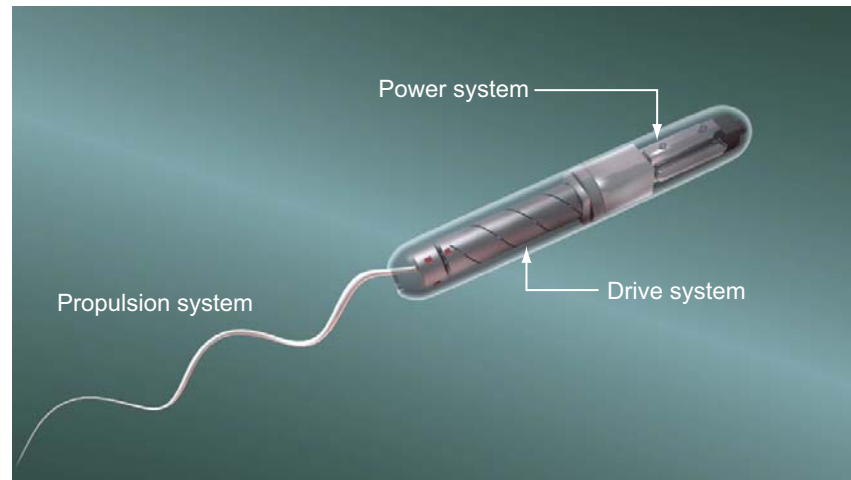


Figure 1.1: The key components of a tetherless *in vivo* micro-robot.

of the world.

## 1.2 The DNA of an *In Vivo* Micro-Robot

To work effectively inside the human body, tetherless *in vivo* microbots must be sub-millimetre in diameter, be able to move rapidly and accurately with a low power consumption, and be easy for the surgeon to control. The key components of such a device are the power system, the propulsion system and the drive system, as shown in Figure 1.1.

Propulsion systems that may be suitable for microbots have been proposed, with some good results achieved. In general, the designs have focussed on propulsion systems that in some way mimic the flagella propulsion of bacteria [21, 22]. Research into power systems for such devices has also been progressed [23] with the most recent research examining the possibility of wireless power transfer [24, 25]. However, as we will outline in Sections 1.3 and 1.4, what has not been achieved is a motor that meets the performance and dimensional requirements

required to drive a tetherless *in vivo* microbot.

In this thesis the challenge of producing a motor that can meet these requirements is addressed. The primary goal of the research is to overcome existing hurdles in micro-motor design and fabrication through an in-depth examination of past designs, the identification and application of a new design methodology, resulting in the fabrication and testing of a motor suitable for use in a tetherless *in vivo* microbot.

### 1.3 Micro-motor Requirements for *In Vivo* Micro Robots

In his PhD thesis [26], Liu presented an analysis on the size and performance requirements of a micro-motor being used to power a tetherless *in vivo* microbot. In the analysis, Liu examined the constraints on the microbot geometry, the blood viscosity and velocity profiles the microbot has to overcome, and the power and torque needed to drive a propulsion system. In Table 1.1 we summarise his findings and outline the approximate minimum requirements for a microbot to move upstream in an arterial tree.

The key parameters of interest in Table 1.1 are the design diameter,  $200\ \mu\text{m}$ , and the normalised torque and power. The only practical motor class that has achieved a diameter of this scale previously are electrostatic motors, as demonstrated by the design by Mehregany et al [27]. However, such motors have a very low torque output with a value on the order of  $1\ \text{nNm}/\text{mm}^2$  [27]. The performance requirements have been met by small scale electromagnetic motors, such as the commercially available Faulhaber Series 0203B that has performance figures in the range of  $3\ \mu\text{Nm}/\text{mm}^2$  and  $24\ \text{mW}/\text{mm}^2$ . However, with a diameter



Table 1.1: Performance requirements of a micro-motor driving a microbot in an artery and associated calculation parameters from [26]. The work approximates the minimum requirements for a microbot to move upstream in an arterial tree. (\* Diameter to access anterior cerebral arteries)

Parameter	
Diameter* ( $\mu\text{m}$ )	200
Analysis Diameter (mm)	1
Analysis Length (mm)	5
Motor density–steel ( $\text{kg}/\text{m}^3$ )	7800
Blood density ( $\text{kg}/\text{m}^3$ )	1050
Blood viscosity (Pa.S)	$4 \times 10^{-3}$
Microbot velocity (cm/s)	-15
Microbot acceleration ( $\text{cm}/\text{s}^2$ )	0
Blood acceleration ( $\text{cm}/\text{s}^2$ )	8/-3
Reynolds Number	40
Torque/cross-sectional area ( $\text{nNm}/\text{mm}^2$ )	15
Power/cross-sectional area ( $\mu\text{W}/\text{mm}^2$ )	65

of 2 mm it is too large for this application. We will more fully discuss motor classes and performance in Section 1.4.

## 1.4 Background on Design Methodologies of Micro/Milli-Scale Actuators

In this section, we reproduce a review on small scale actuators that was undertaken to determine which class of motor is best suited for use in a tetherless *in vivo* microbot. The underlying physics of electromagnetic, electrostatic, thermal, osmotic, electro-conjugate fluid and piezoelectric ultrasonic motor classes were all examined, with the key area of investigation being the *driving force*: the force that is produced by the stator and that induces motion in the rotor. From the investiga-

tion, it was determined that piezoelectric ultrasonic motors showed the greatest potential for use in applications that require a volume of less than  $1 \text{ mm}^3$ , such as an *in vivo* microbot.

Through further investigation of the common characteristics and the driving force of existing piezoelectric ultrasonic micro/milli-scale actuator designs, it was possible to create a new actuator classification system. An examination of the motor classes, structured using the classification system, revealed the benefits and disadvantages of each of the existing classes of piezoelectric ultrasonic motors, whilst revealing areas of limited research.

The review showed that the largest and most researched area is that of motors that use some form of resonant bending mode to create a standing wave in the stator. These designs have a large stator tip displacement, associated with the low harmonic bending modes of operation, which results in high torque–low speed performance characteristics. They also, in general, require complex stators to be fabricated from a piezoelectric ceramic that has made meeting the geometric requirements of an *in vivo* microbot thus far unobtainable for this class of motor. We also note that the standing wave ultrasonic displacement class and those motors that use a propagating wave, although suitable for many applications, are not suitable for use in sub-millimeter applications due to their complex designs. Moreover, it was observed that motors using torsional motion include some very important piezoelectric ultrasonic motor designs [28], however, no small scale actuator has been produced using this design class. The investigation concluded that a piezoelectric ultrasonic resonant micro-motor with a volume and performance capable of meeting the requirements for an *in vivo* microbot has not yet

been reported.

We hypothesise that the underlying reason for this is the design methodology of current piezoelectric ultrasonic resonant motor designs. In general, existing designs from all classes fabricate the stator of the motor from the piezoelectric ceramic. This potentially has a performance benefit by ensuring maximum use of the converse piezoelectric effect, however, fabricating a complex shape from a piezoelectric ceramic becomes significantly more complex as scales decrease. In addition, the use of multiple electrical inputs, as required by most designs, further increases the complexity of the system, lessening the chance of achieving the required dimensions.

# Piezoelectric Ultrasonic Micro/Milli-Scale Actuators

**Brett Watson**, James Friend and Leslie Yeo

*Sensors and Actuators A:Physical*

152, 219–233 (2009)

Copyright © 2009 Elsevier B.V.

DOI: 10.1016/j.sna.2009.04.001

## Declaration for Thesis Chapter 1

### Declaration by candidate

In the case of Section 1.4, the nature and extent of my contribution to the work was the following:

Nature of contribution	Extent of contribution (%)
I was chief investigator for this work. I was responsible for the literature review, the interpretation of the findings, the development of the classification system and the writing of the paper.	80

The following co-authors contributed to the work.

Name	Nature of contribution
Professor James Friend	Overall supervision, review of drafts and submission of paper to journal.
Associate Professor Leslie Yeo	Overall supervision and review of drafts.

	Date
Candidate's Signature	

### Declaration by co-authors

The undersigned hereby certify that:

- (1) the above declaration correctly reflects the nature and extent of the candidate's contribution to this work, and the nature of the contribution of each of the co-authors.
- (2) they meet the criteria for authorship in that they have participated in the conception, execution, or interpretation, of at least that part of the publication in their field of expertise;
- (3) they take public responsibility for their part of the publication, except for the responsible author who accepts overall responsibility for the publication;
- (4) there are no other authors of the publication according to these criteria;
- (5) potential conflicts of interest have been disclosed to (a) granting bodies, (b) the editor or publisher of journals or other publications, and (c) the head of the responsible academic unit; and
- (6) the original data are stored at the following location(s) and will be held for at least five years from the date indicated below:

Location(s)	Department of Mechanical and Aerospace Engineering, Monash University, Clayton, Victoria, Australia.
-------------	--

	Date
Signature 1	
Signature 2	



## Review

## Piezoelectric ultrasonic micro/milli-scale actuators

B. Watson, J. Friend\*, L. Yeo

Monash University, Department of Mechanical and Aerospace Engineering, Micro/Nanophysics Laboratory, Clayton, VIC 3800, Australia

## ARTICLE INFO

## Article history:

Received 7 October 2008

Received in revised form 13 March 2009

Accepted 2 April 2009

Available online 10 April 2009

## PACS:

07.10.Cm

85.50.-n

43.35.+d

89.75.Da

## Keywords:

Piezoelectric

Micro-actuator

Micro-motor

Ultrasonic

Review

## ABSTRACT

A growing demand for actuators with a volume of less than  $1\text{ mm}^3$  has driven researchers to produce a varied range of micro/milli-scale designs. By examining the underlying physics of the actuator operation we are able to demonstrate why piezoelectric ultrasonic actuators have the greatest potential to meet this need. Moreover, it allows us to create a new classification system for piezoelectric ultrasonic actuators, affording us a better understanding of the core characteristics of each class of actuator, which class is most suited to various applications, and highlights potential areas of future research.

© 2009 Elsevier B.V. All rights reserved.

## Contents

1. Introduction.....	219
2. Commonalities of piezoelectric ultrasonic micro/milli-scale actuators.....	221
3. Piezoelectric ultrasonic actuator classification.....	222
4. Standing wave piezoelectric ultrasonic micro/milli-scale actuators.....	222
4.1. Rotational actuators.....	222
4.1.1. Flexural mode actuators.....	222
4.1.2. Bending mode actuators.....	223
4.1.3. Torsional mode actuators.....	226
4.2. Linear actuators.....	228
5. Propagating wave actuators.....	228
5.1. Rotational actuators.....	229
5.2. Linear actuators.....	231
6. Ultrasonic displacement actuators.....	231
7. Actuator performance classification.....	232
8. Future research areas.....	232
References.....	232
Biographies.....	233

## 1. Introduction

There is growing demand for actuators with a volume of less than  $1\text{ mm}^3$ . This need has been reported across the micro-robotics

industry [1] and the medical profession [2,3]. Despite such varied fields of use, the core characteristics required of actuators at millimetre and sub-millimetre scales are the same. Actuators at these scales require high output forces, accuracy, low response times, a simple design and simple operation. An understanding of how well myriad actuator classes may meet these requirements can be determined by examining the underlying physics of the actuator operation. The key focus of such an investigation is the force that is

\* Corresponding author.

E-mail address: [James.Friend@eng.monash.edu.au](mailto:James.Friend@eng.monash.edu.au) (J. Friend).

**Table 1**  
Comparative scaling of motor driving forces ( $F$  is output force,  $L$  is characteristic length).

Motor class	Driving force	Scaling
Electromagnetic	Electromagnetic	$F \propto L^4$
Electrostatic	Electrostatic	$F \propto \frac{1}{L^2}$
Thermal	Mechanical strain	$F \propto L$
Osmotic	Osmotic effect	Dependent on many variables
ECF	ECF	$F \propto \frac{1}{L}$ minimum
Piezoelectric ultrasonic	Converse piezoelectric effect	$F \propto L$

used as the basis of design. This is the force that is produced by the stator and induces motion in the rotor/slider; hereafter referred to as the driving force.

Electromagnetic actuators are the most widely used of any design at the macro-scale, with small-scale versions also having been developed [4,5]. The driving force for an electromagnetic actuator relies on the interaction of the permanent magnets of the rotor, and the magnetic field induced by the current in the coil of the stator. The use of this non-destructive, non-contact force gives the electromagnetic actuator a high energy density, which compares favorably with most other actuator designs and has led to its wide spread use. However, as detailed in Table 1, the electromagnetic force poorly scales down [6] and the relative performance of an electromagnetic actuator becomes progressively worse as the length scale reduces to the order of millimetres. Moreover, due to the reduction in scale the electromagnetic driving force promotes an undesirable high speed, low force behaviour in the actuator. We concluded from this that the driving force that makes an electromagnetic actuator superior to most actuators in large-scale applications likewise makes it unsuitable as the actuator volume is reduced to the desired 1 mm<sup>3</sup>.

The simple design of the electrostatic actuator has enabled researchers to produce actuators with diameters as small as 100 µm [7] and beyond [8], making them among the smallest practical actuators produced. This small size has led to some success in the field of micro-electro-mechanical systems (MEMS) [9], where size is of critical importance. As with electromagnetic actuators, electrostatic actuators use a non-contact force to create mechanical work. The force arises from the interaction between charged materials, and decreases with the square of the distance between the two charged bodies. The excellent scalability of the electrostatic force (the force increases with a reduction in size, see Table 1), is a major design advantage, and has allowed the development of the very small-scale actuators previously noted. However, the electrostatic driving force also leads to the disadvantages associated with these designs. Most importantly, the electrostatic driving force is weak when compared with many other forces used for actuation and in spite of excellent scaling characteristics, limits the output of electrostatic actuators. At the scales noted previously, the output torque is currently limited to approximately 10 pNm [7]. The electrostatic driving force also results in a nonlinear output for the actuator. This is particularly problematic at the end of the output range, where actuators can undergo 'snap-down'. Moreover, the electrostatic driving force is very sensitive to the operating environment and actuator design. The maximum electrostatic field strength is strongly dependent on humidity and ambient gas content and the force performs best with actuator designs with low aspect ratios (large electrode surface compared to distance to travel). These deficiencies are less important for many MEMS applications, but limit the actuator's use in most other areas.

Thermal actuators are another actuator design that have been employed in MEMS applications [10,11]. This type of design can be produced at scales comparable to electrostatic actuators, but have output forces in the order of micro-Newtons. In contrast to electromagnetic and electrostatic actuators, thermal actuators use

a mechanical strain, rather than a non-contact force, as a driving force. Mechanical strain rates greatly vary depending on the type of material used, with smart memory alloys (SMAs) having significantly higher strain rates than regular metallic alloys. Regardless of the material used, the output can be magnified through clever geometric design with the actuator performance scaling linearly due to the inherent thermal characteristics. Although the thermally induced mechanical strain of these designs produces a high output force and scales well, actuators that use this driving force have two significant disadvantages. The first is that the driving force used results in a response time that is very slow when compared to alternatives, also affecting the actuator velocities obtained from the designs. The second is that the lifespan of the actuator may be limited due to the plastic strain arising from repeated cycling. With such characteristics, thermal actuators are most suited to applications that require large forces infrequently, such as micro-grippers.

Osmotic actuator designs utilise a different approach to creating motion [12] than those actuator classes already covered. The removal of the need for an electrical input is advantageous for some operating conditions and the design has obvious benefits for use with microfluidics. The driving force of an osmotic actuator is the increase in pressure within a vessel, leading to an expansion of an actuation diaphragm. The increased pressure is caused by one-directional flow of liquid across a semi-permeable diaphragm, driven by the osmotic effect. How well an osmotic actuator can be scaled is dependent on many factors, including the diaphragm material used and the concentration of the osmotic agent. Osmotic actuators have numerous disadvantages when applied to a broad spectrum of applications including:

- Slow response times, leading to low actuator velocities.
- Complex designs required obtain large, linear or rotational outputs.
- Problems with solute deposition, fouling and control.

Such drawbacks demonstrate that osmotic actuators are unsuitable for many applications. It is worthy to note however, that like thermal actuators, osmotic actuators have shown potential for use as micro-grippers.

A further somewhat unusual design is the design developed by Yokota et al. [13,14]. The driving force of these motors is the jetting phenomenon induced in an electro-conjugate fluid (ECF) when in the presence of an electric current. The motors use a rotor with vanes to harness the ECF jetting, producing the output rotation. Although the ECF jetting phenomenon is not yet fully elucidated, it has been demonstrated that motors designed using this driving force improve in performance as the scale is reduced [13]. Motors of these designs have good outputs, and excellent scalability, however, there may be difficulties in further reducing the scale of these motors below 1 mm<sup>3</sup> [15].

The first piezoelectric ultrasonic micro/milli-scale actuators evolved from earlier larger scale piezoelectric actuators successfully used in cameras [16]. Since then, numerous small-scale actuators have been produced, including designs with dimensions of only a few millimetres [17] and nanometre positioning accuracy [18]. The driving force of a piezoelectric actuator arises from the converse piezoelectric effect, which converts a harmonic electrical input to a cyclic strain in the piezoelectric element. This driving force scales linearly with the characteristic length scale, potentially allowing useful amounts of work to be produced from small-scale actuators. This is especially true when the actuators are designed to operate near the mechanical resonance of the stator. In addition to good scalability, piezoelectric actuators have numerous other benefits for use as milli/micro-actuators. They include:

- Large output torques
- Direct drive
- No gearbox or brake mechanism required
- Bearingless
- Quick response
- No backlash
- Negligible effects from external magnetic fields
- Simple design
- Low voltages

The drawback of current piezoelectric ultrasonic resonant actuators include a significant performance loss if a deposited piezoelectric material is used for very small scales (see actuators produced by Morita et al. as an example [20,21]) and the potential complexity of the control system due to multiple input signals required by most designs.

The underlying physics of the actuator operation demonstrates that piezoelectric ultrasonic actuators have the greatest potential to meet the core requirements of an actuator design as devices are reduced in scale below  $1\text{ mm}^3$  in volume.

This paper reviews piezoelectric ultrasonic actuators that have made significant steps towards reaching the goal of a true micro-motor. In addition, we introduce a classification system that forms the structure of our review. By using the underlying physics of the actuator design as the basis for the classification, we are able to encompass previously proposed classification systems [22,23], whilst promoting a better understanding of the core characteristics of the proposed design. Moreover, the use of such a classification system aids in determining which piezoelectric ultrasonic actuator class is best suited to various applications and highlights potential areas of future research.

## 2. Commonalities of piezoelectric ultrasonic micro/milli-scale actuators

The focus of this paper is to review piezoelectric ultrasonic micro/milli-scale actuators by examining the differences in their underlying physics of operation. To enable this to be completed successfully, it is prudent to first cover the commonalities shared by all piezoelectric ultrasonic actuators.

The first and most important of these is that piezoelectric materials are the basis for all piezoelectric ultrasonic resonant actuators. The piezoelectric element in actuators may be used in bulk form as the stator [24], as a method to induce vibration in the stator [18], or in a deposited form [21].

Piezoelectricity, from the Greek *piezein*, means squeeze or pressure electricity. The general definition of piezoelectric materials is that they develop an electric charge differential along an axis of piezoelectric polarisation if placed under appropriate mechanical strain (direct piezoelectric effect) and deform if an electric field is applied along the same axis of polarisation (converse piezoelectric effect). Piezoelectric materials may be used to provide static and dynamic deformations, at frequencies up to several gigahertz, depending on the motion to be induced, the scale of the device, and the material used.

As previously noted, actuators make use of the converse piezoelectric effect as a driving force. The converse piezoelectric effect arises when, upon the application of an electric field to a piezoelectric material, a dipole moment is created by the relative motion of the material's atoms. This motion may contract or expand the unit cell, leading to a maximum strain in the piezoelectric element of approximately 1%.

Upon the application of an electric field, for the atom motion to occur the piezoelectric material must be non-centrosymmetric in crystal structure, and be polarised. Non-centrosymmetric

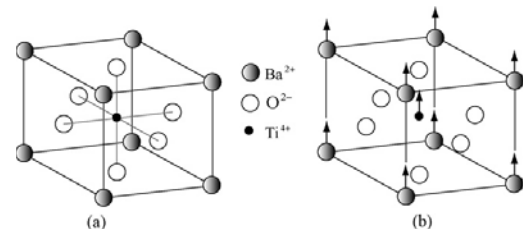


Fig. 1. The (a) centrosymmetric (non-piezoelectric) and (b) non-centrosymmetric (piezoelectric) crystal structure of barium titanate. Note the offset barium and titanium atoms.

refers to the lack of a centre of symmetry in the crystal structure. Materials which are centrosymmetric, when placed under stress, exhibit a symmetrical movement, inhibiting the formation of a mechanical strain. As an example, Fig. 1 shows the centrosymmetric (non-piezoelectric) and non-centrosymmetric (piezoelectric) crystal structure of barium titanate. Most piezoelectric materials are generally not naturally polarised, nor polarised by the fabrication process. To polarise the material, an applied electric field or mechanical strain is used. For an in-depth examination of these materials for use in piezoelectric actuators, see the work by Kenji Uchino [25].

We can also note the generalised operation of a piezoelectric ultrasonic resonant micro/milli-scale actuator is to convert the cyclic motion of the piezoelectric element to a net work at the rotor or slider. This is achieved through a friction coupling between the stator and rotor or slider.

The stator design and the physics harnessed by it during operation are the key things we are to examine in Sections 3 through 6. Here we note that the goal of all stator designs is to produce an elliptical motion at the stator tip (the point of contact between the stator and rotor/slider). As demonstrated by Fig. 2, an elliptical stator tip motion is desirable as it results in the stator imparting both a contact (normal) and driving (tangential) force on the rotor or slider, resulting in the desired stator/rotor output.

In reality, it is very difficult to obtain the idealised motion as illustrated in Fig. 2. It is far more common to keep the stator or rotor in constant contact with the stator. This ensures that the output obtained is repeatable for each stator cycle. The method by which this achieved is known as the friction coupling and is the other key commonality among piezoelectric ultrasonic actuators. The principle of the friction coupling is to ensure that a larger contact force is exerted between the rotor/slider and the stator for one half of the operating cycle than the other half. Using a coulombic friction model, we can see that the cyclic contact force leads to a cyclic frictional force which, when time averaged across one stator cycle, results in a net work at the rotor/slider in a given direction. This leads to a net motion of the rotor or slider. We can see this illustrated in Fig. 3.

To ensure this constant contact force, a preload is used. This is a normal force on the rotor or slider in the opposite direction to that imposed by the stator and is usually a magnetic, weight or spring force.

Although the friction coupling ensures a repeatable output, it is also the area of greatest inefficiency in a piezoelectric ultrasonic actuator. Only a small part of the energy within the stator is converted to a useful net tangential displacement of the rotor. The remaining energy is wasted through the unused motion of the rotor and in heat, caused by friction.



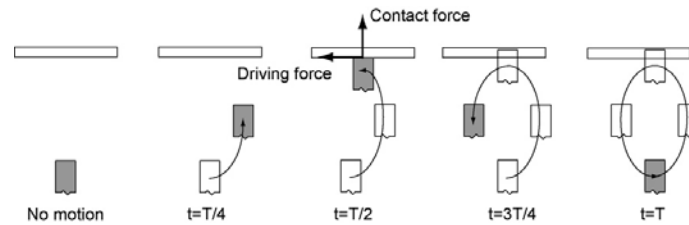


**Fig. 2.** The idealised stator tip motion for one cycle for a piezoelectric ultrasonic actuator. The elliptical stator tip motion enables the stator to impart both a contact (normal) and driving (tangential) force on the rotor or slider, resulting in the rotor/slider being driven through friction. Note:  $T$  is period and  $t$  is cycle time.

### 3. Piezoelectric ultrasonic actuator classification

As noted in Section 2 the key differentiation in the design of piezoelectric ultrasonic actuators is the method by which the stator converts the motion of the piezoelectric elements to the elliptical stator tip motion. By analysing these methods, we can develop a classification system which affords us a clearer understanding of the advantages and disadvantages associated with a specific design, allows a selection of a particular actuator class best suited to an application, and enables better comparison of actuator performances. It may also highlight potential areas of future research needed to meet a specific need. Piezoelectric ultrasonic actuators can be classified according to:

- the type of wave used to promote motion,
- the type of motion being produced by the actuator,
- the vibration mode, if any, being induced in the stator, and
- how vibration modes of the stator are being combined.

Fig. 4 shows a delineation of the different actuators into these classes.

For the remainder of this paper we use this classification system to review existing piezoelectric ultrasonic micro/milli-scale actuators. We describe the different operational principles used within the design of each class, how these relate to the characteristics and performance of the actuator, and highlight examples of each class.

### 4. Standing wave piezoelectric ultrasonic micro/milli-scale actuators

Standing wave actuators make use of resonant vibration modes to elicit the elliptical motion from the stator. This motion may be one [24], or several stator tips [26]. The elliptical motion may be created by coupling different resonant modes (i.e., coupled orthogonal bending, coupled axial and bending, or coupled axial and torsional) through the use of multiple piezoelectric elements or through a combination of resonant mode and geometrical design.

The use of resonant vibration modes as the basis of design for this class of actuator governs the common performance characteristics.

Specifically, the comparatively large outputs achieved by this class of actuators are a result of the amplification of the piezoelectric strain achieved under resonant conditions. The magnitude of this effect varies with the vibration mode used, as we will explore later, and scales linearly with the characteristic length of the piezoelectric element. This accounts for the excellent scalability of these designs. The resonant conditions of the stator also determine the speed of operation. Counter-productively, operating at resonance can reduce the service life of the actuator, requiring additional consideration during design.

#### 4.1. Rotational actuators

##### 4.1.1. Flexural mode actuators

Flexural mode actuators are designed to use a flexural resonant mode of a thin, flat (membrane-like) stator. The stator, in general, is fabricated from or coated with a piezoelectric material, with the resonant mode excited by the direct application of an alternating electric field.

The flexural resonant mode-shape of the membrane-like stator results in a linear stator displacement. To obtain the required elliptical motion from the stator, a geometric addition must be made to the “membrane”. This geometric addition will modify the linear motion of the stator surface to create an elliptical path for the stator tip. An example is the actuator produced by Dubois and Muralt [29], as shown in Fig. 5, which uses ‘elastic fins’ attached at regular positions under the rotor. During the upward phase of the flexural mode in the membrane-like piezoelectric stator, the fins do not slide when pushed by the stator, owing to friction, but bend elastically. Due to the ‘tilt angle’ at which the fins are fixed, this action results in a horizontal movement of the rotor. During the downward phase of the stator, when the friction force is small, the fins relax and follow the rotor.

Although actuators in this class are operated at a resonant mode, the magnitude of displacement in the stator caused by a flexural wave is small. This limits the output that can be produced by such designs. As an example, the design produced by Dubois and Muralt achieved a maximum torque of  $0.94 \mu\text{Nm}$ , from an actuator with a diameter of  $5.2 \text{ mm}$ . The excitation frequency of this mode is also relatively low, leading to comparatively slower rotational speeds.

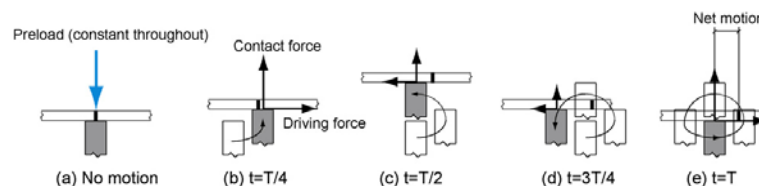


**Fig. 3.** By applying a “preload” to the slider/rotor, it remains in contact during the stator for the complete cycle, ensuring a repeatable output. The elliptical motion now ensures a greater contact (and hence driving force) is applied during part of the cycle (b) and (e), than the other (c) and (d), resulting in a net motion.

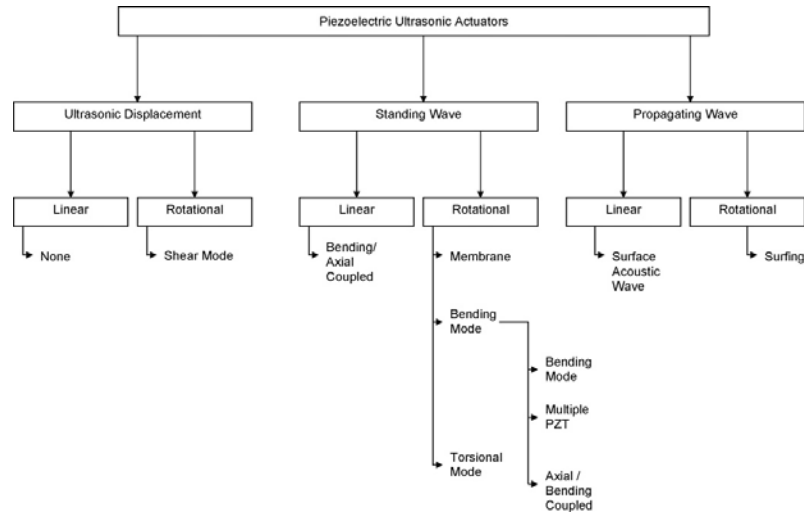


Fig. 4. Classes of piezoelectric ultrasonic milli/micro-actuators as determined by the examination of the underlying physics of actuator operation.

Dubois and Muralt reached a peak rotational velocity of 1020 rpm at an input of 70.6 kHz.

These operational characteristics, derived from the driving force, mean that flexural mode standing wave actuators are well suited to low speed, low output applications where packaging is of primary concern. An example of such an application is in watches, where the flat geometry and reliable motion is more important than the actuator performance.

#### 4.1.2. Bending mode actuators

By far the largest group of piezoelectric ultrasonic micro/milli-scale actuator designs are those that use resonant bending modes. Designs in this class excite a first-order bending mode in combination with another vibration mode to achieve the desired elliptical stator output. This combination may be two orthogonal first-order bending modes, or a first-order bending mode and an unrelated mode (i.e., an axial vibration mode).

First-order bending modes produce the largest stator tip displacement of any mode-shape. This has a direct and beneficial effect on the performance of the actuator, promoting a high torque output for a given size. The use of first-order bending modes also has an effect on the output speed of the design. In general, first-order bending modes are excited at lower frequencies than other modes (i.e., axial or torsional). As such, the operating frequency will be lower, resulting in a lower output rotational velocity than alternative designs.

The most widely researched bending mode designs are those that use orthogonal bending modes to create an elliptical stator tip motion. Known as “wobble motors”, the name is derived from the appearance of the stator during operation. In these designs, the actuator may be driven using one [17] or multiple piezoelectric elements [30].

To demonstrate the wobble motion, we consider a simple beam fabricated from a piezoelectric material, as shown in Fig. 6. The first-order orthogonal bending modes, bending modes 1 and 2, of the beam in Fig. 6 can be isolated by driving the piezoelectric element at the correct frequencies. We assume a harmonic electrical input to the piezoelectric element and no proportion of any other mode effecting the beam motion. If the beam is driven at the natural frequency that excites bending mode 1, the displacement of point A on the stator tip in the x-direction is given by

$$u_x(t) = u_0 \sin(\omega t + \alpha), \quad (1)$$

where  $u_0$  is the magnitude of vibration,  $\omega$  is the frequency of vibration,  $t$  is the time and  $\alpha$  is the phase constant. There is no motion in the y-direction for bending mode 1. Similarly, if we drive the beam at the natural frequency of bending mode 2, the displacement of point A on the stator tip in the y-direction is given by

$$u_y(t) = u_1 \sin(\omega t + \beta), \quad (2)$$

where  $u_1$  is the magnitude of vibration,  $\omega$  is the frequency of vibration,  $t$  is the time and  $\beta$  is the phase constant. There is no motion in the x-direction for bending mode 2. If we now consider these two

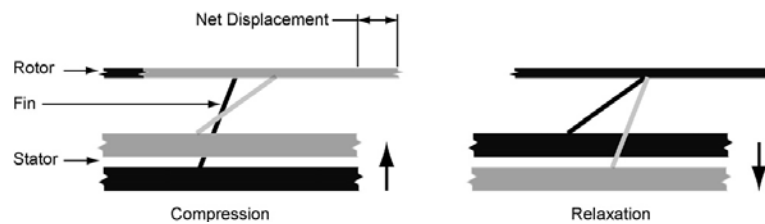
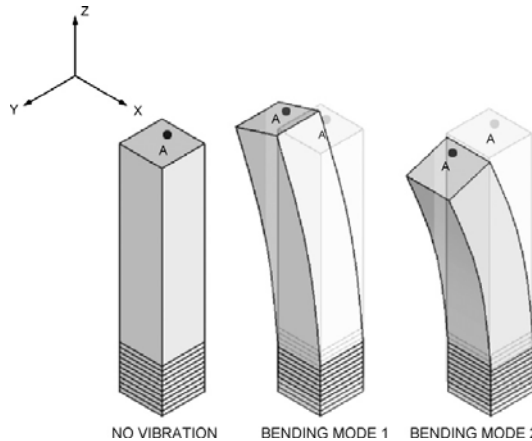


Fig. 5. The membrane actuator by Dubois and Muralt [29] uses ‘elastic fins’ to convert the linear motion of the piezoelectric “membrane” to the desired elliptical motion.

224

B. Watson et al. / Sensors and Actuators A 152 (2009) 219–233



**Fig. 6.** The first-order stator orthogonal bending modes excited during the operation of a bending mode actuator.

bending modes to be excited simultaneously, the motion of point A can be considered to be the combination of Eqs. (1) and (2). Together these equations describe an elliptical path in the  $x$ - $y$  plane.

If we also include the change in position in the  $z$ -direction due to the effects of bending during this excitation, the displacement at point A can further be described by

$$u_z(t) = u_2 \sin(\omega t + \gamma), \quad (3)$$

where  $u_2$  is the magnitude of vibration,  $\omega$  is the frequency of vibration,  $t$  is the time and  $\gamma$  is the phase constant. The path trace of point A can then be sketched as shown in Fig. 7.

The simplest of these designs uses a single piezoelectric stator with multiple electrodes. These multiple electrodes allow two driving signals to be used simultaneously, creating orthogonal bending modes. The actuator is designed to run at the fundamental bending mode of the stator. It is excited by four electrical sources, with  $\pm 90^\circ$  phase shifts. By reversing the phase shifts, the rotation direction can also be reversed.

The first use of this design at the milli-scale was reported by Morita et al. [19]. The design uses a thin-film PZT (9  $\mu\text{m}$ ) deposited by a hydrothermal method on to the surface of a titanium tube, 2.4 mm in diameter and 10 mm in length. Electrodes were then formed

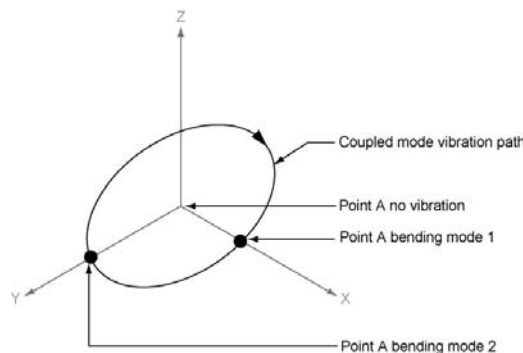


**Fig. 7.** The theoretical trace of the stator tip of a bending mode actuator for one period. The elliptical motion is achieved by coupling orthogonal first-order bending modes.

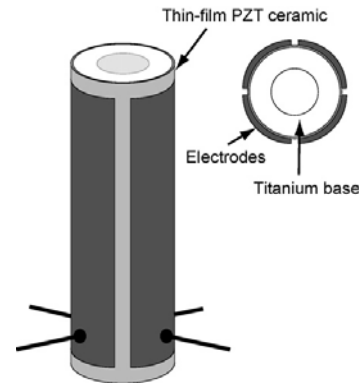


**Fig. 8.** The early bending mode actuator by Morita et al. [19] uses multiple electrical inputs to a cylindrical stator with a thin-film piezoelectric coating, to simultaneously excite orthogonal bending modes. Note the four external electrodes.

in four places on the PZT layer. This is detailed in Fig. 8. The motor achieved bi-directional operation and a peak rotation of 295 rpm with a driving voltage of 20–33  $V_{p-p}$ .

This design was subsequently advanced by Morita et al. in 2000 [21]. The thin-film PZT was increased to 12  $\mu\text{m}$  in thickness, deposited using the hydrothermal method on a titanium base as before. The stator dimensions were reduced to 1.4 mm in diameter and 5 mm in length. The actuator was driven at the first bending mode resonant frequency of the stator of 227 kHz. The maximum rotational velocity was 680 rpm with a maximum torque of 0.67  $\mu\text{Nm}$ .

Morita et al. also modified this design, to produce one of the first micro/milli-scale actuator designs to use a bulk piezoelectric element as the stator. The actuator has a cylindrical stator, 2.4 mm in diameter and 10 mm in length. The stator consists of a bulk cylindrical PZT element, a single cylindrical inner electrode and four outer electrodes, as shown in Fig. 9. The PZT is poled through the thickness from the outside to the inside. The actuator housing holds the stator through rubber O-rings at two nodal positions and the rotor is preloaded by a spring.

The driving frequency for the actuator is 85 kHz, which produced a maximum rotational velocity of 650 rpm. The input voltage was 100  $V_{p-p}$  and the actuator produced a maximum torque of 220  $\mu\text{Nm}$ . The maximum efficiency was 25%, which is excellent for an actuator of this scale. As an example of future applications, the

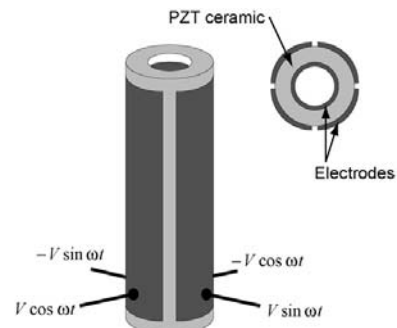


**Fig. 9.** Morita et al. [20] also applied the design from Fig. 8 to a bulk PZT stator. Here the earth electrode is internal.

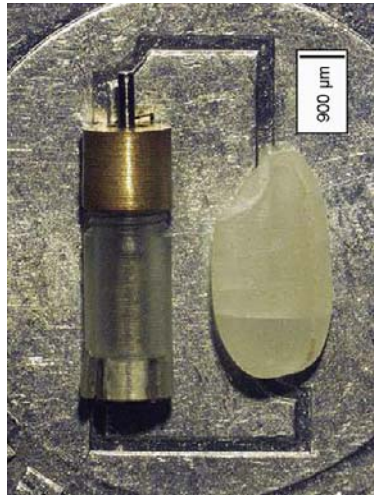


**Fig. 10.** An image of a “wobble motor” by Kanda et al. [17]; note the small size of the motor when compared to the grain of rice on the right. (Figure © [2004] IEEE).

actuator was used in a ‘robotic hand’ and was able to drive a 10 g load [20].

The wobble motor has been scaled even further downwards. The design by Kanda et al. [17] also uses a cylindrical PZT stator and was also operated using the fundamental bending mode. The stator for this actuator is 0.8 mm in diameter and 2.2 mm in height. The total dimensions of the actuator were 2 mm in diameter and 5.9 mm in height, approximately the same dimensions as the stator design produced by Morita et al. [21]. An image of the completed actuator is shown in Fig. 10.

At 40  $V_{p-p}$  and an operating frequency of 69 kHz the maximum rotational velocity was 3850 rpm. With a 5 mN preload, from a spring element, the maximum torque was 0.025  $\mu\text{Nm}$ .

A recent design in the same class was produced by Zhang et al. [24]. The dimensions of the actuator are 1 mm in diameter and 8 mm in length, including a spring element used for the preload. At a resonance frequency of 58 kHz and an input voltage of 100  $V_{p-p}$ , the actuator produced a starting torque of 7.8  $\mu\text{Nm}$  and rotational velocities in excess of 3000 rpm.

Wobble motors produce good outputs at small scales. However, the design has limitations. The use of a bulk PZT stator, although potentially beneficial to performance, introduces possible problems in terms of reliability and robustness, due to the fragile nature of the ceramic. Moreover, the potential uses of the actuator may be limited due to the complex nature of the electrical input required for the piezoelectric element.

An alternative bending mode actuator design using two piezoelectric elements was developed by Koc et al. [30]. This actuator uses a cylinder of diameter 2.4 mm and length 10 mm, with two flattened sides which creates a mounting point for the two piezoelectric elements, as shown in Fig. 11. The piezoelectric elements were bulk PZT, poled through their thickness, with the stator itself made from brass. The actuator uses a spring element for the required preload.

The two degenerate orthogonal bending modes for such a design have a frequency that is very close, due to the symmetric structure of the stator. By exciting one piezoelectric element at a frequency between the two resonant frequencies, both modes could be excited. This resulted in the desired elliptical motion at the

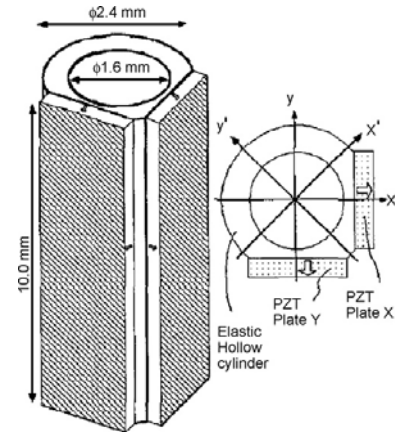


**Fig. 11.** When excited by one of the piezoelectric elements, the degenerate bending modes of the bending mode actuator by Koc et al. [30] couple to create an elliptical motion at the stator tip. Excitation by the second piezoelectric element reverses the rotation direction. (Figure © [2002] IEEE).

stator tip. By exciting the other PZT element, the rotational direction could be reversed. The actuator was operated at 69.5 kHz. At 120 V, the start-up torque was 1800  $\mu\text{Nm}$ . The maximum rotational velocity was 573 rpm, with a maximum power of 60 mW and a running torque of 1000  $\mu\text{Nm}$ . The benefit of exciting coupled resonant frequencies using one driving signal can be seen in the large output of this design. The performance of this actuator is approximately nine times better than the motor by Morita et al. [20], which is of a similar scale.

An alternative to the orthogonal bending modes used in the wobble motor, the superposition of axial and bending motions has been explored as a method for obtaining an elliptical stator motion. By exciting a bending mode in a part of the stator, whilst simultaneously vibrating the whole stator axially, an elliptical motion in the axial plane may be obtained.

As with wobble motors, the operational frequency required to excite a bending mode keeps the rotational velocity of these motors relatively low. In contrast, the vertical nature of the elliptical stator motion means that the contact point between the stator and rotor can be offset from the rotation axis of the rotor. Such a design improves the torque characteristics of this class of motor due to the increase in the moment arm associated with the stator. This is further improved by the option of having more than one contact point between the rotor and stator. However, to ensure a suitable motor scale, the size of the bending element must be reduced when compared to a wobble motor of the same scale. This reduction reduced other performance benefits, though the service life of such motors should be better than a wobble motor as the piezoelectric element does not have to be run at resonance.

A good example of such a design is the one proposed by Yao et al. [26]. This design was also one of the first piezoelectric ultrasonic resonant micro/milli-scale actuators to use a multi-layer piezoelectric linear actuator (MLPA) [31]. The MLPA is made up of hard PZT layers of a thickness of 250  $\mu\text{m}$  stacked alternately with copper electrodes of 25  $\mu\text{m}$  thickness and laminated with epoxy. The PZT MLPA is the largest external dimension of the actuator, with a diameter of 3 mm. This design uses two bending elements in the stator, as can be seen in Fig. 12. The actuator showed a maximum starting torque of 127.5  $\mu\text{Nm}$ , with a maximum rotational velocity of 1070 rpm at an input of 80  $V_{p-p}$ .

226

B. Watson et al. / Sensors and Actuators A 152 (2009) 219–233

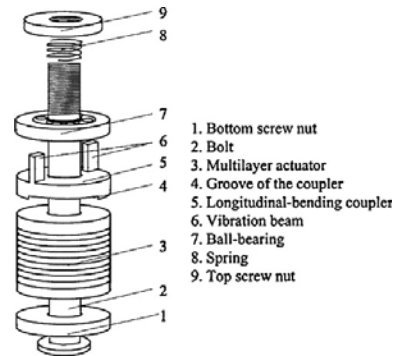


**Fig. 12.** The bending mode actuator by Yao et al. [26] couples the axial motion of the multi-layer piezoelectric actuator (MLPA) with the excited bending mode of the vibration beams, resulting in an elliptical stator tip motion in the vertical plane. (Figure © [2001] IEEE).

A different use of bending and axial vibration modes was proposed by Suzuki et al. [32] who developed a micro-actuator 2 mm in diameter and 0.3 mm in height. The piezoelectric ceramics are shaped rectangular parallelepipeds polarised in the direction of their thickness. As the piezoelectric elements vibrate, the elastic cantilever oscillator that the piezoelectric elements are attached to generate vibration and flexion, creating elliptical movements at the free end of the cantilever oscillator. This motion is transferred to the rotor by friction with the flat spring providing a preload. The stator is constructed from PZT elements glued to a stainless steel base. The rotor is made from nickel by electroforming and gilding. The flat spring is also constructed from stainless steel, and is formed through an etching process. The actuator had an operating speed of approximately 1500 rpm with a maximum torque of  $3.2 \mu\text{N}\cdot\text{m}$  at a driven voltage of  $18 V_{p-p}$ .

In the design by Aoyagi et al. [27], the fundamental axial and second order bending modes of the stator are used to achieve the elliptical stator tip motion. The stator consists of two PZT elements sandwiching a stainless steel vibrator. The bending and axial modes are excited in the vibrator by the PZT elements, delivering elliptical motion at the contact point with the shaft. This is illustrated in Fig. 13. The total size of the actuator is centimetre-scale, but due to the thin shaft, and low height (approximately  $50 \mu\text{m}$ ) it has been included in this review. With an input of  $30 V_{p-p}$ , this rotational actuator achieved a torque of  $60 \mu\text{N}\cdot\text{m}$  and 8000 rpm.

Tamura et al. also produced an actuator in this class [28]. The unusual design couples the axial and bending modes in the stator by using the crystal anisotropy of Lithium Niobate ( $\text{LiNbO}_3$ ) from which it is fabricated. Fig. 14(a) illustrates how in an X-axis rotated, Y-axis cut plate the elastic coefficients  $s_{ij}^E$  ( $i = 1, 2, 3$ ) and

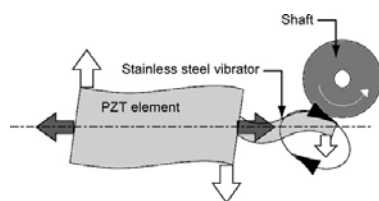


**Fig. 13.** The actuator by Aoyagi et al. couples the fundamental axial and second bending resonant modes within a stainless steel vibrator to impart a torque on the shaft [27].

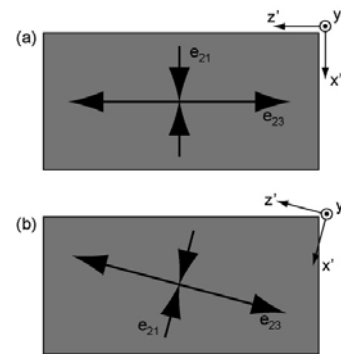


**Fig. 14.** An additional rotation about the  $y'$ -axis of the X-rotated, Y-plate  $\text{LiNbO}_3$  allows the axial and bending resonance modes to be coupled in the actuator design by Tamura et al. [28].

the piezoelectric constant  $e_{25}$  associated with the in-plane shear are zero. This results in the fundamental axial and second bending modes being independent. However, by applying an additional rotation about the  $y'$ -axis for the standard plate (Fig. 14(b)), the elastic and piezoelectric characteristics are changed; the elastic coefficients  $s_{15}^E$  and  $s_{35}^E$  become non-zero. The longitudinal components of stress and strain in the length and width directions are combined with the in-plane shear components, coupling the fundamental axial and second bending modes. This unusual design resulted in an actuator with dimensions of  $10 \text{ mm} \times 2.55 \text{ mm} \times 0.5 \text{ mm}$  for the stator, giving a performance of 1000 rpm and  $25 \mu\text{N}\cdot\text{m}$  in the counter-clockwise direction and 5000 rpm and  $12 \mu\text{N}\cdot\text{m}$  in the clockwise direction.

#### 4.1.3. Torsional mode actuators

Torsional mode actuators were one of the earliest types of piezoelectric ultrasonic actuators researched. The initial focus was on "hybrid" designs, utilising two piezoelectric elements, one poled axially and other poled radially. Using two driving signals, the output of the piezoelectric elements could be combined to create a one-directional driving force [33]. These motors, though efficient, are complex and expensive, making them unsuitable for use as a micro/milli-scale actuator.

More recent research in micro/milli-scale actuators has focussed on the coupling of torsional and axial resonant modes within the

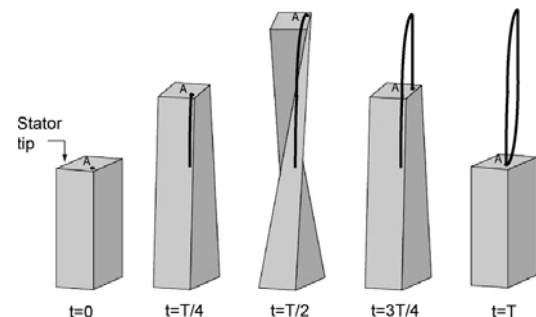


**Fig. 15.** An illustration of the stator motion for an axial/torsional coupled actuator, where  $T$  is the period of one cycle and  $t$  is the time. The coupling of the axial and torsional modes produces the desired elliptical stator tip motion.



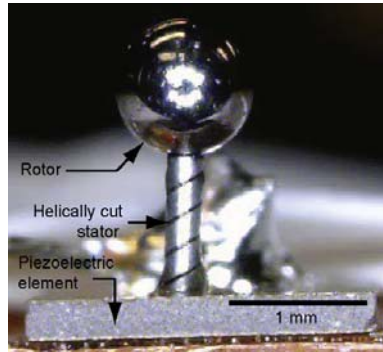


**Fig. 16.** Photo of the torsional mode actuator produced by Watson et al. [34]. The helical cuts in the stator couple the axial and torsional resonant modes.

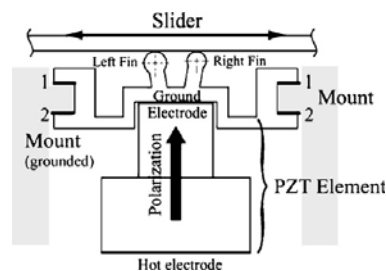


**Fig. 17.** Linear actuator design by Friend et al. [18]. The design uses asymmetrical fins to produce the driving force for the slider. (Figure © [2006] IEEE).

stator to achieve the same result. The axial vibration mode is used to increase or decrease the contact force between the stator and rotor, and the torsional mode is used to impart the tangential driving force. An example of a stator motion for an axial/torsional coupled mode actuator is shown in Fig. 15. The key to the design of such actuators is the geometry chosen for the stator, which enables the axial and torsional resonant modes to be matched.

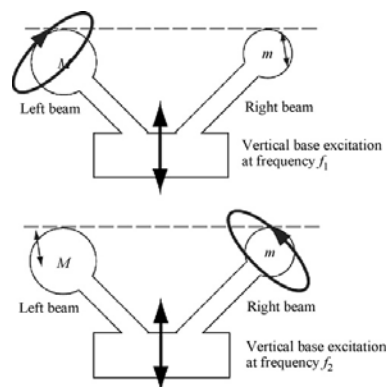


**Fig. 18.** The distinct resonant frequencies of the asymmetrical fins of the linear bending mode actuator by Friend et al. [18] enables bi-directional operation. (Figure © [2006] IEEE).

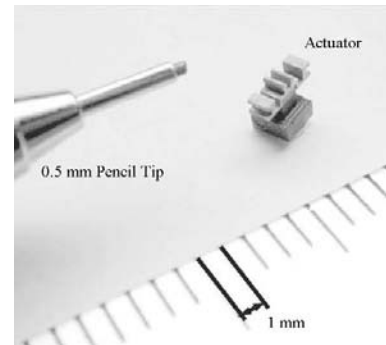


**Fig. 19.** A photo showing the small-scale of the "Baltan" actuator by Friend et al. [18]. (Figure © [2006] IEEE).

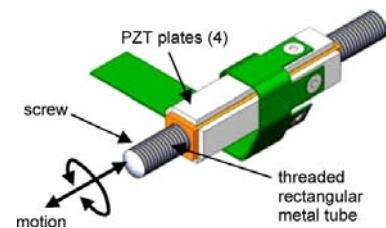


**Fig. 20.** The SQUIGGLE® motor by New Scale Technologies uses a small diameter threaded screw to convert the coupled orthogonal bending modes wobbling motion to a linear output [37]. (Figure © [2009] Newscale Technologies).

Both axial and torsional resonant modes produce stator tip displacements smaller than those associated with bending class actuators. However, the use of the torsional mode ensures that a large proportion of the potential tangential motion is imparted to the rotor, benefitting the actuator output. The coupled axial/torsional mode also produce higher rotational speeds than bending mode designs. The designs in general must have a long thin geometry as the stator length governs the frequency of operation. Using a short stator produces a high operating frequency, promoting undesirable operating characteristics.

The design by Watson et al. [34] is a recent example of this class of actuators and is shown in Fig. 16. Two diametrically opposed helical cuts in the stator are used to couple the axial and torsional motion of the stator tip. The stator is 250  $\mu\text{m}$  in diameter and 1 mm in length, making it the smallest stator of any piezoelectric ultrasonic actuator produced. The stator is driven by a single PZT element at 677 kHz. At 28.1  $V_{p-p}$ , the actuator produced a maximum torque of 0.013  $\mu\text{N}\cdot\text{m}$  and a maximum rotational velocity of 1300 rpm.

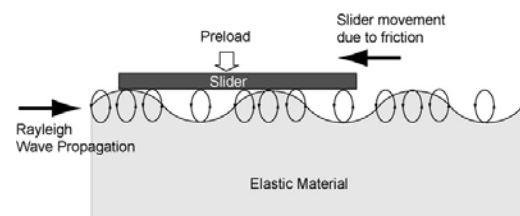


**Fig. 21.** Propagating wave actuators are different from standing wave actuators in that every point on the stator contact face undergoes an elliptical motion. Like standing wave actuators, friction is used to drive the slider.

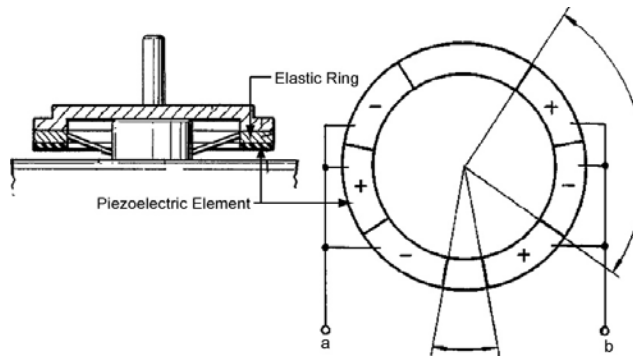


Fig. 22. A propagating wave "surfing" motor developed by Sashida [39]. The design uses multiple vibration sources (a and b) to create multiple standing waves in the piezoelectric element, that through superposition create a propagating wave around the elastic ring.

#### 4.2. Linear actuators

Research into standing wave linear micro-actuators has been limited to designs using resonant bending modes. Linear bending mode actuators differ little in operation from rotational actuators. As with rotational actuators, a resonant bending mode of the stator is combined with another vibration mode to elicit an elliptical motion from the stator. However, due to the requirement of a linear output, it is beneficial for the stator motion to be planar, as opposed to the favoured wobble motion of rotational actuators. As such, the coupled orthogonal bending mode actuators have no particular benefits over other actuators, such as ones that employ coupled axial and bending modes.

The requirement of a two-dimensional stator motion has an effect on the characteristics of these types of actuators. As with rotational actuators, the use of a bending mode magnifies the overall displacement of the stator, benefiting the actuator output. However, as the output is linear, the disadvantage in output velocity is reduced.

One of the few linear piezoelectric ultrasonic actuators developed at millimetre scales was developed by Friend et al. in 2006 [18]. The 'Baltan' micro-actuator is a linear bi-directional micro-actuator capable of nanometre scale positioning accuracy. The stator of the actuator uses a set of asymmetrical fins to provide the driving force to the slider, as shown in Fig. 17. By changing the length, attached mass, and mounting angle of the two beams, two distinct fundamental flexural resonance frequencies can be obtained. Each beam tip, at the appropriate resonance frequency, would roughly trace out an arc centred about the beam's base due to the flexural vibration in the beam in combination with the axial motion of the base.

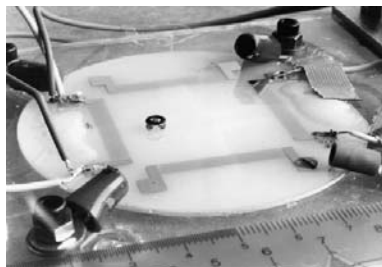


Fig. 23. The first surface acoustic wave (SAW) motor, produced by Kurosawa et al. [40]. (Figure © [1996] IEEE).

However, if the axial and bending motions are in phase, the net result would be rectilinear motion at either beam tip. By vibrating the base of the structure slightly away from the resonance of either beam, elliptical motion can be obtained from one of the two beam tips whilst the other beam tip will be vibrating rectilinearly and out-of-phase with respect to the other beam tip by approximately  $90^\circ$ , promoting motion in one direction. This is shown in Fig. 18.

The actuator gave a sliding velocity of 100 mm/s and 12 mN sliding force in either direction. A peak of 212 mm/s and 44 mN were obtained. By reducing the length of the applied signal, the sliding distance was reduced to  $90 \pm 2$  nm. An indication of the scale of the device can be seen in Fig. 19. Friend et al. [35] then further reduced the scale of this design, meeting Feynman's original 1/64-in. challenge made in 1959 [36]. At these small scales, the actuator produced outputs of 40 mm/s and 30 mN in either direction.

An alternative to linear actuators using planar bending motion is the SQUIGGLE<sup>®1</sup> motor produced by New Scale Technologies [37]. This actuator uses coupled bending modes driven by four piezoelectric elements to create a wobbling motion in a central hollow tube. Unusually however, the actuator converts this wobbling motion to a linear displacement through the use of a threaded screw. This can be seen in Fig. 20. The actuator has a maximum dimension of 6 mm and a driven shaft of 0.9 mm. It produces a force of 196 mN and a velocity of 5 mm/s.

#### 5. Propagating wave actuators

The generalised operation of a propagating wave actuator is not dissimilar from that of a standing wave design. As with standing wave designs an elliptical motion is generated in the stator, which is then transferred to the rotor through a friction coupling. The elliptical motion however, is not generated at one point within the stator; rather every point on one stator face follows an elliptical trajectory. This occurs due to the generation of the propagating wave within the stator. In general, this wave is generated by combining two standing waves,  $90^\circ$  out of phase. As the wave travels, particles at the surface move in an elliptical path as shown in Fig. 21. The component standing waves are generated by a pair of vibration sources, allowing the wave to propagate in both directions.

As with standing wave designs, the key characteristics of actuators in this class can be attributed to the physics involved in the operation. The small amplitude, high frequency waves generated

<sup>1</sup> SQUIGGLE is a registered trademark of New Scale Technologies.

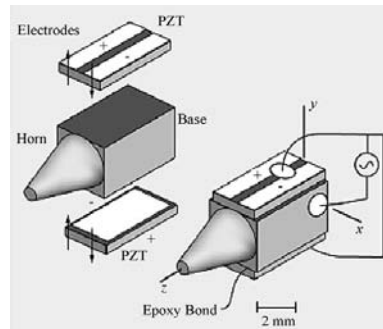


Fig. 24. The design by Friend et al. [45] uses in-plane piezoelectric bimorphs to shear the stator, resulting in a rotation at the stator tip. (Figure © [2004] IEEE).

promote high speed and high output force operation. The high frequency operation also allows a very high accuracy to be obtained from the rotor or slider, with the potential for sub-nanometre positioning accuracy [38]. However, the amplitude of the propagating wave and the complex design used to generate them both have a detrimental effect on the scalability of these designs. The amplitude of the wave produced by the device reduces linearly with the scale of the device. As we approach a sub-millimetre scale actuator, the vibration amplitude becomes so small as to become difficult to use as a driving mechanism in an actuator. In addition, the necessity to fabricate complex interdigital transducers for surface acoustic wave actuators at scales small enough to produce a sub-millimetre actuator also limits the potential for a reduction in scale for this particular class of propagating wave actuators. As such, no significant micro/milli-scale actuators have been developed in this class. Here we review some of the most successful larger scale designs and those that provide high accuracy.

### 5.1. Rotational actuators

The most successful type of rotary propagating wave actuators are known as “surfing” motors. In these motors, multiple vibration sources are used to excite an elastic ring. A standing wave is generated for each vibration source, and through superposition of these waves, it is possible to create a propagating wave around the ring.

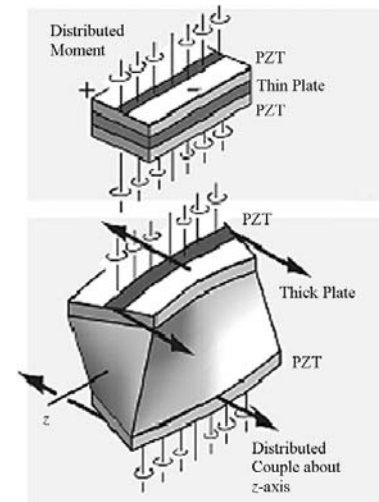


Fig. 25. Induced net moment due to the shearing effect of the piezoelectric material for the actuator proposed by Friend et al. [45]. (Figure © [2004] IEEE).

The most successful of this type of design, and arguably the most successful piezoelectric actuator ever produced, was developed by Sashida [39]. In this actuator, the travelling wave is induced in a thin piezoelectric ring, with directional reversibility achieved through an exchange of sine and cosine input voltages. Bonded to the piezoelectric element is a ring-shaped elastic body. This body was then in contact with the ring-shaped slider. This is illustrated in Fig. 22.

With a propagating wave frequency of 44 kHz and an input voltage of 10.3 V, the actuator developed a maximum torque of approximately  $100 \times 10^3 \mu\text{Nm}$  and a maximum rotational velocity of greater than 30 rpm [22].

The performance of these surfing motors was excellent. The use of multiple input voltages to create multiple standing waves made them very controllable and high output actuators. However, as mentioned above, the complexity of the design currently limits their reduction to sizes to a scale of a few millimetres.

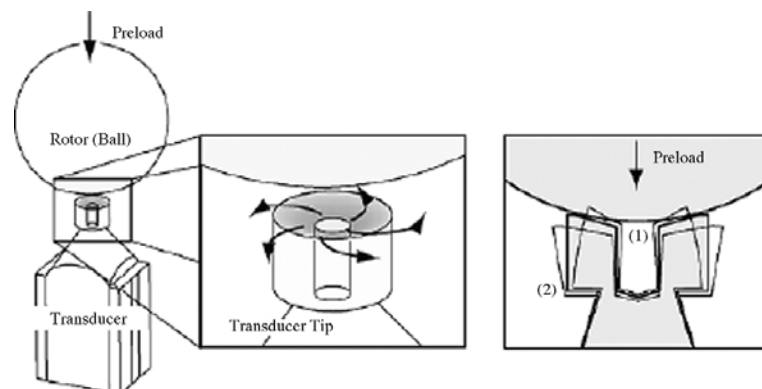


Fig. 26. Novel transducer tip design by Friend et al. The radial movement of the stator tip varies the contact force, replacing the need for an elliptical stator tip motion. The preload was produced by the weight of the ball [46].



**Table 2**  
Comparison of the performance of rotational micro/milli-scale actuators.

Design	Driving force	Class	Motion	Actuator principle	Stator type	Stator dia. (mm)	Stator length (mm)	Output ( $\mu\text{Nm}$ )	Velocity (rpm)
Dubois and Muraik, 1998 [29]	Converse piezoelectric effect	Standing wave	Rot.	Flexural mode	Membrane-like, elastic fins, bulk PZT	5.2	N/A	0.94	1020
Morita et al., 1999 [20]	Converse piezoelectric effect	Standing wave	Rot.	Orthogonal bending modes	Bulk PZT tube	2.4	10	220	650
Morita et al., 2000 [21]	Converse piezoelectric effect	Standing wave	Rot.	Orthogonal bending modes	Thin-film PZT on tube	1.4	5	0.67	680
Kanda et al., 2004 [17]	Converse piezoelectric effect	Standing wave	Rot.	Orthogonal bending modes	Bulk PZT	0.8	2.2	0.025	3850
Zhang et al., 2006 [24]	Converse piezoelectric effect	Standing wave	Rot.	Orthogonal bending modes	Bulk PZT tube	1	5	7.8	3000
Koc et al., 2002 [30]	Converse piezoelectric effect	Standing wave	Rot.	Degenerate ortho. bending modes	Tube with two flattened sides for bulk PZT	2.4	10	$1.8 \times 10^3$	573
Yao et al., 2001 [26]	Converse piezoelectric effect	Standing wave	Rot.	Axial/bending	PZT MPLA	3	N/A	127.5	1070
Suzuki et al., 2000 [32]	Converse piezoelectric effect	Standing wave	Rot.	Axial/bending	Bulk PZT on stainless steel	2	0.3	3.2	1500
Aoyagi et al., 2004 [27]	Converse piezoelectric effect	Standing wave	Rot.	Axial/bending	Bulk PZT on stainless steel vibrator	$16.2 \times 2.5$	0.55	60	8000
Tamura et al., 2008 [28]	Converse piezoelectric effect	Standing wave	Rot.	Axial/bending	Crystal anisotropy in $\text{LiNbO}_3$	$10 \times 2.55$	0.5	25 CCW	5000
Watson et al., 2008 [34]	Converse piezoelectric effect	Standing wave	Rot.	Torsion/axial	Helically cut tube	0.25	1	0.013	1300
Friend et al., 2004 [46]	Converse piezoelectric effect	Ultrasonic disp.	Rot.	In-plane shearing	Bulk PZT on phosphor bronze	$3 \times 4$	8.5	100	425

**Table 3**  
Comparison of the performance of linear micro/milli-scale actuators.

Design	Driving force	Class	Motion	Actuator principle	Stator type	Stator dim. (mm × mm)	Stator length (mm)	Output (mN)	Velocity (mm/s)
Friend et al., 2006 [18]	Converse piezoelectric effect	Standing wave	Linear	Bending and vertical mode coupling	Asymmetrical fins on bulk PZT	3.25 × 2.5	2	44	212
SQUIGGLE® [37]	Converse piezoelectric effect	Standing wave	Linear	Orthogonal bending mode coupling	Threaded screw and bulk PZT	1.55 × 1.55	6	196	5
Shigematsu and Kurosawa, 2006 [38]	Converse piezoelectric effect	Prop. wave	Linear	SAW from IDT	Lithium Niobate	2.5 × 3	12.5	13	300

## 5.2. Linear actuators

The most promising of the linear propagating wave actuators are the surface acoustic wave (SAW) actuators. A SAW is an acoustic wave that travels along the surface of an elastic material. If the SAW is generated on a piezoelectric substrate (usually Lithium Niobate—LiNbO<sub>3</sub>) the acoustic energy can be converted to a mechanical displacement. This displacement occurs at each particle on the surface and takes the form an ellipse as already discussed.

The first actuator using SAW as a driving force was reported by Kurosawa et al. in 1996 [40]. The design was based on a Ø76.2 mm Lithium Niobate substrate. The actuator incorporated four interdigital transducers (IDT's), allowing motion in the *x*- and *y*-directions. The driving frequency was approximately 9 MHz and produced a lateral transfer speed of 200 mm/s. An image of the device can be seen in Fig. 23.

The design was improved through the use of a multiple contact stator [41], and improved contact conditions [42] to the point where the actuator could be operated at 70 MHz and produced a transfer speed of 700 mm/s. The reduction in scale of the actuator was also examined by Takasaki et al., who produced an actuator with dimensions of 15 mm × 60 mm × 1 mm [43].

The excellent positioning accuracy of this actuator was demonstrated by Shigematsu et al. [44]. With a 60 mm × 15 mm × 1 mm LiNbO<sub>3</sub> substrate and a 9.6 MHz driving force, a stepping drive of 2 nm steps produced a 1-nm friction driven step. The authors reported that there was a potential for a sub-nanometre friction driven step. The most recent published work by Shigematsu and Kurosawa has further reduced the size of the actuator to using a 3 mm × 12.5 mm × 2.5 mm substrate and a 100 MHz driving frequency [38].

SAW linear actuators have great potential as positioning devices with nanometre accuracy or better. They also have a high output speed and good output force making them suitable for a wide range of applications. However, it will prove difficult to continually reduce the scale of the device due to the necessity to manufacture the IDT's. Moreover, SAW based actuators suffer from high wear rates stemming from the direct contact between the slider and the fragile piezoelectric material at high operating frequencies. These drawbacks of SAW propagation remain a hurdle to their commercialisation.

## 6. Ultrasonic displacement actuators

Ultrasonic displacement actuators use the displacement of the piezoelectric element and stator, cycled at ultrasonic frequencies, to create a useful output at the rotor or slider. These designs differ from those previously discussed as no wave is set-up within the stator to assist with the performance or to convert the piezoelectric output to a more useful form. Instead, the piezoelectric output is either converted into a linear or a rotational output at the rotor through geometrical design. Limited research has been carried out in this class for micro/milli-actuators, however, we will note one design here. The design by Friend et al. [45], which uses a shearing action to drive a rotational piezoelectric ultrasonic actuator.

This design used multiple electrodes for a bulk piezoelectric element to effectively create an in-plane bimorph. The bulk piezoelectric elements were epoxy bonded to a phosphor bronze structure that included a tapered conical horn that acted as the stator tip, as shown in Fig. 24. By applying a voltage to the correct electrodes, an in-plane shearing motion could be achieved in the piezoelectric elements. This shearing motion led to a net moment at the conical tip. This can be seen in Fig. 25.

The actuator was operated at 192.1 kHz. At this frequency and 27.3 V<sub>RMS</sub>, a rotational velocity of 71 rpm was obtained at the

1.5 mm-diameter tip. At 1.02 MHz and 17.8 V<sub>RMS</sub>, 371 rpm was measured at the tip.

Friend et al. also made a modification to this actuator, introducing a unique concept for translating the stator motion to the rotor [46]. By tapering the hole, as shown in Fig. 26, the tapered surface moved away from the rotor as the tip expanded outward, lowering both the contact force and the delivered torque.

The revised actuator was operated at two frequencies: 186.3 kHz for counter-clockwise motion and 246.6 kHz for clockwise motion. With a preload of 87.1 mN, a torque of 100  $\mu$  Nm was obtained with a rotational velocity 425 rpm. The overall efficiency peaked at more than 40%.

This design proposed an interesting stator set-up, and showed the potential of the system. However, the results were obtained in the absence of a practical rotor and preload system. It is also worth noting that this design requires a stator manufactured from a material with a low material damping loss. Attempts to use biocompatible tantalum in place of phosphor bronze were unsuccessful. The design may also benefit from being operated at the torsional resonance frequency of the stator, potentially improving the stator tip response.

## 7. Actuator performance classification

As has been noted throughout this review, classifying micro/milli-scale actuators according to their basis of operation provides an understanding of the actuator performance. This has benefits in determining successful designs, suitability for applications and further research areas. In Tables 2 and 3 we summarise the performance data of the actuators reviewed according to classification to further highlight this relationship and to provide an easy reference for review.

## 8. Future research areas

The next logical step of research in this field will be to develop a practical sub-millimetre scale actuator, a true micro-actuator. There is already a demand for such actuators in the micro-robotics industry [1] and the medical profession, specifically for minimally invasive surgery [2,3]. To achieve this goal, we anticipate that research will focus on the driving mechanisms that are best suited to a continued reduction in scale. From this review, it can be seen that those designs that use a resonant mode to induce a standing wave are well suited for micro-applications, and as such, will continue to be an active area of research.

In addition to the research into driving mechanisms and stator design, the other components of the actuators will also need further development. Further research into thin-film, polymer and other technologies that provide designers with smaller and better piezoelectric elements will be required. We also envisage continuing work in the areas of micro-fabrication to allow these new micro-actuators to be successfully constructed. Aside from the size reduction of actuators, further investigation needs to be conducted to improve actuator efficiencies. Current efficiencies for ultrasonic milli-actuators are around 20%. Improvements in the understanding of rotor/stator interface and friction coupling could potentially increase these efficiencies leading to a better performing actuators.

## References

- [1] J. Bardina, R. Thirumalainambi, Micro-Flying Robotics in Space Missions, SAE International, 2005.
- [2] E.J. Hanly, M.A. Talamini, Robotic abdominal surgery, *The American Journal of Surgery* 188 (2004) 19S–26S.
- [3] A. Mencias, M. Quirini, P. Dario, Microrobotics for future gastrointestinal endoscopy, *Minimally Invasive Therapy and Allied Technologies* 16 (2007) 91–100.
- [4] K. Hori, T. Miyagawa, L. Ito, Development of ultra-small sized servo actuator with brushless DC motor planetary gear drive and optical rotary encoder, *International Journal of the Japan Society for Precision Engineering* 31 (1997) 1–5.
- [5] C.K. Malek, V. Saile, Applications of LIGA technology to precision manufacturing of high-aspect-ratio micro-components and systems: a review, *Microelectronics Journal* 35 (2004) 131–143.
- [6] K.E. Drexler, Productive nanosystems: the physics of molecular fabrication, *Physical Education* 40 (2005).
- [7] M. Mehregany, P. Nagarkar, S.D. Senturia, J.H. Lang, Operation of microfabricated harmonic and ordinary side-drive motors, in: *Proceedings of the IEEE Micro-Electro-Mechanical Systems Workshop*, February 11–14, 1990, pp. 1–8.
- [8] A.M. Fennimore, T.D. Yuzvinsky, M.S. Wei-Qiang Han, J. Fuhrer, A. Cumings, Zettl, Rotational actuators based on carbon nanotubes, *Nature* 424 (2003) 408–410.
- [9] R. Yeh, S. Hollar, K.S.J. Pister, Single Mask, Large force, and large displacement electrostatic linear inchworm motors, *Journal of Microelectromechanical Systems* 11 (2002) 330–336.
- [10] S. Heo, Y.Y. Kim, Optimal Design, Fabrication of MEMS rotary thermal actuator, *Journal of Micromechanics and Microengineering* 17 (2007) 2241–2247.
- [11] M.J. Sinclair, The Seventh Intersociety Conference on Thermal and Thermomechanical Phenomena in Electronic Systems (2000) 127–132.
- [12] Y.-C. Su, L. Lin, A.P. Pisano, A water-powered osmotic microactuator, *Journal of Microelectromechanical Systems* 11 (2002) 736–742.
- [13] S. Yokota, A. Sadamoto, Y. Kondoh, Y. Otsubo, K. Edamura, A micro motor using electroconjugate fluids (ECFs), *JSM International Journal Series C* 44 (2001) 756–762.
- [14] S. Yokota, K. Kawamura, K. Takemura, K. Edamura, A High-integrated micromotor using electro-conjugate fluid (ECF), *Journal of Robotics and Mechatronics* 17 (2005) 142–148.
- [15] S. Yokota, Personal correspondence, October 2008.
- [16] L. Frank, J. Lee, Camera with electronic flash and piezoelectric lens motor, U.S. Patent Number 4,291,958, September 1981.
- [17] T. Kanda, A. Makino, L. Suzumori, T. Morita, M.K. Kurosawa, A cylindrical micro ultrasonic motor using a micro-machined bulk piezoelectric transducer, in: *IEEE Ultrasonics Symposium*, Montreal, QC, Canada, August 23–27, 2004, pp. 1298–1301.
- [18] J. Friend, Y. Gouda, K. Nakamura, S. Ueha, A simple bidirectional linear microactuator for nanopositioning—the “Baltan” microactuator, *IEEE Transactions on Ultrasonics, Ferroelectrics, and Frequency Control* 53 (2006) 1160–1168.
- [19] T. Morita, M.K. Kurosawa, T. Higuchi, An ultrasonic micromotor using a bending cylindrical transducer based on PZT thin-film, *Sensors and Actuators A* 50 (1995) 75–80.
- [20] T. Morita, M.K. Kurosawa, T. Higuchi, Cylindrical micro ultrasonic motor utilizing bulk lead zirconate titanate (PZT), *Japanese Journal of Applied Physics* 38 (1999) 3347–3350.
- [21] T. Morita, M.K. Kurosawa, T. Higuchi, A cylindrical shaped micro ultrasonic motor utilizing PZT thin film 1.4 mm in diameter and 5.0 mm long stator transducer, *Sensors and Actuators A* 83 (2000) 225–230.
- [22] K. Uchino, Piezoelectric ultrasonic motors: overview, *Smart Material Structures* 7 (1998) 273–285.
- [23] T. Mortia, Miniature piezoelectric motors—review, *Sensors and Actuators A* 103 (2002) 291–300.
- [24] H. Zhang, S. Dong, S. Zhang, T. Wang, Z. Zhang, L. Fan, Ultrasonic micro-motor using miniature piezoelectric tube with diameter of 1.0 mm, *Ultrasonics* 44 (2006) e603–e606.
- [25] K. Uchino, *Piezoelectric Actuators and Ultrasonic Motors*, Kluwer Academic Publishers, Boston, 1997.
- [26] K. Yao, B. Koc, K. Uchino, Longitudinal-bending mode micromotor using multilayer piezoelectric actuator, *IEEE Transactions on Ultrasonics, Ferroelectrics, and Frequency Control* 48 (2001) 1066–1071.
- [27] M. Aoyagi, F. Suzuki, Y. Tomikawa, I. Kano, High-speed thin ultrasonic spindle motor and its application, *Japanese Journal of Applied Physics* 43 (2004) 2873–2878.
- [28] H. Tamura, K. Shibata, M. Aoyagi, T. Takano, Y. Tomikawa, S. Hirose, Single phase drive ultrasonic motor using LiNbO<sub>3</sub> rectangular vibrator, *Japanese Journal of Applied Physics* 47 (2008) 4015–4020.
- [29] M.A. Dubois, P. Muralt, PZT thin film actuated elastic fin micromotor, *IEEE Transactions on Ultrasonics, Ferroelectrics, and Frequency Control* 45 (1998) 1169–1177.
- [30] B. Koc, S. Gagatay, K. Uchino, A piezoelectric motor using two orthogonal bending modes of a hollow cylinder, *IEEE Transactions on Ultrasonics, Ferroelectrics, and Frequency Control* 49 (2002) 495–500.
- [31] K. Uchino and K. Ohnishi, Linear motor, U.S. Patent Number 4,857,79, August 1989.
- [32] Y. Suzuki, K. Tani, T. Sakuhara, Development of a new type piezoelectric micromotor, *Sensors and Actuators A* 83 (2000) 244–248.
- [33] S. Mishi, Rotary ultrasonic motor, U.S. Patent Number 4,697,117, September 1987.
- [34] B. Watson, J. Friend, L. Yeo, Piezoelectric ultrasonic resonant motor with stator diameter less than 250  $\mu$ m: the Proteus motor, *Journal of Micromechanics and Microengineering* 19 (2009) 022001–022005.
- [35] J. Friend, L. Yeo, M. Hogg, Piezoelectric ultrasonic bidirectional linear actuator for micropositioning fulfilling Feynman's criteria, *Applied Physics Letters* 92 (2008) 0141071–0141073.
- [36] R. Feynman, There's plenty of room at the bottom, *Journal of Microelectromechanical Systems* 1 (1992) 60–66.

- [37] D.A. Henderson, Simple ceramic motor.. inspiring smaller products, actuator 2006, in: 10th International Conference on New Actuators, Bremen, Germany, June 14–16, 2006.
- [38] T. Shigematsu, M.K. Kurosawa, Miniaturized SAW motor with 100 MHz drive frequency (letter), *IEEE Transactions on Sensors and Micromachines* 126 (2006) 166–167.
- [39] T. Sashida, Motor device utilizing ultrasonic oscillation, U.S. Patent Number 4,562,374, December 1985.
- [40] M. Kurosawa, M. Takahashi, T. Higuchi, Ultrasonic linear motor using surface acoustic waves, *IEEE Transactions on Ultrasonics, Ferroelectrics, and Frequency Control* 43 (1996) 901–906.
- [41] M.K. Kurosawa, M. Chiba, T. Higuchi, Evaluation of a surface acoustic wave motor with a multi-contact-point slider, *Smart Material Structures* 7 (1997) 305–311.
- [42] M. Takasaki, M.K. Kurosawa, T. Higuchi, Optimum contact conditions for miniaturized surface acoustic wave linear motor, *Ultrasonics* 38 (2000) 51–53.
- [43] M. Takasaki, N. Osakabe, M.K. Kurosawa, T. Higuchi, Miniaturization of surface acoustic wave linear motor, in: *IEEE Ultrasonics Symposium*, Sendai, Miyagi, Japan, October 5–8, 1998, pp. 679–682.
- [44] T. Shigematsu, M.K. Kurosawa, K. Asai, Nanometer stepping drives of surface acoustic wave motor, *IEEE Transactions on Ultrasonics, Ferroelectrics and Frequency Control* 50 (2003) 376–385.
- [45] J. Friend, K. Nakamura, S. Ueha, A torsional transducer through in-plane shearing of paired planar piezoelectric elements, *IEEE Transactions on Ultrasonics, Ferroelectrics, and Frequency Control* 51 (2004) 870–877.
- [46] J. Friend, K. Nakamura, S. Ueha, A piezoelectric micromotor using in-plane shearing of PZT elements, *IEEE/ASME Transactions on Mechatronics* 9 (2004) 467–473.

### Biographies

**Brett Watson** is currently undertaking his Ph.D. degree in Mechanical Engineering at Monash University as part of the MicroNanophysics Research Laboratory. He received his Bachelor of Engineering (Mechanical) from Curtin University in 2000. His research interests are in motors, actuators and propulsion systems for biomedical micro-robotic applications. His paper on a piezoelectric micro-motor for in vivo swimming microbots at AOTULE 2008 was highly commended, he is a member of the Golden Key Honour Society and currently has a patent application in progress.

**James Friend** (member IEEE) received the B.S. degree in aerospace engineering, and the M.S. and Ph.D. degrees in mechanical engineering from the University of Missouri-Rolla in 1992, 1994, and 1998, respectively. He received two awards—the AIAA Jefferson Student Goblet and ASME Presentation Award—for his presentation on ultrasonic motor analysis at the AIAA/ASME/AHS/ASC 26th Annual Structural Dynamics Conference in 1996, an award for the encouragement of young scientists at the Symposium for Ultrasonic Electronics and Engineering in 2003 for a presentation on acoustic waveguides, an award in 2004 for a presentation on the Scream actuator at the Spring Meeting of the Acoustical Society of Japan, excellence in teaching and early career researcher awards from the Monash Faculty of Engineering in 2007 and 2008, respectively, and a Future Leader award from the Davos Future Summit in Sydney in 2008. James Friend joined Monash University in late 2004, and founded and co-directs the \$6.5 million MicroNanophysics Research Laboratory with clean room and biolab, a current staff of three academics, three post-doctorates and thirteen PhD students. He is an associate professor and deputy head of the Department of Mechanical and Aerospace Engineering at Monash University, with research interests in micro/nanodevices for biomedical applications, with over one hundred peer-reviewed publications, with five book chapters, fifty-two peer-reviewed journal papers, and thirteen patents and patent applications.

**Dr Leslie Yeo** is currently an Australian Research Fellow and Senior Lecturer in the Department of Mechanical & Aerospace Engineering and Co-Director of the Micro/Nanophysics Research Laboratory at Monash University, Australia. He received his PhD from Imperial College London in 2002, for which he was awarded the Dudley Newitt prize for a computational/theoretical thesis of outstanding merit. Prior to joining Monash University, he was a Mathematical Modeller at Det Norske Veritas UK and a postdoctoral research associate in the Department of Chemical & Biomolecular Engineering at the University of Notre Dame, USA. Dr Yeo was the recipient of the 2007 Young Tall Poppy Science Award from the Australian Institute for Policy & Science 'in recognition of the achievements of outstanding young researchers in the sciences including physical, biomedical, applied sciences, engineering and technology', and a finalist in the 2008 Eureka Prize People's Choice Award. Dr Yeo is the author of over 70 research publications and over 10 patent applications, and is currently the Associate Editor of the American Institute of Physics journal *Biomicrofluidics*.

## 1.5 Research Goals

The aim of this thesis is to demonstrate that by changing the design methodology of current piezoelectric ultrasonic motors we can realise a motor with a geometry and performance suitable to drive a tetherless *in vivo* microbot, with the requirements outlined in Table 1.1.

Our design methodology focusses on the stator of the motor. A design focus on the stator allows the separation of the piezoelectric element from the stator, simplifying the system when compared with existing piezoelectric motor designs. This simplification leads to the motor being easier to fabricate, which in turn results in a greater potential for a reduction in scale. In addition, our methodology aims to only use one electrical input signal to the piezoelectric element. This will further simplify the design, allowing for a further decrease in scale. These simplifications are achieved through a stator design that matches resonant frequencies and produces an elliptical stator tip motion from a single excitation source. To investigate this methodology, we propose to develop a piezoelectric ultrasonic micro-motor that uses a sub-millimeter scale piezoelectric element to excite coupled axial and torsional vibration modes. The coupled modes will be achieved through the use of helical geometries in a tubular stator, which will simultaneously excite both the axial and torsional resonant modes.

The first goal of this research is to demonstrate the viability of our simplified design methodology by producing a piezoelectric motor with stator dimensions suitable for *in vivo* applications. The complexity of current stator designs is one of the major shortcomings in existing piezoelectric ultrasonic micro-motor design, as such, the primary aim of this work is to ensure the stator design is robust and

easy to fabricate at the desired scale using existing fabrication techniques. This will be achieved by using commercially available stainless steel tubing as the base of the stator with the final design produced using commercially available laser machining techniques.

As our design methodology calls on a simple piezoelectric element to excite multiple resonant modes in the stator, much of the focus of the research will be on the understanding of how the geometric parameters of the stator design affect the resonant modes of interest. Existing analytical and computational methods to achieve this are complex and computationally time consuming, whilst providing only a limited understanding of the interactions and effects that changes in the geometric parameters have on the resonant frequencies. The second goal of the research is to develop novel, simple to use modelling techniques that clearly demonstrate how the geometric parameters affect the frequencies of interest, whilst illuminating the underlying physics of these effects. This will enable an improvement in motor performance by ensuring the resonant frequencies are closely matched.

The final goal of this research is to build on the modelling techniques developed to examine the matching of modes, to enable a motor to be designed that not only closely matches the mechanical resonant modes, but also the electro-mechanical resonance of the entire system. Operating the motor at a frequency that excites both mechanical and electro-mechanical resonances ensures the greatest performance and efficiency from the design. To do this, we aim to develop a design model of the whole mechanical system that makes up the motor. Traditionally such problems are only tackled using the finite element method due to the complexity of the many components in the mechanical system. This is

computationally expensive, and in general, does not lead to a thorough understanding of the system. By using scaling techniques, we can not only limit the number of cases to be examined using the finite element method, we can gain an understanding of how the system parameters affect the multitude of resonances. By developing such a modelling technique, it will be possible to fully design a micro-motor with the greatest chance of being suitable for use in a tetherless *in vivo* microbot.

## 1.6 Thesis Outline

On the following pages an overview of the thesis chapters are given. The research of this thesis is reported in Chapters 2–4, with each chapter consisting of a peer reviewed or submitted journal article. As the chapters are original published works, there may be some repetition to ensure an understanding of the motivation and concepts by individual readers.

### Chapter 2

Chapter 2 reports the proof of concept of our proposed simplified design methodology. The stator of the prototype was fabricated from a commercially available stainless steel tubing, using widely available laser cutting techniques. Using this method a stator diameter of  $241\ \mu\text{m}$  was achieved, approximating the dimensional requirements laid out in Section 1.3. Performance of the prototype was determined to be  $16.5\ \text{nNm/mm}^2$  for start-up torque and  $5.4\ \mu\text{W/mm}^2$  for power. Conclusions from the work included: the proposed design methodology

is sound, a stator was successfully fabricated at the required dimensions for the first time for this class of motor, and the performance did not meet the requirement outlined in Table 1.1. This shortfall in performance leads directly to the work in Chapter 3.

### **Chapter 3**

The work of Chapter 3 is focussed on modelling the axial and torsional resonant frequencies of the stator. The first modelling technique reported decomposes the stator into easy to understand components, allowing a simple analysis of the system to be carried out. The second, more general, method uses scaling techniques to limit the number of cases evaluated using the finite element method. This not only reduces calculation time, but gives an insight impossible using the finite element method alone. Three-dimensional contour plots derived from the models define the interactions between geometric parameters required to ensure matched axial and torsional resonant frequencies. Applying this knowledge a second prototype was fabricated using a stator that was designed to have closely matched axial and torsional resonant frequencies. This prototype has an increase in performance of at least three times over the prototype reported in Chapter 2.

### **Chapter 4**

Chapter 4 acts as a culmination of the work presented in the preceding chapters. The scaling modelling technique introduced in Chapter 3 is extended to model



all components of the motor, including the epoxy bonds. This facilitates a motor design that closely matches the axial, torsional and electro-mechanical resonant frequencies of the motor. Closely matching these three resonant frequencies improves the performance of the motor over previous prototypes. The resulting design includes a stator diameter of  $241\text{ }\mu\text{m}$  and an overall diameter of  $400\text{ }\mu\text{m}$ , as determined by the commercial availability of components. As designed, the motor produced a start-up torque of  $23.8\text{ nNm/mm}^2$  and a peak output power of  $5\text{ }\mu\text{W/mm}^2$  using a preload of  $46.6\text{ }\mu\text{N}$ . Increasing the preload on the motor to  $2264\text{ }\mu\text{N}$  improved this performance to  $230.4\text{ nNm/mm}^2$  and  $76.5\text{ }\mu\text{W/mm}^2$ . These results meet the geometric and performance requirements for a motor to drive a tetherless micro-robot within the human body.

## Chapter 5

Chapter 5 presents the conclusions of the thesis by providing the key contributions of the work. In Chapter 5 we also discuss the future research areas that may follow on from the work presented in this thesis.

## Proof of Concept

*This chapter reports the proof of concept of our proposed piezoelectric ultrasonic resonant micro-motor design methodology. Using widely available techniques and materials, a motor stator diameter of 241  $\mu\text{m}$  was achieved. This approximates the dimensional requirements outlined in Section 1.3. Performance of the prototype was determined to be 16.5 nNm/mm<sup>2</sup> for start-up torque and 5.4  $\mu\text{W}/\text{mm}^2$  for power. These results lead to the chapter conclusions, which include the following: that the proposed design methodology is sound with a working prototype motor produced, a stator was successfully fabricated at the required dimensions for an *in vivo* microbot for the first time for this class of motor, and that the performance did not meet requirements for the desired application.*

As discussed in Section 1.4 we hypothesise that the fundamental reason a piezoelectric motor has yet to be produced at a scale suitable for *in vivo* applications is a design methodology that results in complex, difficult to fabricate motor designs. To overcome this we have proposed a simplified design methodology that focusses on the stator, potentially simplifying the motor as outlined in Section 1.5.

To commence testing our hypothesis, the paper reproduced in Chapter 2 reports the proof of concept of our proposed design methodology. The reported prototype uses a single piezoelectric element driven from a single harmonic electrical input. The novel stator design uses helical cuts in the cylindrical stator to enable coupling of axial and torsional motion at the stator tip. When excited using the piezoelectric element, it is possible to achieve the desired stator tip motion.

A key aim of the work was to fabricate the first stator for a piezoelectric ultrasonic motor with dimensions suitable for a tetherless microbot. The stator design had to be robust and easy to fabricate, to ensure existing problems with piezoelectric motor designs were not repeated. The prototype stator was fabricated using commercially available laser cutting techniques, and from commercially available stainless steel tubing. The diameter of the fabricated stator was  $241\text{ }\mu\text{m}$ , the diameter of the smallest commercially available tubing, and was the first time a piezoelectric ultrasonic motor has been fabricated with a stator diameter that approximately meets the requirements outlined in Table 1.1.

The prototype motor performance was determined by the method introduced by Nakamura et al. [29]. Using the cross-sectional area of the 1 mm diameter rotor to normalise the results, the start-up torque was determined to be  $16.5\text{ nNm/mm}^2$ , and the power determined to be  $5.4\text{ }\mu\text{W/mm}^2$ . As a comparison, we note that the start-up torque is approximately equal to that outlined in Table 1.1, whilst the power is significantly lower. This shortfall leads to the work reported in Chapter 3.

There are three key conclusions that can be drawn from the work presented in Chapter 2. Firstly, that our proposed design methodology is sound, producing

a functioning piezoelectric ultrasonic resonant micro-motor. Secondly, that our prototype stator design was simple enough to be fabricated at the required scale for the first time in this class of motor. Lastly, that an improvement in motor performance is necessary to meet the aim of producing a motor suitable for an *in vivo* tetherless microbot.

# Piezoelectric ultrasonic resonant motor with stator diameter less than 250 $\mu\text{m}$ : the Proteus motor

**Brett Watson**, James Friend and Leslie Yeo

*Journal of Micromechanics and Microengineering*

19, 022001 (2009)

Copyright © 2009 IOP Publishing

doi:10.1088/0960-1317/19/2/022001

## Declaration for Thesis Chapter 2

### Declaration by candidate

In the case of Chapter 2, the nature and extent of my contribution to the work was the following:

Nature of contribution	Extent of contribution (%)
I was chief investigator for this work. I was responsible for the design, modelling, motor assembly, experimental work and the writing of the paper.	80

The following co-authors contributed to the work.

Name	Nature of contribution
Professor James Friend	Overall supervision, piezoelectric finite element model, review of drafts and submission of paper to journal.
Associate Professor Leslie Yeo	Overall supervision and review of drafts.

		Date
Candidate's Signature		

### Declaration by co-authors

The undersigned hereby certify that:

- (1) the above declaration correctly reflects the nature and extent of the candidate's contribution to this work, and the nature of the contribution of each of the co-authors.
- (2) they meet the criteria for authorship in that they have participated in the conception, execution, or interpretation, of at least that part of the publication in their field of expertise;
- (3) they take public responsibility for their part of the publication, except for the responsible author who accepts overall responsibility for the publication;
- (4) there are no other authors of the publication according to these criteria;
- (5) potential conflicts of interest have been disclosed to (a) granting bodies, (b) the editor or publisher of journals or other publications, and (c) the head of the responsible academic unit; and
- (6) the original data are stored at the following location(s) and will be held for at least five years from the date indicated below:

Location(s)	Department of Mechanical and Aerospace Engineering, Monash University, Clayton, Victoria, Australia.
-------------	--

		Date
Signature 1		
Signature 2		

## BRIEF COMMUNICATION

# Piezoelectric ultrasonic resonant motor with stator diameter less than $250\ \mu\text{m}$ : the *Proteus* motor

B Watson, J Friend and L Yeo

Micro/Nanophysics Laboratory, Department of Mechanical and Aerospace Engineering,  
Monash University, Wellington Road, Clayton, VIC 3800, AustraliaE-mail: [james.friend@eng.monash.edu.au](mailto:james.friend@eng.monash.edu.au)

Received 25 September 2008, in final form 18 November 2008

Published 20 January 2009

Online at [stacks.iop.org/JMM/19/022001](http://stacks.iop.org/JMM/19/022001)**Abstract**

Minimally invasive and *in vivo* surgery is limited by the ability to provide controllable and powerful motion at scales appropriate for navigation within the human body. A motor for *in vivo* microbot propulsion is presented with a stator diameter of  $\phi 250\ \mu\text{m}$ , demonstrating the potential to directly drive a flagellum for swimming at up to 1295 rpm with a torque of 13 nN m. The motor uses coupled axial-torsional vibration at 652–682 kHz in a helically cut structure excited by a thickness-polarized piezoelectric element. The output power is  $4.25\ \mu\text{W}$ , on the order of what is necessary to navigate small human arteries.

(Some figures in this article are in colour only in the electronic version)

**1. Introduction**

Opportunities for micro-motors and micro-actuators abound in fields as diverse as bio-medicine, electronics, aeronautics and the automotive industry. Responses to this need have been just as diverse, with designs developed using electromagnetic [1], electrostatic [2], thermal [3] and osmotic [4] driving forces. This paper specifically focuses on the need for small scale motors for medical procedures. In many circumstances, techniques used in minimally invasive surgery are inferior to standard cut and sew methods. Even the most complex minimally invasive surgical equipment reduces a surgeon's dexterity, feel and visibility [5]. To improve this, research is being carried out on systems that will permit procedures to be conducted on the micro-scale using remotely operated micro-robots (microbots). To facilitate this, micro-scale motors are required. A design that has significant potential in this area is one that uses ultrasonic vibrations driven by the converse piezoelectric effect. Piezoelectric ultrasonic actuators are familiar at the macro scale, with many examples in commercial products such as watches and cameras. These designs have

favourable scaling characteristics [6] and, in general, are simple designs, which provide an excellent platform for the development of micro-motors and micro-actuators.

Piezoelectric ultrasonic motors with stator dimensions of approximately 1 mm and overall dimensions of only a few millimetres exist [7, 8], and, even smaller, linear actuators have been developed that fit into a cube  $400\ \mu\text{m}$  on a side [9]. However, a practical rotational actuator with dimensions significantly below 1 mm—a true *micro*-motor—has not yet been achieved. Here we detail the principle of operation, design, fabrication and initial results for a piezoelectric ultrasonic motor with a stator diameter of less than  $250\ \mu\text{m}$ . This stator design is approximately 70% smaller than the smallest design produced so far [8], and is the first step towards the design of a practical micro-motor. The intended application of this motor is in propulsion of micro or so-called 'nanorobots' [10] for autonomous non-invasive observation and surgery within the human body, the reason for naming it the *Proteus* motor after the project name used in Isaac Asimov's prescient *Fantastic Voyage* [11].

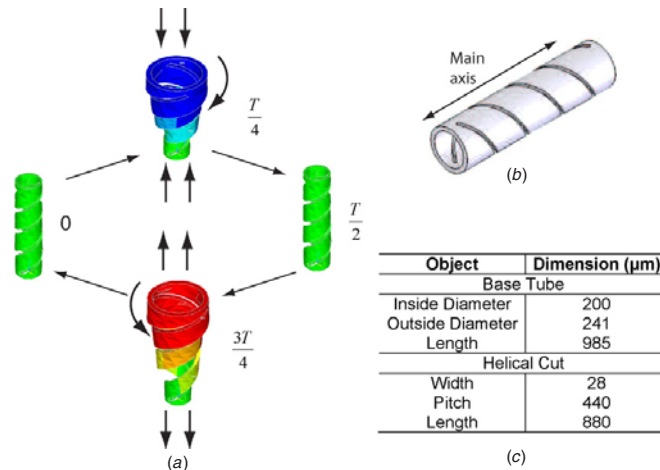


**Figure 1.** Finite element analysis (a) confirmed the coupled axial and torsional motion of the helically cut stator (b) of dimensions significantly below 1 mm (c).

## 2. Basis of operation

Piezoelectric ultrasonic resonant micro-motors use the resonant vibration mode of the stator to amplify and control the induced strain of the piezoelectric element. By coupling resonant modes in the stator, an elliptical motion at the stator tip can be obtained. This elliptical motion can, through friction coupling, be converted to provide rotational motion [12]. The most successful and popular micro-motor designs to date use coupled orthogonal bending modes in the stator, driven through a spring-force friction coupling [7, 8]. These designs however, have fragile and difficult to fabricate piezoelectric stators. Moreover, complex stator designs and control systems provide obstacles to a further reduction in scale.

An alternative is to couple the axial and torsional modes of the stator. Such a design allows the coupled modes to be excited by one piezoelectric element not integral to the stator. This removes many of the obstacles associated with coupled bending mode designs. It is known that coupling axial and torsional modes can be achieved through geometric design, the most striking example of this being the Wilberforce pendulum [13]. However, limited research has been carried out to obtain practical stator designs, or to explore the potential design benefits at small scales, with only limited macro-scale designs having been developed [14, 15].

In response, we have developed a new stator design coupling torsional and axial displacements. The design uses a helical geometry machined with laser micro-machining technology (Norman Noble Inc., Highland Heights, OH, USA) to induce torsional motion during axial vibration, with a resulting motion reminiscent of a helical spring under axial loading. Due to a phase shift in the torsional response with respect to the axial motion, an elliptical motion of the stator tip is developed. This allows a net motion to be achieved through the friction coupling.

## 3. Design and fabrication

The finite element analysis program ANSYS V10.0 (ANSYS Inc., Canonsburg, PA, USA) was used to conduct an initial limited parametric study on the helical geometries. It modelled all stator geometries and used free boundary conditions at both ends. Through modal analysis, this study was used to qualitatively confirm the expected stator motion and to determine a robust, but not optimized, geometric design for fabrication. The stator motion is illustrated in figure 1. Future work will see the model expanded to include the piezoelectric element, which will allow an accurate comparison to experimental results and a model validation.

The fabricated design consists of a 304 stainless-steel tube, with two diametrically opposite helical cuts through the tube wall (fabricated by Norman Noble Inc., Highland Heights) also detailed in figure 1. The resonant modes are excited by a hard composition lead zirconate titanate (PZT) piezoelectric element (C203, Fuji Ceramics, Tokyo, Japan), bonded by epoxy to one end of the helically cut stator. The PZT element is 3.5 mm in length, 2.5 mm in width and 0.27 mm in thickness; thickness poled, and was chosen due to availability. The frequency of operation was well below any frequency that would excite an out-of-plane mode in the PZT. Therefore, as the thickness dimension (0.27 mm) is smaller than what one would expect to use in a finalized micro-motor (of PZT dimensions  $0.25 \text{ mm} \times 0.25 \text{ mm} \times 0.5 \text{ mm}$  thickness for example) the large element does not artificially improve the motor performance. Moreover, if we consider that a PZT element of 0.5 mm thickness can produce a larger displacement and accept a higher input voltage, both of which improve performance, the use of the larger element may reduce the motor performance. A conductive copper tape was used to attach the PZT/stator component to an alumina base for testing. All wiring was hand soldered. The friction coupling



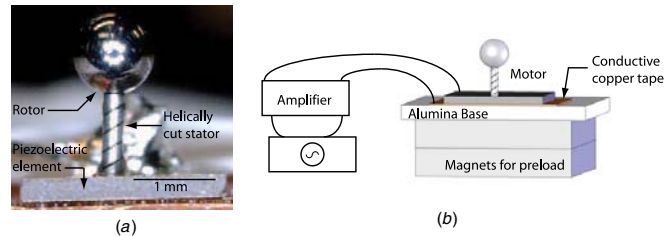


**Figure 2.** (a) Photo of the micro-motor prototype showing the  $\phi 241 \mu\text{m}$  helically cut stator, 1 mm stainless-steel ball as a rotor and the PZT element. (b) Magnets were used to increase the friction coupling preload.

was enhanced using a magnetic force acting on a hardened steel ball 1 mm in diameter (the rotor), to provide a preload of  $39 \mu\text{N}$ . The steel ball was chosen to act as a rotor as it provided a clean reflective surface that assisted in the performance measurement, was easy to mount, had a homogeneous and predictable density, accepted a magnetic preload and provided a smooth consistent surface for operation. The test prototype can be seen in figure 2.

#### 4. Method

A scanning laser Doppler vibrometer (LDV) and associated software (MSA-400, Polytec GmbH, Waldbronn, Germany) was used to measure motion along the thickness axis for the PZT element. Whilst simultaneously exciting all frequencies in the band 0–2 MHz, an axial displacement response spectrum was recorded. This response was compared with the response spectrum of the axial motion along the main axis of the stator (see figure 1). The stator spectrum was determined using the same method, and the same frequency band as for the PZT. Peaks in the axial motion of the stator tip, without the associated peaks in the PZT motion, were determined to be stator resonant modes. Each resonant mode was further analysed using the scanning LDV to classify the mode shape based on the displacement of the stator tip. Figure 3 shows the typical displacement profile of the stator tip for nominal axial and bending derived modes. The motor was designed to place the bending modes away from the axial and torsional modes of the motor. Rotor motion was recorded using a digital high speed camera (Olympus i-speed, Olympus Australia, Mount Waverley, Australia) at 1000 frames per second. The angular velocity versus time curve was determined using the Olympus i-speed image processing software (V1.16, Olympus Industrial America, Orangeburg, NY, USA).

#### 5. Results and discussion

Through experimental trials, the motor was found to have the highest start-up torque and rotational velocity when driven at the stator axial resonance with the largest amplitude, 677 kHz. Using the technique described in section 4, this mode was found to be predominantly a high-order axial/torsional coupled mode. However, due to a small misalignment during fabrication and the nonlinearity of the design, bending and

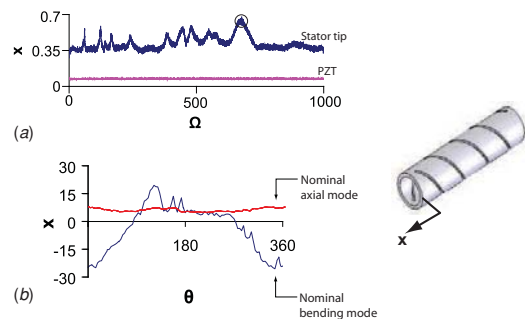


**Figure 3.** By comparing the axial response spectrum for the PZT and stator tip, the stator modes could be highlighted (a);  $x$  is the axial displacement in (nm) and  $\Omega$  is the driving frequency (kHz). The circled area is the frequency of operation. These resonant frequencies were then analysed with the LDV to determine the mode shape (axial or bending based) (b):  $x$  is the axial displacement (nm) and  $\theta$  is the circumferential position (degrees) around the free tip of the stator. Note an in-phase displacement amplitude over the whole tip for the axial mode, while the bending mode only has a positive displacement for approximately half of the circumference around the tip.

pinching modes were also weakly excited at this frequency. Further work will be required to determine the extent of the effect of these additions. Using a signal generator and amplifier (Rohde & Schwarz-SML 01 and NF-HSA 4501, North Ryde, NSW, Australia), the PZT element was driven at 677 kHz with an applied voltage  $28.1 V_{p-p}$ , as measured with an oscilloscope (LeCroy WaveJet 334, Chestnut Ridge, NY, USA). The voltage was applied as a step input, resulting in the angular velocity versus time curve shown in figure 4. The fitted exponential curve is derived from the standard curve for a piezoelectric ultrasonic motor [16].

The maximum angular velocity recorded for the motor was  $135 \text{ rad s}^{-1}$  (1295 rpm). Using this as an input for the method developed by Nakamura *et al* [16] the maximum start-up torque, based on the curve shown in figure 4, was calculated to be 13 nNm. For the chosen operating mode, the motor had an operating frequency range of 652–682 kHz. Although performance varies across this range, having a large operational frequency band will allow flexibility in future applications for the motor, should frequency stabilization or modulation be important in power supplies. The performance

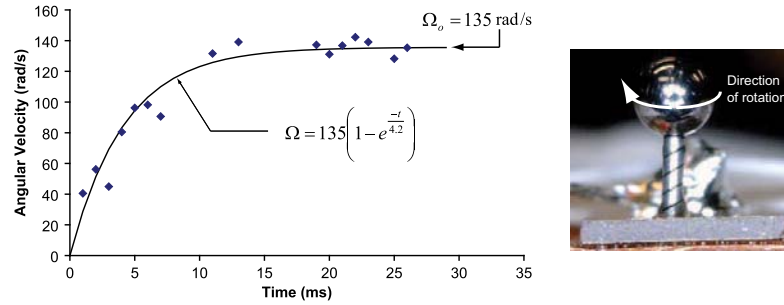


**Figure 4.** Angular velocity versus time results for an applied step voltage of 28.1 V<sub>p-p</sub>, preload of 39  $\mu$ N and a operating frequency of 677 kHz. The fitted curve is derived using the method outlined in [16].

of this new design compares well with other piezoelectric ultrasonic micro-motors; this design offers 52% of the torque with a stator 32% of the size of the most comparably sized device by Kanda *et al* [8].

To improve the motor performance, further work to match the torsional and axial resonance frequencies of the laser machined tubing with the thickness resonance of the piezoelectric element is to be carried out. To ensure this performance improvement is sustained whilst having a complete motor volume of less than 1 mm<sup>3</sup>, it will be necessary to provide a new rotor arrangement that removes the need for large magnets currently used to provide a preload. This may ultimately be achieved through a mechanical ‘snap-fit’, however current research is focussed on a novel approach to casting magnetic components. As magnetic force is proportional to distance to the power of 4 ( $F_{\text{mag}} \propto d^4$ ), it is hypothesised that a magnetic rotor will alleviate the need for the large magnets, or at the very least reduce the size required to within the desired volume range.

We now consider an application for the motor, that of the drive system for an *in vivo* ‘swimming microbot’ that uses an *E. coli*-like flagellum as a means of propulsion. Such microbots have been highlighted as having great potential for use in *in vivo* medical procedures due to the low Reynolds number propulsion system [17]. The power output of the reported motor is approximately  $\phi_{\text{max}} T_{\text{max}}/4 = (135)(13 \times 10^{-9})/4 \text{ W} = 4.25 \text{ } \mu\text{W}$ . Using Higdon’s model for flagellar propulsion [18], we may determine the average power required for swimming in small human arteries from  $\bar{P} = 6\pi\mu A \bar{U}^2 \eta_0^{-1} K$ ; blood has a viscosity of approximately  $\mu = 0.0035 \text{ Pa s}$  [19],  $A$  is the radius of the swimming microbot which we will assume to be approximately the size of the motor, 150  $\mu\text{m}$ , and  $K$  is Stokes’ law correction for a prolate spheroid, 2.7 [20]. From Higdon’s results, we take  $\eta_0^{-1} = 200$ , which leaves only the swimming speed  $\bar{U}$  to be defined. If we presume the device should at least swim as fast as the blood flow, and consider the right central retinal artery as a suitable example of a location both difficult to reach by other means and one where this device would be used,  $\bar{U} \approx 6.0 \text{ cm s}^{-1}$  [21], giving 19  $\mu\text{W}$  of power. This demonstrates that potentially the motor could propel such a microbot.

## 6. Conclusions

We have demonstrated a piezoelectric ultrasonic resonant motor that uses coupled axial and torsional displacements, derived from a helically cut stator. This novel stator design enables us to overcome many of the problems associated with current designs and produce a stator that is less fragile, simpler to control and more than 70% smaller than the smallest stator design produced thus far. With further research, such motor designs potentially open the door to new areas of *in vivo* surgery and micro-robotics.

## Acknowledgments

This work was made possible in part by grants SM/07/1616 and SM/06/1208 from the CASS Foundation, grant DP0773221 from the Australian Research Council, and the New Staff and Small Grant Scheme funds from Monash University.

## References

- [1] Hori K, Miyagawa T and Ito K 1997 Development of ultra-small sized servo actuator with brushless DC motor, planetary gear drive and optical rotary encoder *Int. J. Japan Soc. Precis. Eng.* **31** 1–5
- [2] Mehregany M, Nagarkar P, Senturia S D and Lang J H 1990 Operation of microfabricated harmonic and ordinary side-drive motors *Proc. IEEE Micro-Electro-Mechanical Systems Workshop* p 8
- [3] Sinclair M J 2000 A high force low area MEMS thermal actuator *Seventh Intersociety Conf. on Thermal and Thermomechanical Phenomena in Electronic Systems*
- [4] Su Y-C, Lin L and Pisano A P 2002 A water-powered osmotic microactuator *J. Microelectromech. Syst.* **11** 736–42
- [5] Hanly E and Talamini M 2004 Robotic abdominal surgery *Am. J. Surg.* **188** 19S–26
- [6] Wang Z L 2007 Nanopiezotronics *Adv. Mater.* **19** 889–92
- [7] Morita T, Kurosawa M K and Higuchi T 2000 A cylindrical shaped micro ultrasonic motor utilizing PZT thin film 1.4 mm in diameter and 5.0 mm long stator transducer *Sensors Actuators* **83** 225–30
- [8] Kanda T, Makino A, Suzumori K, Morita T and Kurosawa M K 2004 A cylindrical micro ultrasonic motor

- using a micro-machined bulk piezoelectric transducer *IEEE Ultrasonics Symp.*
- [9] Friend J, Yeo L and Hogg M 2008 Piezoelectric ultrasonic bidirectional linear actuator for micropositioning fulfilling Feynman's criteria *Appl. Phys. Lett.* **92** 014107
- [10] Sitti M 2001 Survey of nanomanipulation systems *IEEE-NANO 2001: Proc. 2001 1st IEEE Conf. on Nanotechnology* pp 75–80
- [11] Asimov I 1966 *Fantastic Voyage: A Novel* (Boston: Houghton Mifflin)
- [12] Uchino K 1998 Piezoelectric ultrasonic motors: overview *Smart Mater. Struct.* **7** 13
- [13] Berg R E and Marshall T S 1991 Wilberforce pendulum oscillations and normal modes *Am. J. Phys.* **59** 32–8
- [14] Wajchman D, Liu D, Friend J and Yeo L 2008 An ultrasonic piezoelectric motor utilising a non-circular cross-sectioned twisted beam *IEEE Trans. Ultrason. Ferroelectr. Freq. Control* **55** 832–40
- [15] Tsujino J 1998 Ultrasonic motor using a one-dimensional longitudinal-torsional vibration converter with diagonal slits *Smart Mater. Struct.* **7** 345–51
- [16] Nakamura K, Kurosawa M, Kurebayashi H and Ueha S 1991 An estimation of load characteristics of an ultrasonic motor by measuring transient responses *IEEE Trans. Ultrason. Ferroelectr. Freq. Control* **38** 481–5
- [17] Behkam B and Sitti M 2006 Design methodology for biomimetic propulsion of miniature swimming robots *ASME J. Dynamic Syst. Meas. Control* **128** 36–43
- [18] Higdon J J L 1978 The hydrodynamics of flagellar propulsion: helical waves *J. Fluid Mechanics* **94** 331–51
- [19] Rand P W, Lacombe E, Hunt H E and Austin W H 1964 Viscosity of normal human blood under normothermic and hypothermic conditions *J. Appl. Physiol.* **19** 117–22
- [20] Happel J and Brenner H 1965 *Low Reynolds Number Hydrodynamics* (Englewood Cliffs, NJ: Prentice Hall)
- [21] Fuchsiger-Mayrl G, Polak K, Luksch A, Polska E, Dorner G T, Rainer G, Eichler H-G and Schmetterer L 2001 Retinal blood flow and systemic blood pressure in healthy young subjects *Graefes Arch. Clin. Exp. Ophthalmol.* **239** 673–7

## Modelling of Stator Resonant Frequencies

*This chapter focusses on modelling the axial and torsional resonant frequencies of the stator, with an aim of improving motor performance by ensuring the motor stator has closely matched resonant frequencies. For this, two modelling techniques are reported that reduce calculation time compared with traditional analytical or finite element modelling techniques, whilst giving an insight impossible using the finite element method alone. The three-dimensional contour plots derived from the models define the interactions between geometric parameters to ensure matched axial and torsional resonant frequencies. Applying this knowledge, a second prototype was fabricated using a stator that was designed to have closely matched axial and torsional resonant frequencies. This prototype improved performance by at least three times over the initial prototype reported in Chapter 2. However, performance was still below what is required to drive a tetherless microbot, with many of the motor components also too large.*

The performance of the prototype motor reported in Chapter 2 was insufficient to successfully drive a tetherless microbot inside a human. A key reason for this is the weakly coupled axial and torsional resonant modes. To obtain the greatest performance from the motor, it is beneficial to design the motor in such a way as to ensure that the resonant modes of operation, in this case the axial and torsional resonant modes, are closely matched. Operating a motor in this way ensures that the maximum displacements associated with the modes of interest are achieved at the same operating frequency. This results in a larger motion transfer to the rotor, and improved motor performance.

As the prototype motor reported in Chapter 2 was a proof of concept, the design process to obtain the fabricated stator design was minimal. The key design parameter, the helical pitch angle, was derived from the twisted beam motor reported by Wajchman et al. [30] and set at  $30^\circ$ . Post experimental analysis showed that this resulted in an axial resonant frequency 30% higher than the torsional resonant frequency of the same harmonic. To rectify this, and improve the performance of the prototype motor, it is necessary to modify the design to match the axial and torsional resonant frequencies of the stator. To achieve this, an understanding of how changes in the geometric parameters of the stator affect the resonant frequencies of interest is required.

The focus of the paper reproduced in this chapter was to produce a representation of how changes in the geometric parameters interact to ensure a ratio of axial to torsional resonant frequencies of one is maintained. For this, two novel models are presented. The first model decomposes the stator into easy to analyse components, in this case helical springs. The second model using scaling techniques to

limit the number of parameter cases calculated using the finite element method, whilst giving an insight not possible with using the finite element method alone. Both models enable a three-dimensional contour plot to be produced, illustrating how the geometric parameters interact to ensure an ideal case of matched axial and torsional resonant frequencies.

Important design points obtained from these plots include: that the stator length and external diameter do not affect the matching of the axial and torsional resonant frequencies, that the interaction between the pitch angle and cut width is important, and that for stator designs with a small internal diameter it is impossible to match axial and torsional resonant frequencies for a high number of cuts.

Using these models, it was possible to produce a second prototype motor that had a stator with closely matched axial and torsional resonant frequencies. This motor had a performance increase of a minimum of three times the prototype motor outlined in Chapter 2.

# A Study on Axial and Torsional Resonant Mode Matching for a Mechanical System with Complex Non-Linear Geometries

**Brett Watson**, Leslie Yeo and James Friend

*Review of Scientific Instruments.*

81, 063901 (2010)

Copyright 2010, American Institute of Physics

doi:10.1063/1.3430537

**Declaration for Thesis Chapter 3****Declaration by candidate**

In the case of Chapter 3, the nature and extent of my contribution to the work was the following:

<b>Nature of contribution</b>	<b>Extent of contribution (%)</b>
I was chief investigator for this work. I was responsible for the development of the modelling techniques, motor assembly, experimental work, interpretation of results and the writing of the paper.	80

The following co-authors contributed to the work.

<b>Name</b>	<b>Nature of contribution</b>
<b>Professor James Friend</b>	Overall supervision, review of drafts and submission of paper to journal.
<b>Associate Professor Leslie Yeo</b>	Overall supervision and review of drafts.

	<b>Date</b>
<b>Candidate's Signature</b>	

**Declaration by co-authors**

The undersigned hereby certify that:

- (1) the above declaration correctly reflects the nature and extent of the candidate's contribution to this work, and the nature of the contribution of each of the co-authors.
- (2) they meet the criteria for authorship in that they have participated in the conception, execution, or interpretation, of at least that part of the publication in their field of expertise;
- (3) they take public responsibility for their part of the publication, except for the responsible author who accepts overall responsibility for the publication;
- (4) there are no other authors of the publication according to these criteria;
- (5) potential conflicts of interest have been disclosed to (a) granting bodies, (b) the editor or publisher of journals or other publications, and (c) the head of the responsible academic unit; and
- (6) the original data are stored at the following location(s) and will be held for at least five years from the date indicated below:

<b>Location(s)</b>	Department of Mechanical and Aerospace Engineering, Monash University, Clayton, Victoria, Australia.
--------------------	--

	<b>Date</b>
<b>Signature 1</b>	
<b>Signature 2</b>	



## A study on axial and torsional resonant mode matching for a mechanical system with complex nonlinear geometries

Brett Watson, Leslie Yeo, and James Friend<sup>a)</sup>

*Department of Mechanical and Aerospace Engineering, MicroNanophysics Research Laboratory,  
Monash University, Clayton, Victoria 3800, Australia*

(Received 2 February 2010; accepted 26 April 2010; published online 4 June 2010)

Making use of mechanical resonance has many benefits for the design of microscale devices. A key to successfully incorporating this phenomenon in the design of a device is to understand how the resonant frequencies of interest are affected by changes to the geometric parameters of the design. For simple geometric shapes, this is quite easy, but for complex nonlinear designs, it becomes significantly more complex. In this paper, two novel modeling techniques are demonstrated to extract the axial and torsional resonant frequencies of a complex nonlinear geometry. The first decomposes the complex geometry into easy to model components, while the second uses scaling techniques combined with the finite element method. Both models overcome problems associated with using current analytical methods as design tools, and enable a full investigation of how changes in the geometric parameters affect the resonant frequencies of interest. The benefit of such models is then demonstrated through their use in the design of a prototype piezoelectric ultrasonic resonant micromotor which has improved performance characteristics over previous prototypes. © 2010 American Institute of Physics. [doi:10.1063/1.3430537]

### I. INTRODUCTION

Mechanical systems designed to operate at a resonant frequency have numerous advantages at small scales. Systems take advantage of the motion associated with resonance to induce motion,<sup>1</sup> enable sensing,<sup>2</sup> and convert motion without the need for gears or joints,<sup>3</sup> resulting in the design of smaller mechanical systems.<sup>4</sup> To successfully make use of such resonant phenomena, it is beneficial to have an insight into how changes in component geometry effect the desired resonant frequencies.<sup>5</sup> For a simple system such as a beam, this may be quite easily determined analytically,<sup>6</sup> but when nonlinearities are introduced, such as a curve to the beam, the analysis quickly becomes complex.<sup>7</sup> The complexity of such models does not allow for an intuitive understanding of how the resonant frequency changes with geometric parameters or the underlying physics of the system.

An alternative to creating these complex mathematical models is to use the finite element method (FEM). The FEM allows the relatively quick determination of the resonant frequencies of a system with complex nonlinear geometries. However, if the system has many parameters or a large parameter range, the computational effort required to optimize the design using this method can be tremendous. Moreover, though we may arrive at our desired design, we will not necessarily understand the effect each geometric parameter has on the outcome. Subsequently, a significant amount of effort is required to determine new optimum parameters even when only slight modifications are made to them.

In this paper, we propose to demonstrate two alternative and simple modeling techniques to gain an understanding of how the geometric parameters of a highly nonlinear geomet-

ric system affect its axial and torsional resonant frequencies. The first model makes an approximation of the system by decomposing it into a set of well-understood components. This method gives an analytical approximation of the system, allowing an intuitive understanding of the physics while providing a simple to use design tool. The second, more generalized model uses scaling techniques to enable a rational use of the FEM, which results in a pseudoanalytical approximation of the system. We believe this technique is the first example of the use of general scaling techniques such as nondimensionalization and curve fitting to determine the system stiffness and subsequently the resonant frequencies of a mechanical system. The second model provides less insight into the underlying physics of the system than the first but more easily enables an understanding of the effect of the geometric parameters and provides significantly more insight than the FEM alone. Both techniques may benefit researchers developing complex nonlinear mechanical systems at small scales by reducing design and computational time and providing additional insight to the system characteristics.

The specific test case for this work results from our previous paper<sup>8</sup> where we reported on a piezoelectric ultrasonic micromotor concept that uses coupled axial and torsional displacements of the stator tip to drive the rotor. The axial and torsional coupling was achieved by introducing a set of helical cuts to the cylindrical tube being used as the stator. To improve the micromotor performance, we wish to match the axial and torsional resonant modes of the stator. Doing so will take advantage of the increased stator tip displacements that result from operating simultaneously at both the axial and torsional resonant frequency.

A full analytical solution for such a system would be complex and not intuitive for design, such as the model proposed for a twisted beam.<sup>9</sup> Moreover, a full finite element

<sup>a)</sup>Author to whom correspondence should be addressed. Electronic mail: james.friend@eng.monash.edu.au. URL: <http://mnrl.monash.edu>.

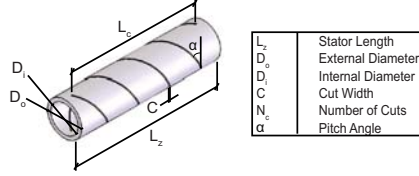


FIG. 1. (Color online) The geometric parameters of the stator that, along with the material properties, describe the system.

parametric analysis of the system geometries would be time and computationally intensive. The two models we demonstrate successfully highlight the relationship of axial-torsional resonant frequencies of the stator to the geometric parameters while being intuitive enough to be used as a design tool. Subsequent fabrication and testing of a micromotor designed using these models demonstrates a significant improvement in performance and provides a way to validate the proposed models.

## II. MODELING

### A. Stator parameters

#### 1. Nondimensionalization of stator parameters

The stiffness of the stator is a function of the six geometric parameters of the stator design and the material properties

$$K_e = f(D_o, D_i, C, N_c, \alpha, L_c, E, L_z), \quad (1)$$

$$K_r = f(D_o, D_i, C, N_c, \alpha, L_c, G, L_z), \quad (2)$$

where  $K_e$  is the axial stiffness and  $K_r$  is the torsional stiffness of the stator,  $E$  is the Young's modulus,  $G$  is the shear modulus, and the geometric parameters are outlined in Fig. 1. The quantity  $L_c$  is the cut length which is kept constant at  $0.9L_z$  as specified by our design concept, while the density  $\rho$  does not affect the stiffness. We can nondimensionalize the system using the Buckingham Pi theorem<sup>10</sup> to arrive at

$$\frac{K_e}{ED_o} = f\left(\frac{D_i}{D_o}, \frac{C}{D_o}, N_c, \alpha, \frac{L_z}{D_o}\right) \rightarrow K_e^* = f(D_i^*, C^*, N_c, \alpha, L_z^*) \quad (3)$$

for the nondimensional axial stiffness and

$$\frac{K_r}{GD_o^3} = f\left(\frac{D_i}{D_o}, \frac{C}{D_o}, N_c, \alpha, \frac{L_z}{D_o}\right) \rightarrow K_r^* = f(D_i^*, C^*, N_c, \alpha, L_z^*) \quad (4)$$

for the nondimensional torsional stiffness.

#### 2. Parameters space of the modeled stator

To validate, compare, and use the models, it will, in part, be necessary to use a model derived using the FEM. For this, we nominate a parameter space that covers a range of geometric values that would be suitable for use in our piezoelectric ultrasonic micromotor.

### B. Resonant frequency calculation

Axial and torsional resonant frequencies are calculated for both models in the same way. To determine the harmonic normalized axial resonant frequency, we use

$$\frac{\omega_e}{n} = \frac{1}{2} \sqrt{\frac{K_e}{M}}, \quad (5)$$

where  $n$  is the harmonic number,  $K_e$  is the axial stiffness as determined from the method under investigation, and  $M$  is the mass of the stator, which can be determined using

$$M = \rho D_o \left[ \frac{\pi}{4} D_o^2 (1 - D_i^{*2}) L_z^* - N_c C^* h L \right], \quad (6)$$

where  $\rho = 8000 \text{ kg/m}^3$  for 304 stainless steel,  $h$  is described by Eq. (16), and  $L$  is the total length of the helical cut and can be found using

$$L = [(0.9L_z^* D_o)^2 + (\pi D_o N_c)^2]^{1/2}. \quad (7)$$

For the harmonic normalized torsional resonant frequency, we use

$$\frac{\omega_r}{n} = \frac{1}{2} \sqrt{\frac{K_r}{I_z}}, \quad (8)$$

where  $K_r$  is the torsional stiffness as determined from the method under investigation and  $I_z$  is the second moment of the area of the stator. To calculate  $I_z$  explicitly would be complex; as such, we approximate the second moment of area by ignoring the helical twist and considering an extrusion with a cross-section identical to the stator. This approximation can be calculated using

$$I_z = \frac{\pi}{32} D_o^5 \rho L_z^* \left\{ 1 - N_c \sin^{-1} \left[ \frac{C^*}{\sin(\alpha)} \right] \right\}. \quad (9)$$

Comparisons with data taken from a solid modeling program for a specific stator design show this to be an acceptable approximation with an error of 6.5%.

We can see from this set of equations that the unknown in our system is the stiffness of the stator. It is this that we seek to determine using our models.

### C. FEM model

We choose to model the stator stiffness using two models. The first is based on the stiffness of a helical spring, henceforth referred to as the helical spring model (HSM). The second uses scaling techniques to develop a pseudostiffness, referred to as the pseudostiffness model (PSM). For both HSM and the PSM, we require a model using the FEM of the stator with which to compare or make use of.

For this we developed a model using the commercially available software package ANSYS V10.0 (ANSYS Inc., Canonsburg, PA). The stator was modeled using three-dimensional (3D) ten-node tetrahedral structural solid elements, leading to an eigenvalue extraction problem of the form

$$[K]\{\Phi\} = \lambda_i [M]\{\Phi\}, \quad (10)$$

where  $[K]$  is the structure stiffness matrix,  $\{\Phi\}$  is the eigenvector,  $\lambda_i$  is the eigenvalue, and  $[M]$  is the structure mass

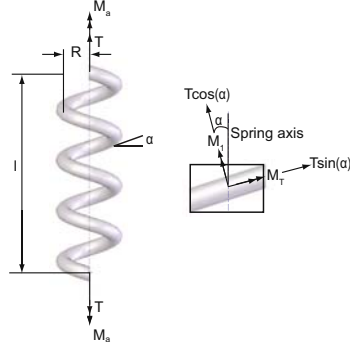


FIG. 2. (Color online) The free-body diagram of the method proposed by Wittrick (Ref. 13) to calculate the equivalent axial and torsional spring stiffness of a helical spring.

matrix. Eigenvalues were extracted using an in-built shifted block Lanczos algorithm based on the theoretical work of Grimes *et al.*<sup>11</sup>

The stator was modeled with free-free boundary conditions. We know that in our system, the mass of the piezoelectric element will be on the order of 500 times larger than that of the stator. In addition, we expect the stiffness of the components to be of the same order. Therefore, it is valid to assume that the resonant frequencies of the two systems would be significantly different; thus, the piezoelectric element would not be coupled with the frequency of the stator. As a consequence of the large difference in resonance frequencies between the piezoelectric element and the stator, the piezoelectric element acts to deliver a harmonic force that parametrically excites the resonance of the stator, while the consequent resonant vibration of the stator has negligible effect on the piezoelectric element's motion. This is the reason for the free-free assumption used here and the close correspondence between FEM-computed and experimentally measured resonance frequencies in Sec. IV B supports this decision. If the proposed modeling methods were to be used for other cases, the boundary conditions for the finite element model would have to be examined in each case.

From the FEM, the first two axial and torsional resonant frequencies were semiautomatically determined using a modified version of the method developed by Friend *et al.*<sup>12</sup> For the third harmonic and higher resonances, the highly nonlinear behavior of the system makes specific mode shapes difficult to determine.

#### D. HSM

##### 1. Spring stiffness

The seminal equation for the axial and torsional spring stiffness of a helical spring was developed by Wittrick.<sup>13</sup> Using an energy balance and the free-body diagram illustrated in Fig. 2, Wittrick arrived at the expression for the equivalent axial spring stiffness to be

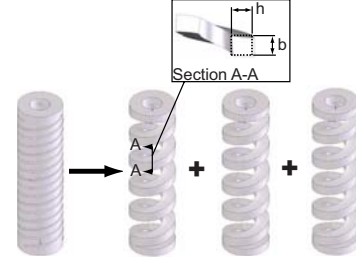


FIG. 3. (Color online) To use the calculation proposed by Wittrick (Ref. 13) to determine the axial and torsional stiffness, the stator is decomposed into a set of helical springs, with the cross-section approximated by a rectangle of dimensions  $b$  and  $h$ .

$$K_{se} = \frac{\beta_T \cos^2(\alpha) + \beta_1 \sin^2(\alpha)}{LR}, \quad (11)$$

and the equivalent torsional spring stiffness to be

$$K_{sr} = \frac{\beta_1 \cos^2(\alpha) + \beta_T \sin^2(\alpha)}{L}, \quad (12)$$

where  $\beta_T$  is the torsional modulus of the spring cross-section,  $\beta_1$  is a bending modulus of the spring cross-section,  $\alpha$  is the pitch angle of the spring,  $L$  is the total length of wire in the spring, and  $R$  is the radius of the spring.

Implicit in the derivation of Eqs. (11) and (12) are three assumptions: that the spring cross-section is doubly symmetric, that the spring is wound in such a way that one of the two center lines of every cross-section is normal to the surface of the cylinder of radius  $R$ , and that cross-sectional dimensions of the spring are small when compared with the radius of curvature  $R \sec^2(\alpha)$  of the helix. The last assumption can be expressed more formally as

$$\gamma^2 \ll 1, \quad (13)$$

where  $\gamma$  is defined as

$$\gamma = \frac{R}{k_T} \sec^2 \alpha, \quad (14)$$

in which  $k_T$  is the polar radius of gyration of the spring cross-section.

##### 2. Application of Wittrick's stiffness model

To use Wittrick's model to calculate an equivalent stiffness in our model, we decompose the stator into the same number of identical springs as there are number of cuts ( $N_c$ ). The cross-section of each spring is determined by approximating the remaining tube wall material as a rectangle, as shown in Fig. 3.

Using the nondimensional geometric parameters outlined in Eqs. (3) and (4), we can calculate  $b$  and  $h$  to be

$$b = \left[ \frac{D_o}{N_r N_s \cos(\alpha)} \right] \left\{ 0.9 L_z^* - \left[ \frac{C^*}{\cos(\alpha)} \right] (N_r N_s + 1) \right\}, \quad (15)$$

$$h = \frac{D_o(1 - D_i^*)}{2}, \quad (16)$$

respectively, in which  $\alpha$  can be determined from

$$\alpha = \tan^{-1}\left(\frac{0.9L_z^*}{\pi N_r}\right). \quad (17)$$

Having determined  $b$  and  $h$ , we can explicitly write expressions for the rest of the variables to determine  $K_{se}$  and  $K_{sr}$  for one of the system springs,

$$\beta_T = G \left[ \frac{bh}{12}(b^2 + h^2) \right], \quad (18)$$

$$\beta_1 = E \left( \frac{bh^3}{12} \right), \quad (19)$$

$$R = \frac{D_o}{4}(1 + D_i^*). \quad (20)$$

We can also write an expression for  $k_T$  that will allow us to calculate  $\gamma$  using Eq. (14)

$$k_T = \frac{\sqrt{b^2 + h^2}}{2\sqrt{3}}. \quad (21)$$

The total stiffness of the stator can then be recovered using the parallel spring theorem

$$K_n = N_c K_{sn}, \quad (22)$$

where  $K$  is the stiffness of the stator;  $N_c$  is the number of cuts;  $K_s$  is the stiffness of the spring; when the  $n$  subscript is replaced by  $e$  throughout, we are referring to the axial resonance; and when  $r$  replaces  $e$ , we are referring to the torsional resonance. In the above, we have assumed that the small uncut sections of the stator ( $0.05L_z$  long at each end) are much stiffer than the equivalent spring stiffness and have ignored these in the stiffness calculation.

## E. PSM

### 1. FEM derived stiffness

To generate a function for the pseudoaxial and the pseudotorsional stiffness and to subsequently determine the associated resonant frequencies, we calculate the stator stiffness from the finite element model using the parameter space outlined in Table I. The stator stiffness is calculated from the FEM using a ratio of the resonant frequency of the stator and the resonant frequency of an uncut tube using Eqs. (5) and (8). This ratio leads to

$$K_{eth} = \left( \frac{\omega_{eth}}{\omega_{et}} \right)^2 \left( \frac{M_{th}}{M_t} \right) K_{et} = \omega_e^{*2} M^* K_{et} \quad (23)$$

and

$$K_{rth} = \left( \frac{\omega_{rth}}{\omega_{rt}} \right)^2 \left( \frac{I_{zth}}{I_{zt}} \right) K_{rt} = \omega_r^{*2} I_z^* K_{rt}, \quad (24)$$

where  $K$  is the stiffness and  $\omega$  is the resonant frequency,  $e$  in the subscript refers to the axial calculation,  $r$  refers to the torsional calculation,  $t$  refers to the uncut tube, and  $th$  refers to the helically cut tube (the stator).  $M_{th}$  is the stator mass

TABLE I. The parameter space used throughout the paper to validate and compare the models under investigation. Note:  $\alpha$  is related to  $N_r$  by Eq. (17).  $D_o$  is the outside diameter,  $E$  is the Young's modulus, and  $G$  is the shear modulus of a stainless steel 32-gauge tube, the smallest commercially available stainless steel tubing.

Parameter	Low	High	Step size
$D_o$	0.24 mm	0.24 mm	...
$D_i^*$	0.25	0.75	0.25
$L_z^*$	2	6	2
$C^*$	0.04	0.08	0.02
$N_r$	2	5	1
$N_c$	2	4	1
$E$	193 GPa	193 GPa	...
$G$	57.9 GPa	57.9 GPa	...

which can be found using Eq. (6) and  $I_{zth}$  is the stator second moment of area which can be found using Eq. (9).  $K_{at}$ ,  $K_{rt}$ ,  $\omega_{at}$ ,  $\omega_{rt}$ ,  $M_t$ , and  $I_{zt}$  can be found using the standard equations for a free-free cylindrical tube.<sup>6</sup> These stiffnesses are then nondimensionalized using Eqs. (3) and (4).

We note there are two inherent assumptions in this analysis. First, that the static stiffness of the uncut tube  $K_{at}$  and  $K_{rt}$  can be used to find the effective dynamic stiffness of the stator  $K_{eth}$  and  $K_{rth}$  without introducing a large error. Second, that the difference in mode shape, and thus the effective inertia, of the stator and uncut tube in negligible allow the ratios  $M_{th}/M_t$  and  $I_{zth}/I_{zt}$  to be used.

## 2. Pseudostiffness

To generate the pseudostiffness function, we curve-fit the nondimensionalized parameters in Eqs. (3) and (4) against the FEM stiffness derived using Eqs. (23) and (24). We explicitly get

$$K_{nth}^* = f\{D_i^*, C^*, N_c, \alpha, L_z^*\}, \quad (25)$$

where when the  $n$  subscript is replaced by  $e$  throughout, we are referring to the axial resonance, and when  $r$  replaces  $e$ , we are referring to the torsional resonance. By fitting a curve to each parameter in turn and improving the least-squares fit toward an ideal of  $y=x$  and a coefficient of determination of  $R^2=1$ , we get the following equations for the pseudostiffness:

$$K_{peth}^* = 0.0135[\cos(D_i^*)^{11.6}](\alpha^{2.5})(L_z^{-1})(N_s^{-1.5})(C^{*-0.58}) \quad (26)$$

and

$$K_{prth}^* = 0.0135[\cos(D_i^*)^{11.684}](\alpha^{1.8})(L_z^{-1})(N_s^{-0.55})(C^{*-0.5}), \quad (27)$$

which can be used to collapse the data, as shown in Fig. 4, where  $y=0.9998x$  with  $R^2=0.88$  for the axial stiffness and  $y=0.9976x$  with  $R^2=0.98$  for the torsional stiffness, which demonstrates good agreement with the stiffness calculated using the FEM. We believe the difference in correlation between the axial stiffness  $R^2=0.88$  and the torsional stiffness  $R^2=0.98$  arises from the assumption in the derivation of the stiffness from the FEM, as defined in Sec. II E 1. Specifi-

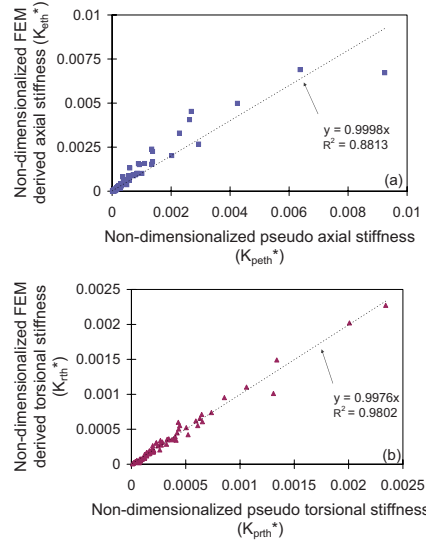


FIG. 4. (Color online) Collapse of (a) the axial pseudostiffness and (b) the torsional pseudostiffness data, using the scaling in Eqs. (26) and (27), respectively, showing good agreement with the stiffness calculated from the FEM.

cally, the effective mass and axial stiffness of the stator is more effected by changes to the geometric parameters than the effective second moment of inertia and torsional stiffness. This is highlighted by limiting  $\alpha < 0.5$ , where the correlation for the axial stiffness improves to  $R^2 = 0.88$  and the correlation for the torsional stiffness decreases slightly to  $R^2 = 0.95$ . However, to provide the largest parameter range for design, we do not apply the restriction of  $\alpha < 0.5$  to the model.

### III. MODEL RESULTS AND DISCUSSION

#### A. Model correlation

We investigate how well the HSM captures the actual characteristics of the geometric system by comparing the HSM-generated resonant frequencies (Secs. II B and II D 2) with resonant frequency data obtained from the finite element model (Sec. II C) over the parameter space outlined in Table I. By performing a linear regression on these sets of data, it is possible to obtain an indication of how well the HSM models the stator. Figure 5 shows a good approximation of the stator's resonant frequencies with a least-squares fit of  $y = 0.875x$  with a  $R^2$  value of 0.8031.

To examine possible errors in the model, we review the assumptions inherent in Wittrick's spring stiffness model and outlined in Sec. II D 1. From the design, we know that the equivalent springs are "wound" in such a way that one of the two center lines of every cross-section is normal to the surface of the cylinder. For all cases, the maximum  $\gamma^{-2}$  value we find is 0.31, which is acceptable for the assumption  $\gamma^{-2} \ll 1$ . A ratio of  $b/h = 1$  indicates a doubly symmetric cross-

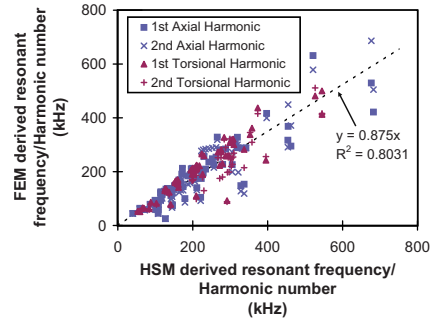


FIG. 5. (Color online) The least-squares fit of the comparison between the HSM and FEM derived resonant frequencies.

section. Calculating the  $b/h$  ratio for the parameter space in Table I, we find a minimum of ratio of 0.1 and a maximum of 7.59.

An aspect ratio range of  $0.1 < b/h < 7.59$  is significantly outside the ratio of 1 required by Wittrick's model. To examine the effect of this, we progressively limit the cases that are included in the least-squares analysis to those that have parameters that result in a  $b/h$  within certain boundaries. These results are tabulated in Table II.

We find limiting the ranges of aspect ratio in the HSM provides a distinct improvement in the correlation. We also note that there is little change in the effectiveness of the model from a small range ( $0.9 < b/h < 1.1$ ) to a range of  $0 < b/h < 2$  or an error of 100%. We find that the parameters that result in a  $b/h$  ratio outside of the range  $0 < b/h < 2$  are those that have a thin tube wall (a high  $D_i^*$ ) and those that have a large pitch angle ( $\alpha$  approximately greater than 0.5) while having a low number of cuts ( $N_c = 2$ ).

From these results we can determine some important points. First, by using this simplified modeling technique, it is possible to accurately model the resonant frequencies of the system. Second, the simple calculation allows an intuitive understanding of how the physics of the system works. For example, an increase in the pitch angle affects both the

TABLE II. Limiting the parameter cases to ranges of the aspect ratio demonstrates the effect that violating Wittrick's assumption  $b/h = 1$  has on the HSM accuracy (Ref. 13). Note the number of data points for each least-squares analysis was four times the number of cases signifying two harmonics for two resonant modes.

$b/h$ range	Number of cases	Least-squares fit constant	$R^2$
All parameter cases	72	0.875	0.8031
0.1–7.59			
0.9–1.1	5	0.9676	0.9136
0.75–1.25	20	0.9825	0.8953
0.5–1.5	37	0.9975	0.8859
0.25–1.75	47	1.0034	0.8683
0–2	58	1.0284	0.8819
0–3	65	1.0647	0.8642
0–4	68	1.0755	0.8511

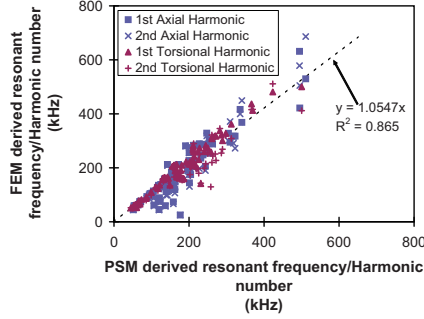


FIG. 6. (Color online) Comparison of the axial and torsional resonant frequencies calculated using the PSM and those obtained using the FEM.

moment of inertia of the spring cross-section and the applied loading. Last, we find the interesting result that as a design tool, the model for equivalent spring stiffness derived by Wittrick can be applied to a much greater range of problems than the original strict definition of  $b/h=1$  suggests.

Using the calculations in Secs. II B and II E to determine the resonant frequencies, the same technique can be used to determine how well the PSM models the system. Figure 6 shows the correlation between the PSM and the FEM is comparable with the best correlation obtained when comparing the HSM and the FEM.

The benefit of the PSM is obvious in two areas. First is the generality of the model. The technique can be used for any single component complex geometrical system without constraints from analytical assumptions. Second, the function quickly shows how important a parameter is to the calculation. This ensures that time is spent most effectively during design. The model is, however, inferior to the HSM in that it does not provide an understanding of the underlying physics of the system and cannot provide information beyond the original task (in this case the calculation of the axial and torsional resonant frequencies).

### B. Matching resonant frequencies

For the axial and torsional resonant frequencies to be matched, the ratio must equal 1. From this we write

$$\frac{\omega_e}{\omega_r} = \left( \frac{K_a}{M} \right) \left( \frac{I_z}{K_r} \right) = 1. \quad (28)$$

Using Eq. (28) to first examine the HSM, we find that the external diameter  $D_o$  has no effect on whether the axial and torsional resonances can be matched. Although more complicated, we also find that the nondimensional length  $L_z^*$  plays little part in enabling the matching of axial and torsional resonant frequencies. Figure 7 shows a typical contour plot of  $\omega_e/\omega_r=1$  against the stator length  $L_z^*$ , pitch angle  $\alpha$ , and number of cuts  $N_c$ . We see that for any combination of  $\alpha$  and  $N_c$  that achieves  $\omega_e/\omega_r=1$ , making changes in  $L_z^*$  has no effect. We also note that for  $N_c \geq 3$ , it is possible to achieve a ratio of one for more than one value of  $\alpha$ . For the solution that uses a small value of  $\alpha$ , it can be seen that the model

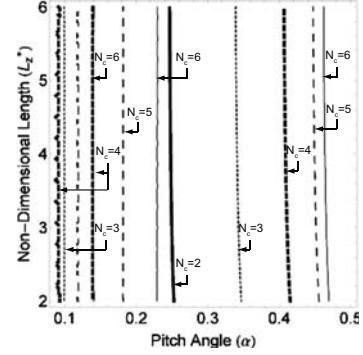


FIG. 7. A typical contour plot of a unity ratio of axial to torsional resonant frequency  $\omega_e/\omega_r=1$  against nondimensional length  $L_z^*$ , pitch angle  $\alpha$ , number of cuts  $N_c$  for nondimensional cut width  $C^*=0.06$ , and nondimensional internal diameter  $D_i^*=0.458$ .

breaks down as the value of equivalent spring breadth  $b$  nears zero resulting in the broken lines.

Having noted that  $D_o$  and  $L_z^*$  play little part in being able to match the axial and torsional resonant frequencies, we now focus on the remaining four geometric parameters  $C^*$ ,  $D_i^*$ ,  $\alpha$ , and  $N_c$ . Figure 8(a) plots how the relationship between the parameters varies to ensure  $\omega_e/\omega_r=1$ . We see that we have a set of curved shells, with the curve being projected in the  $\alpha$ - $C^*$  plane. By plotting only the  $\alpha$ - $C^*$  plane for a nominal value of  $D_i^*=0.458$ , we can more closely examine the projected curves, as shown in Fig. 9(a). What we note is that the curves get shorter and more rounded as the value of  $N_c$  increases. This means that for  $N_c=2$ , only a small change in the pitch angle is required for a large change in the nondimensional cut width to ensure a ratio of one is achieved. This is not the case for the higher cases of  $N_c$  where a much larger change in  $\alpha$  is required.

In Fig. 10(a), we observe that as  $N_c$  gets larger, the change in  $C^*$  required for a given change in  $D_i^*$  gets smaller. Therefore, for a small number of cuts, the change in the nondimensional cut width required to account for any manufacturing changes to the internal diameter would be much greater than for a larger number of cuts.

Figure 11(a) demonstrates that for low values of  $N_c$ , only a small change in  $\alpha$  is required to offset any changes in  $D_i^*$ . However, as the number of cuts increases,  $D_i^*$  becomes more dominant to the point where, for  $N_c=6$ , the axial and torsional resonant frequencies cannot be matched for a stator with a thick wall.

Carrying out the same investigation using the PSM, we find that we can more clearly determine that the outside diameter  $D_o$  and the length  $L_z^*$  can be ignored when matching the axial and torsional resonant frequencies. Comparing the results for the HSM and the PSM in Figs. 8(a) and 8(b) shows that, in general, both models produce the same trends, with a set of shells curved in the  $\alpha$ - $C^*$  plane.

The two models have some key differences in the changes in relationship necessary to maintain an axial-torsional frequency ratio of one. In Fig. 10, we note that the



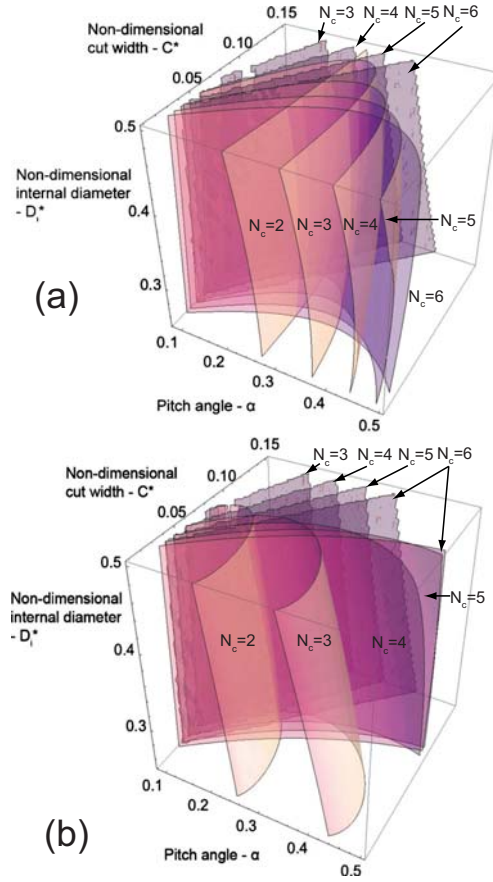


FIG. 8. (Color online) 3D contour plot demonstrating the relationship between the pitch angle, the number of cuts, the nondimensional cut width, and the nondimensional internal diameter to ensure a unity ratio of axial to torsional resonant frequency  $\omega_a/\omega_t = 1$  for (a) the HSM and (b) the PSM. A nominal value of  $L_s^* = 3.8$  has been used for the calculation; colors are for visualization only.

PSM predicts that a larger cut width is required for a given internal diameter than the HSM. Also, the path for  $N_c = 2$  line is significantly different between the two models, which could arise from the error in the HSM when  $b/h \gg 1$ . The error in the HSM for aspect ratios significantly different from one may also explain the differences we see in the higher numbered cut lines in Figs. 11(a) and 11(b). From Fig. 11(b), we also note that the pitch angle is a much more dominant factor in the PSM than the HSM, while Fig. 9 shows an opposite effect, with the pitch angle being less important in the  $\alpha$ - $C^*$  relationship for the PSM than for the HSM. In summary, we note for an intermediate number of cuts ( $N_c = 3-5$ ), the two models produce similar trends on how we can match the axial and torsional resonant frequencies.

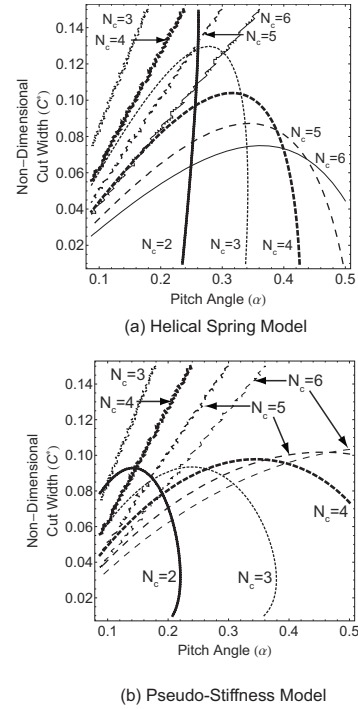


FIG. 9. Parametric relationship for the pitch angle  $\alpha$ , the nondimensional cut width  $C^*$ , number of cuts  $N_c$  for a nondimensional internal diameter of  $D_i^* = 0.458$ , and a nondimensional stator length  $L_s^* = 3.8$  for (a) the HSM and (b) the PSM.

#### IV. PROTOTYPE MICROMOTOR

##### A. Micromotor parameters

The piezoelectric ultrasonic prototype micromotor setup is shown in Fig. 12. The micromotor uses a large piezoelectric element to excite the matched axial and torsional resonant modes in the stator, creating the desired motion in the rotor.<sup>3</sup> The parameters for the stator we have available for testing are listed in Table III. The stator tube is made from 32-gauge 304 stainless steel.

##### B. Finite element model validation

Both the HSM and the PSM have been shown to produce axial and torsional resonant frequencies that correlate well with a finite element model. To validate the finite element model, we compare axial, torsional, and bending resonant frequencies of Stator 1 calculated by FEM with resonances measured using a laser Doppler vibrometer (LDV) (MSA-400, Polytec GmbH, Waldbronn, Germany). The motor used for the measurements was as outlined in Sec. IV A, with the rotor removed to enable measurement at the required points on the stator tip.

To capture the resonant frequencies, we record the out-of-plane displacement spectra for six points on the stator tip, with the measurement positions shown in Fig. 13(b) resulting

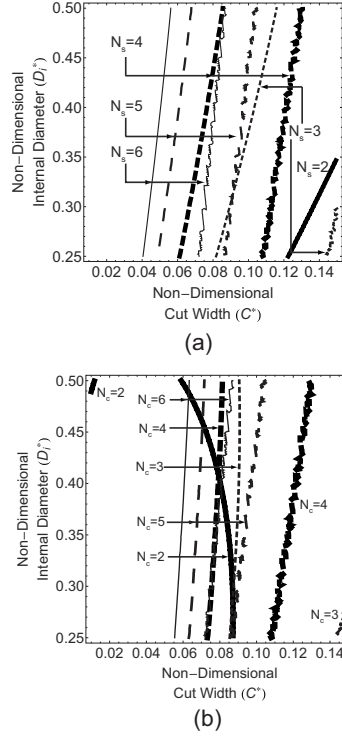


FIG. 10. Parametric relationship for the nondimensional internal diameter  $D_i^*$ , cut width  $C^*$ , number of cuts  $N_c$  for a pitch angle of  $\alpha=0.2$ , and a nondimensional cut length of  $L_c^*=3.8$  for (a) the HSM and (b) the PSM.

in the spectra shown in Fig. 13(a). We then use the method outlined by Friend *et al.*<sup>12</sup> to characterize and record the resonant frequencies, which are shown in Fig. 13(a). These measurements demonstrate an average error of less than 10% between the FEM and the measured resonant frequencies, thus validating the FEM model.

### C. Micromotor performance

To test the micromotor performance, we use Stator 2 as outlined in Table III. Using a signal generator and amplifier (Rohde & Schwarz-SML 01 and NF-HSA 4501, North Ryde, New South Wales, Australia), the PZT element was driven at each of the trial frequencies, which included each of the finite element model derived axial and torsional resonant frequencies using a bandwidth of  $\pm 5\%$  to allow for manufacturing tolerances.

The micromotor demonstrated bidirectional operation with clockwise rotation at the third harmonic (732 kHz) and counterclockwise rotation at the second harmonic (526 kHz). Micromotor performance was determined using the method by Nakamura *et al.*<sup>14</sup> Rotor motion was recorded using a laser Doppler velocimeter (Canon LV-20Z, Utsunomiya, Japan). A maximum clockwise angular velocity of 830 rad/s (7925 rpm) was recorded at an input of 20  $V_{p-p}$  and 732

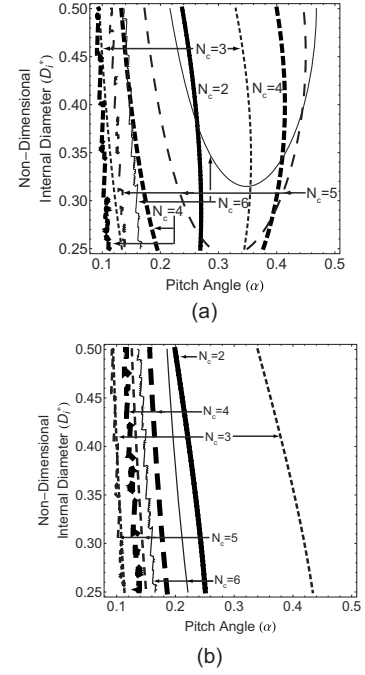


FIG. 11. Parametric relationship for the nondimensional internal diameter  $D_i^*$ , the pitch angle  $\alpha$ , the number of cuts  $N_c$  for a nondimensional cut width  $C^*=0.06$ , and a nondimensional length  $L_c^*=3.8$  for (a) the HSM and (b) the PSM.

kHz. Based on the curve in Fig. 14, the average clockwise start-up torque was 47 nNm with a peak of 51 nNm and a minimum of 39.8 nNm. The average braking torque was calculated to be 17.8 nNm. A maximum counterclockwise angular velocity of 1600 rad/s (15 280 rpm) at 32.1  $V_{p-p}$  and 526 kHz was recorded.

As a measure of the improvement in performance possible through the matching of axial and torsional resonant modes, the current test micromotor shows an increase in angular velocity of a minimum of 5.5 times across all runs

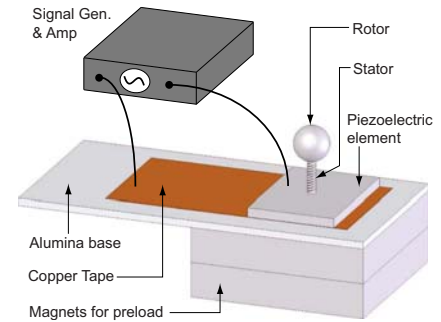


FIG. 12. (Color online) Schematic showing the test setup for the piezoelectric ultrasonic micromotor.



TABLE III. Parameters for the available test stators.

Parameter	Stator 1	Stator 2
Outside diameter ( $D_o$ )	241 $\mu\text{m}$	241 $\mu\text{m}$
Nondimensional inside diameter ( $D_i^*$ )	0.458	0.458
Nondimensional length ( $L_z$ )	3.8	3.8
Nondimensional cut width ( $C^*$ )	0.04	0.04
Pitch angle ( $\alpha$ )	0.214	0.302
Number of cuts ( $N_c$ )	2	3
Frequency ratio ( $\omega_r/\omega_e$ ) from HSM	0.86	0.91
Frequency ratio ( $\omega_r/\omega_e$ ) from PSM	0.88	0.99

when compared with our original micromotor that did not have matched axial and torsional resonant frequencies.<sup>8</sup> In addition to angular velocity, the start-up torque increased by a minimum of three times. During the performance measurement in both micromotors, the preload was modified to ensure that maximum performance was achieved.

### V. CONCLUSIONS

We have demonstrated the use of two simple, novel modeling techniques to examine the effect of changes in geometric parameters on the axial and torsional resonant frequencies of a complex nonlinear system. The first model, the HSM, decomposes the system into simpler, well-understood components giving an accurate analytical model of the system. The second model, the PSM, uses scaling techniques to produce a model that reduces computational time and improves insight into the system when compared with the use of the FEM alone. The pseudostiffness technique in particular shows great potential as a generalized tool for the analysis and design of a multitude of complex nonlinear mechanical systems. Due to the simplicity of the methodology, almost any system that can be accurately modeled using a FEM could be analyzed with the PSM. The methodology could be applied to other systems where the resonant vibration is important such as other ultrasonic motor designs, microcantilever beam designs, or possibly other classes of motors such as electrostatic. Moreover, the methodology may be used to investigate other parameters, such as the output force or tip displacement of thermal actuators.

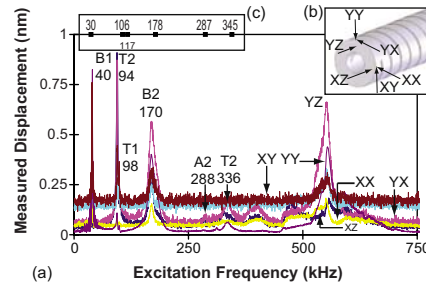


FIG. 13. (Color online) Comparison of stator resonant frequencies obtained from (a) LDV-recorded out-of-plane displacement spectra, using the measurement positions detailed in (b), and (c) finite element model-calculated frequencies for the stator detailed in Stator 1 of Table III.

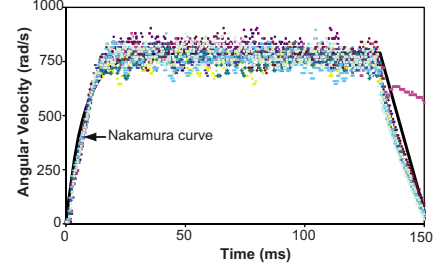


FIG. 14. (Color online) Angular velocity as a function of time, for a test micromotor with closely matched axial and torsional resonant frequencies. A step voltage of 20  $V_{p-p}$  and an operating frequency of 732 kHz was used. The fitted curve is derived from the method by Nakamura *et al.* (Ref. 14) and is the average obtained across all runs.

Using the two models for a specific test case of a piezoelectric ultrasonic micromotor with helical stator geometries, we were able to map the parametric relationships that ensure all axial and torsional modes are matched. This exercise demonstrated that the outside diameter and stator length were unimportant when trying to match axial and torsional resonant frequencies, whereas strong dependence on the cut width and pitch angle were observed.

We demonstrated that a prototype micromotor with closely matched resonant frequencies had a significant improvement in performance over an existing prototype upon applying this knowledge.

### ACKNOWLEDGMENTS

This work was made possible in part by Grant Nos. SM/07/1616 and SM/06/1208 from the CASS Foundation, Grant No. DP0773221 from the Australian Research Council, and the New Staff and Small Grant Scheme funds from Monash University. This work was performed in part at the Macquarie/ATP node of the Australian National Fabrication Facility, a company established under the National Collaborative Research Infrastructure Strategy to provide nanofabrication and microfabrication facilities for Australia's researchers.

- <sup>1</sup> C. J. Morris and F. K. Forster, *J. Microelectromech. Syst.* **12**, 325 (2003).
- <sup>2</sup> K. M. Hansen and T. Thundat, *Methods* **37**, 57 (2005).
- <sup>3</sup> B. Watson, J. Friend, and L. Yeo, *Sens. Actuators, A* **152**, 219 (2009).
- <sup>4</sup> J. Friend, L. Yeo, and M. Hogg, *Appl. Phys. Lett.* **92**, 014107 (2008).
- <sup>5</sup> S. Subramanian and N. Gupta, *J. Phys. D: Appl. Phys.* **42**, 185501 (2009).
- <sup>6</sup> S. S. Rao, *Mechanical Vibrations* (Addison-Wesley, Reading, 1995).
- <sup>7</sup> B. Kang, C. H. Riedel, and C. A. Tan, *J. Sound Vib.* **260**, 19 (2003).
- <sup>8</sup> B. Watson, J. Friend, and L. Yeo, *J. Micromech. Microeng.* **19**, 022001 (2009).
- <sup>9</sup> K.-C. Liu, J. Friend, and L. Yeo, *J. Sound Vib.* **321**, 115 (2009).
- <sup>10</sup> B. R. Munson, D. F. Young, and T. H. Okiishi, *Fundamentals of Fluid Mechanics* (Wiley, New York, 1998).
- <sup>11</sup> R. G. Grimes, J. G. Lewis, and H. D. Simon, *SIAM J. Matrix Anal. Appl.* **15**, 228 (1994).
- <sup>12</sup> J. Friend, K. Nakamura, and S. Ueha, *IEEE Trans. Ultrason. Ferroelectr. Freq. Control* **51**, 870 (2004).
- <sup>13</sup> W. H. Wittrick, *Int. J. Mech. Sci.* **8**, 25 (1966).
- <sup>14</sup> K. Nakamura, M. Kurosawa, H. Kurebayashi, and S. Ueha, *IEEE Trans. Ultrason. Ferroelectr. Freq. Control* **38**, 481 (1991).

# The Modelling and Testing of a Piezoelectric Ultrasonic Micro-Motor Suitable for an In Vivo Micro-Robot

*This chapter demonstrates the final iteration of the motor design methodology developed in this thesis and the size and performance of the prototype motor that results. This iteration extends the pseudo-stiffness model introduced in Chapter 3 to model all components of the motor, including the epoxy bonds. This facilitates a motor design that closely matches the axial, torsional and electro-mechanical resonant frequencies of the motor. Closely matching these three resonant frequencies improves the performance of the motor over previous prototypes. The resulting design includes a stator diameter of 241  $\mu\text{m}$  and an overall diameter of 400  $\mu\text{m}$ , as determined by the commercial availability of components. A motor fabricated as close as possible to design specifications produced a start-up torque of 23.8  $\text{nNm/mm}^2$  and a peak output power of 5  $\mu\text{W/mm}^2$  using a preload of 46.6  $\mu\text{N}$ . Increasing the preload on the motor to 2264  $\mu\text{N}$  improved this performance to 230.4  $\text{nNm/mm}^2$  and 76.5  $\mu\text{W/mm}^2$ . These results meet the geometric and performance requirements for a motor to drive a tetherless micro-robot within the human body.*

Chapter 3 demonstrated the performance gain that can be achieved in a piezoelectric ultrasonic motor by ensuring that the resonant frequencies of the stator are closely matched. The resulting performance of  $64 \text{ nNm/mm}^2$  and  $13.5 \mu\text{W/mm}^2$ , when normalised by the cross-sectional area of the 1 mm diameter rotor, was a significant improvement over the first prototype outlined in Chapter 2. However, the output power of this motor is only approximately 20% of the requirement outlined in Table 1.1 and the dimensions of the rotor, piezoelectric element and preload components are too large for the desired application.

To improve the performance and reduce the geometric dimensions of the motor, the modelling techniques in Chapter 3 need to be extended to include all motor components. By including all the components in the model, it becomes possible to match not only the axial and torsional resonant frequencies, but also the electro-mechanical resonant frequency of the system. By operating at the electro-magnetic resonance of the system we can achieve the largest response from the piezoelectric element, resulting in a further increase in motor performance. Moreover, the inclusion of all the components in the model allows control of the component sizing to ensure the geometric requirements are met.

The paper reproduced in this chapter has two main foci. The first is the extension of the pseudo-stiffness model introduced in Chapter 3 to produce a modelling technique that provides an insight into how the parameters from all the motor components affect the axial, torsional and electro-mechanical resonant frequencies of the system. From the resulting model, it was possible to determine a design space for the motor that closely matched the three resonant frequencies of interest. The prototype used helical grooves in the stator in place of the helical

cuts of previous prototypes. This allowed the fundamental axial, second harmonic torsional and the electro-mechanical resonant frequencies to be matched to within 0.5%.

The second focus was to produce a prototype motor using the generated design and determine the motor performance. The fabricated prototype has a stator dimension the same as previous prototypes, a rotor diameter of 0.25 mm and an overall diameter of 0.4 mm. The large overall diameter arose due to the commercial availability of a magnetic element. As designed, the motor produced  $23.8 \text{ nNm/mm}^2$  and  $5 \text{ } \mu\text{W/mm}^2$  using a preload of  $46.6 \text{ } \mu\text{N}$ . An increase in preload to  $2264 \text{ } \mu\text{N}$  resulted in an increase in performance to  $230.4 \text{ nNm/mm}^2$  and  $72.4 \text{ } \mu\text{W/mm}^2$ , both well in excess of the performance requirement outline in Section 1.3.

From the results, we conclude that with modifications to the preload of the system it would be possible to produce a motor that would meet all the requirements to act as a drive system in a tetherless *in vivo* microbot.

# Modelling and Testing of a Piezoelectric Ultrasonic Micro-Motor Suitable for *In Vivo* Micro-Robotic Applications

**Brett Watson**, James Friend and Leslie Yeo

*Journal of Micromechanics and Microengineering*

Revisions in review (revisions included herein), 19 July 2010

## Declaration for Thesis Chapter 4

### Declaration by candidate

In the case of Chapter 4, the nature and extent of my contribution to the work was the following:

Nature of contribution	Extent of contribution (%)
I was chief investigator for this work. I was responsible for the development of the modelling techniques, motor assembly, experimental work, interpretation of results and the writing of the paper.	80

The following co-authors contributed to the work.

Name	Nature of contribution
Professor James Friend	Overall supervision, review of drafts and submission of paper to journal.
Associate Professor Leslie Yeo	Overall supervision and review of drafts.

	Date
Candidate's Signature	

### Declaration by co-authors

The undersigned hereby certify that:

- (1) the above declaration correctly reflects the nature and extent of the candidate's contribution to this work, and the nature of the contribution of each of the co-authors.
- (2) they meet the criteria for authorship in that they have participated in the conception, execution, or interpretation, of at least that part of the publication in their field of expertise;
- (3) they take public responsibility for their part of the publication, except for the responsible author who accepts overall responsibility for the publication;
- (4) there are no other authors of the publication according to these criteria;
- (5) potential conflicts of interest have been disclosed to (a) granting bodies, (b) the editor or publisher of journals or other publications, and (c) the head of the responsible academic unit; and
- (6) the original data are stored at the following location(s) and will be held for at least five years from the date indicated below:

Location(s)	Department of Mechanical and Aerospace Engineering, Monash University, Clayton, Victoria, Australia.
-------------	--

	Date
Signature 1	
Signature 2	

## Modelling and testing of a piezoelectric ultrasonic micro-motor suitable for *in vivo* micro-robotic applications

B Watson, J Friend and L Yeo

Micro/Nanophysics Laboratory, Department of Mechanical and Aerospace Engineering, Monash University, Wellington Road, Clayton, VIC 3800 Australia

E-mail: james.friend@eng.monash.edu.au

### Abstract.

A piezoelectric ultrasonic resonant micro-motor is developed with a stator diameter of  $241\ \mu\text{m}$  and an overall diameter of  $400\ \mu\text{m}$ . The motor is shown to produce a start-up torque of  $1.2\ \text{nNm}$  and a peak output power of  $0.25\ \mu\text{W}$  as designed, with a preload of  $46.6\ \mu\text{N}$ . An increase in preload to  $2264\ \mu\text{N}$  improved performance to a start-up torque of  $29\ \text{nNm}$  and a peak output power of  $9.1\ \mu\text{W}$ . The motor is five times smaller than the current smallest piezoelectric ultrasonic resonant motor produced by Kanda et al.. The motor is designed to operate at approximately  $771\ \text{kHz}$ , matching the fundamental axial, second harmonic torsional and electro-mechanical resonant frequencies. This is achieved through the use of a novel design process that uses scaling theories to greatly reduce the computational time to design the device. The resultant size and performance of the motor makes it the first motor design capable of meeting the requirements of a drive system in a tetherless swimming *in vivo* micro-robot.

PACS numbers: 07.10.Cm, 85.85.+j, 87.80.Ek, 87.85.Ox, 46.40.-f, 43.38.+n, 43.35.+d

Submitted to: *J. Micromech. Microeng.*

### 1. Introduction

The use of minimally invasive surgery has resulted in a reduction in trauma, pain and recovery times for patients [1, 2, 3]. However, from the perspective of the surgeon, minimally invasive surgery is really minimal *access* surgery [1]. The reduced access afforded by the small incision limits perception, reduces dexterity, increases strain and the likelihood of error [4, 5, 6]. To overcome this, researchers are working towards a tetherless micro-robot (microbot) capable of conducting medical procedures within the human body. Tetherless microbots could revolutionise medicine, being potentially cheaper, less painful and more flexible than existing minimally invasive surgery systems [7].

One of the major obstacles to realising such microbots is the availability of a practical micro-motor of the correct dimensions and performance to act as the drive system. As an example, the anterior cerebral artery is the smallest artery accessed for treatment with current catheter based operations. The geometric requirement of a drive system to operate in this artery is on the order of  $200\text{ }\mu\text{m}$ . To be able to move upstream in the same artery requires a start-up torque of  $15\text{ nNm/mm}^2$  and an output power of  $65\text{ }\mu\text{W/mm}^2$ , with the frontal area of the robot as the normalising area [8].

An examination of the driving force that is used as the basis-of-design of current micro-motor classes [9], demonstrates that the favourable scaling characteristics, high torque/low speed outputs and simple construction of piezoelectric ultrasonic resonant motors (PURM's) hold more promise for meeting these requirements compared to other well known motor classes, such as electrostatic [10] and electromagnetic [11] motors. Although PURM's have been tested at the millimeter scale [10, 12], a PURM that meets the geometric and performance requirements outlined above has yet to be developed.

In this paper we demonstrate a PURM that essentially meets these requirements for the first time. This is achieved by simultaneously matching the axial, torsional and electro-mechanical resonances of the device. The axial and torsional resonances are taken to be the resonant frequency at which the motion associated with the vibration mode shape of the motor is purely axial (along the length of the motor) or torsional (with the rotation axis along the length of the motor), respectively. The electro-mechanical resonance is the frequency where the system electrical impedance is at a minimum. The matched resonances result from a design process that uses an extended version of a modelling technique introduced previously [13] that utilises scaling arguments to greatly reduce computational time and provides an improved insight to the system, when compared with traditional finite element modelling. The stator design is derived from an earlier practical, though ultimately unsatisfactory prototype [14], and uses helical grooves in a cylindrical stator to couple the axial, torsional and electro-mechanical resonant modes of the system. The resulting prototype has a stator diameter of  $241\text{ }\mu\text{m}$ , an overall diameter of  $400\text{ }\mu\text{m}$ . With a preload of  $2264\text{ }\mu\text{N}$ , the performance figures achieved are  $230.4\text{ nNm/mm}^2$  and  $72.4\text{ }\mu\text{W/mm}^2$ . These performance figures meet the requirements, with the stator also approximately equal to the required dimension of  $200\text{ }\mu\text{m}$ . The overall diameter of  $400\text{ }\mu\text{m}$  is driven by the commercial availability of parts and could be reduced to the desired size without incurring significant performance losses. As the bespoke manufacturing of components is not the focus of this paper, this has not been carried out here.

## 2. Basis of Design

Piezoelectric ultrasonic resonant micro-motors use coupled resonant stator modes to produce an elliptical motion at the stator tip. Using a friction coupling, this cyclic motion can then be converted to a net motion of the rotor [15]. The area of micro-motors that research has been most focussed on is the class of motor that uses some



form of coupled resonant bending modes to produce the stator tip motion [9]. Use of the fundamental or lower harmonics of the bending modes in these designs results in a large stator tip displacement and desirable high torque/low speed characteristics. In general, however, this class of motor uses a stator entirely fabricated from a piezoelectric ceramic and requires multiple electrodes for the multiple electrical inputs. The need to fabricate a complex shaped stator, such as that proposed by Kanda et al. [16], out of a piezoelectric material whilst accurately and reliably fabricating multiple electrodes on the same component has proven to be an obstacle in achieving the dimensions required for use in a microbot.

In our previous work [14], we demonstrated that many of these obstacles could be circumvented by removing the piezoelectric element from the stator, and using it solely as a source of excitation for the coupled axial and torsional resonant modes of the helically cut stator. However, the performance of this prototype, and a subsequent prototype that had more closely matched stator resonant frequencies [13], did not meet the performance requirements outlined in Section 1. Moreover, the prototypes did not use either a piezoelectric element or a friction coupling method of a suitable scale for the desired application.

To address the problems associated with the previous designs, we devised two aims for this work. The first aim is to ensure that all components of the design are of a scale suitable for an *in vivo* microbot. This is achieved by using a piezoelectric element 250  $\mu\text{m}$  wide, 250  $\mu\text{m}$  deep and 500  $\mu\text{m}$  tall (C203 lead zirconate titanate, Fuji Ceramics, Tokyo, Japan) and by implementing an in-built magnetic preload for the friction coupling. The second aim is to improve the performance of the prototype to meet the requirements outlined in Section 1. This is to be achieved by ensuring the axial, torsional and electro-mechanical resonances of the system are matched. Operating the motor at a frequency that excites these three resonances simultaneously ensures the largest possible stator tip motion, directly correlated with improved motor performance.

To successfully match these frequencies, we will use two techniques. The first is the addition of a magnetic element to the system. This element is attached to the end of the piezoelectric element distal to the stator and has two functions, to reduce the electro-mechanical resonant frequency of the system and to provide a method of applying a preload to the rotor. The second technique is to use helical grooves in place of the helical cuts of the original prototype [14]. By not penetrating the tube wall of the stator, the stiffness of the stator is increased with little effect on the mass. This results in an increase in the axial and torsional resonant frequencies. Figure 1 illustrates the architecture and parameters for a prototype motor using these design techniques.

*Piezoelectric motor for a micro-robotic applications*

4

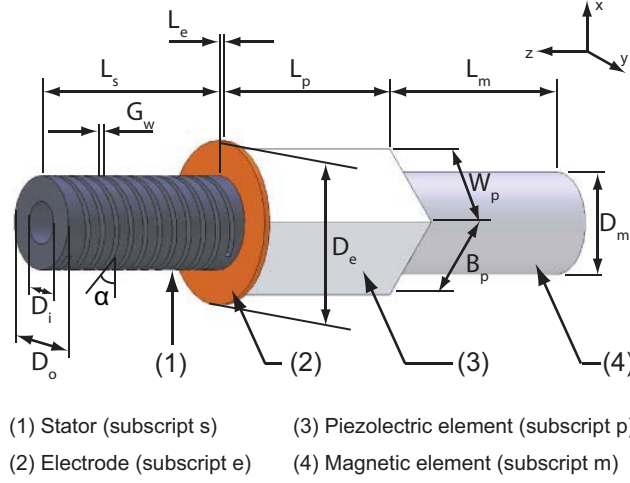


**Figure 1.** The prototype motor design uses helical grooves and a magnetic element as techniques to match the axial, torsional and electro-mechanical resonant frequencies of the system. The geometric parameters are as shown with each component also having a Young's modulus ( $E_x$ ), shear modulus ( $G_x$ ) and density ( $\rho_x$ ) to fully describe the system. The subscript  $x$  is replaced by the subscript associated with each component during the analysis.

### 3. Modelling

#### 3.1. The Pseudo-Function Method

The use of the techniques outlined in Section 2 requires an understanding of how the axial, torsional and electro-mechanical resonant frequencies are affected by changes to the system parameters. For this, a novel extension of the pseudo-stiffness method (PSM) introduced in [13], which we refer to as the pseudo-function method (PFM), is used. As with the PSM, the PFM uses scaling techniques to reduce the number of parameter cases necessary when using the finite element method (FEM) to produce a design. Additionally, it provides insight into the effects that result from changes to the system parameters that cannot be gained with FEM alone.

The PSM is a method to derive a system characteristic for a single component. The PFM extends this by modelling the system as a whole, allowing the effect of multiple components to be examined simultaneously. As with the PSM, the PFM derives a relationship that describes the effect changes in the system parameters have on the characteristic of interest (axial, torsional or electro-mechanical resonant frequency in the case of this paper). This is achieved by fitting each non-dimensional system parameter, in turn, against values of the characteristic calculated using a model created through FEM. By ensuring a least-squares fit with a coefficient of determination  $R^2$  as close as

possible to 1, the exponent for each parameter in the relationship can be determined.

An effective way to apply this method to model the axial and torsional resonant frequencies of this prototype motor is to analyse the stiffness and inertia of each component. We know that the axial resonant frequency must be a function of the axial stiffness and mass of each of the components, i.e.,

$$\omega_a = f(K_{as}, K_{ae}, K_{ap}, K_{am}, M_s, M_e, M_p, M_m) \quad (1)$$

where  $\omega_a$  is the fundamental axial resonant frequency,  $K_s$  is the axial stator stiffness,  $K_{ae}$  is the axial electrode stiffness,  $K_{ap}$  is the axial stiffness of the piezoelectric element,  $K_{am}$  is the axial stiffness of the magnetic element, with  $M_s$ ,  $M_e$ ,  $M_p$  and  $M_m$  the mass of each of the components. Similarly, for the torsional resonant frequency,

$$\omega_t = f(K_{ts}, K_{te}, K_{tp}, K_{tm}, I_{zs}, I_{ze}, I_{zp}, I_{zm}), \quad (2)$$

where  $\omega_t$  is the fundamental torsional resonant frequency,  $K_{ts}$ ,  $K_{te}$ ,  $K_{tp}$ ,  $K_{tm}$  is the torsional stiffness of each of the components in turn, with  $I_{zs}$ ,  $I_{ze}$ ,  $I_{zp}$  and  $I_{zm}$  as the second moment of inertia in the z-direction of each of the components in turn. The stiffness and inertia parameters of equations (1) and (2) include all the geometric parameters and material properties that fully describe the motor, shown in Figure 1.

To apply the PFM, the system axial and torsional resonant frequencies, as described by equations (1) and (2), are non-dimensionalised using the Buckingham Pi theorem [17]. This gives

$$\omega_a \left( \frac{M_s}{K_{as}} \right)^{0.5} = f \left( \frac{K_{ae}}{K_{as}}, \frac{K_{ap}}{K_{as}}, \frac{K_{am}}{K_{as}}, \frac{M_e}{M_s}, \frac{M_p}{M_s}, \frac{M_m}{M_s} \right) \quad (3)$$

and

$$\omega_t \left( \frac{I_{zs}}{K_{ts}} \right)^{0.5} = f \left( \frac{K_{te}}{K_{ts}}, \frac{K_{tp}}{K_{ts}}, \frac{K_{tm}}{K_{ts}}, \frac{I_{ze}}{I_{zs}}, \frac{I_{zp}}{I_{zs}}, \frac{I_{zm}}{I_{zs}} \right). \quad (4)$$

Henceforth, dimensionless parameters will appear with an asterisk (\*).

Equations (3) and (4) represent the relationship between the system parameters and the axial and torsional resonant frequencies, respectively. Fitting the non-dimensional parameters in these equations against a non-dimensional frequency calculated using FEM will complete the relationship.

The PFM can also be used to determine a relationship between the electro-mechanical resonant frequency and the system parameters. As with the axial and torsional resonant frequencies, the electro-mechanical resonant frequency is a function of all the parameters shown in Figure 1. However, for this analysis we choose not to combine them, conducting the analysis on the full set of parameters.

### 3.2. PFM with Epoxy Bonds

When designing piezoelectric ultrasonic resonant micro-motors at scales measured in millimetres and above, it is standard practice to ignore the effect the epoxy bonds have on the resonant frequencies of the motor. This process is justified by the difference

between the length scales of the epoxy bond (5–20  $\mu\text{m}$ ) and the acoustic wave length of the system (1 mm and above for motors designed to make use of the fundamental and lower harmonic resonances). However, when producing a motor that is on the hundreds of microns scale with three epoxy bonds, such as the one described in this paper, the bonds have a notable effect on the resonant frequencies of interest (see figure S1 in the supplementary material for how the thickness of the epoxy bonds affect the resonant frequencies of interest in this motor). As such, two functions will be generated for the axial, torsional and electro-mechanical resonant frequencies. One will use the standard design methodology, ignoring the epoxy bonds, while a second will include the epoxy bonds. This will allow us to compare the two and understand the differences.

To include the epoxy in this model, we add components to the system to represent the joints. This will produce eight new parameters to be considered in equations (1) and (2);  $K_{ace}$ ,  $M_{ce}$ ,  $K_{ane}$ ,  $M_{ne}$ ,  $K_{tce}$ ,  $I_{zce}$ ,  $K_{tne}$ ,  $I_{zne}$ . These are axial stiffness and mass for the conductive epoxy, axial stiffness and mass for the non-conducting epoxy and the torsional stiffness and second moment of inertia for the same, respectively.

### 3.3. Finite Element Method Model

For this paper, all finite element method models are produced using the commercial software package ANSYS v10.0 (ANSYS Inc., Canonsburg, PA, USA), unless otherwise noted. The model components are constructed using 3D 10-node tetrahedral structural solid elements. The average number of elements for a complete motor prototype is 16500, although this number varies widely due to auto-meshing.

The axial and torsional resonant frequencies of the system under investigation are determined using modal analysis. For this, ANSYS solves an eigenvalue extraction problem of the form

$$[K]\{\Phi\} = \lambda_i[M]\{\Phi\},$$

where  $[K]$  is the structure stiffness matrix,  $\{\Phi\}$  is the eigenvector,  $\lambda_i$  is the eigenvalue and  $[M]$  is the structure mass matrix. The eigenvalues were determined using a shifted block Lanczos algorithm based on the theoretical work of Grimes et al. [18].

The electro-mechanical resonant frequency is approximated by conducting a harmonic analysis of the system at predetermined steps across a frequency range. The frequency that results in the system having a phase of approximately zero for the current reaction force of the piezoelectric element is recorded as the electro-mechanical resonant frequency.

The equations of motion of the system for the harmonic analysis are of the form

$$[M]\{\ddot{u}\} + [C]\{\dot{u}\} + [K]\{u\} = \{F^a\},$$

where  $[M]$  is the structural mass matrix,  $[C]$  is the structural damping matrix,  $[K]$  is the structural stiffness matrix,  $\{\ddot{u}\}$ ,  $\{\dot{u}\}$  and  $\{u\}$  are the nodal acceleration, velocity and displacement vectors, respectively, and  $\{F^a\}$  is the applied load vector. This equation is solved directly by ANSYS using the full system matrices. Damping for the system

was applied as a constant damping value for each material in the system, creating a stiffness matrix multiplier.

The finite element model of the motor is constructed by rigidly bonding the four motor components. The motor model uses free-free boundary conditions as this is the situation for the motor when used in an *in vivo* microbot. The epoxy joints are modelled as additional components, rigidly bonded to the adjacent motor components. Specific mechanical properties of the epoxy bonds are not available, however, the mechanical properties of a closely related epoxy *are* [19]. Specific values for the Young's and shear moduli of the modelled epoxy bonds were approximated by scaling the known values in [19] using the Shore hardness as the scaling factor.

The set of finite element models produced using ANSYS are validated through a comparison of calculated resonant frequencies and those measured from a prototype motor. This is reported in Section 4. The accuracy of the resonant frequency prediction validates the free-free boundary conditions of the finite element model and the damping ratio methodology and values. Moreover, it validates the approximation whereby the mechanical properties of the epoxy bonds were calculated through the scaling of the mechanical properties of a closely related epoxy.

Table 1 defines the parameter design space for all FEM's and subsequently all other models. From experience with fabrication and availability, the stator, electrode, piezoelectric element and magnetic element will be fabricated from 304 stainless steel, beryllium copper, C203 lead zirconate titanate and neodymium iron boron, respectively. As such, the mechanical parameters will remain fixed. To include the epoxy bonds in the analysis, we specify the characteristics of the epoxy bonds:

- the conductive epoxy bonds between the electrode, the piezoelectric element and the magnetic element have the same dimensions as the piezoelectric element;
- the diameter of the epoxy bond between the stator and the electrode is the same as the outside diameter of the stator;
- the thickness of all epoxy bonds are the same;
- the range of epoxy thickness is  $0 < L_e < 22.5 \mu\text{m}$  (for the purposes of our parametric study, we vary  $L_e$  in steps of  $2.5 \mu\text{m}$ );
- the conductive epoxy material is Epotek H20E (Elecsys LLC, Providence, RI, USA);
- the non-conductive epoxy material is Araldite 5min (Shelleys, Padstow, NSW, Australia).

### 3.4. Modelling of Stator

To apply the PFM, we need to know the value for the stiffness and inertia of all components for a set of points in a desired parameter space. Figure 1 shows the simple geometries of the electrode, piezoelectric element and magnetic element, which result in a straightforward calculation of the axial and torsional stiffness, mass, and second moment of inertia of these components. However, the complex non-linear geometry

**Table 1.** Parameter space used for the analysis of the mechanical system throughout the paper.  $N_g$  refers to the number of grooves in the stator,  $E$  is the Young's modulus associated with the component material,  $G$  is the Shear modulus associated with the component material with dimensions defined in Figure 1. Note: The material properties ( $E$  and  $G$ ) are kept constant.

Parameter	Low Value ( $V_l$ )	High Value ( $V_h$ )
Stator		
$D_o$	120 $\mu\text{m}$	360 $\mu\text{m}$
$D_i$	69 $\mu\text{m}$	105 $\mu\text{m}$
$L_s$	460 $\mu\text{m}$	1380 $\mu\text{m}$
$G_w$	9.2 $\mu\text{m}$	23 $\mu\text{m}$
$\alpha$	0.114	1.356
$N_g$	2	4
$G_d$	13.8 $\mu\text{m}$	59.8 $\mu\text{m}$
$E_s$	193 GPa	193 GPa
$G_s$	57.9 GPa	57.9 GPa
Electrode		
$D_e$	200 $\mu\text{m}$	1000 $\mu\text{m}$
$L_e$	10 $\mu\text{m}$	200 $\mu\text{m}$
$E_e$	117 GPa	117 GPa
$G_e$	39.8 GPa	39.8 GPa
Piezoelectric Element		
$B_p$	100 $\mu\text{m}$	500 $\mu\text{m}$
$W_p$	100 $\mu\text{m}$	500 $\mu\text{m}$
$L_p$	100 $\mu\text{m}$	1000 $\mu\text{m}$
$E_p$	60 GPa	60 GPa
$G_p$	17.4 GPa	17.4 GPa
Magnetic Element		
$D_m$	200 $\mu\text{m}$	1000 $\mu\text{m}$
$L_m$	100 $\mu\text{m}$	1000 $\mu\text{m}$
$E_e$	160 GPa	160 GPa
$G_e$	38.4 GPa	38.4 GPa

of the stator makes an analytical derivation of these parameters for this component difficult. To determine these parameters for the stator, we will use the PSM as outlined in [13].

*Piezoelectric motor for a micro-robotic applications*

9

From geometry, we determine the function for stator mass to be

$$M_s = \rho_s \left( L_s \frac{\pi}{4} (D_o^2 - D_i^2) - N_g G_w G_d \left( \frac{G_1}{\sin \alpha} \right) \right), \quad (5)$$

where  $G_1$  is the non-dimensional axial length of the groove and is defined as  $G_1 = 0.9L_s$ . From the PSM, the function for the second moment of inertia of the stator is

$$I_{zs} = \rho_s L_s \frac{\pi}{32} (D_o^4 - D_i^4) - 2L_s \rho_s N_g \sin^{-1} \left( \frac{G_w}{\sin \alpha} \right) \left( \frac{D_o^4}{64} - \frac{1}{4} \left( \frac{D_o^4}{2} - G_d \right)^4 \right). \quad (6)$$

Completing the method results in a function for the non-dimensional pseudo-axial stator stiffness:

$$K_{as}^* = 2(G_d^{*0.85}) \left( \cos \left( \frac{A\pi}{2} \right) e^{-2.2\alpha} + \sin \left( \frac{A\pi}{2} \right) \cos(\alpha)^{2.2} \right) \cdot (N_g^{0.013G_d^{*-1.5}}) (G_w^{*(-0.155 \ln(G_d^*)-0.13)}) (L_s^{*-1}), \quad (7)$$

where  $A$  is the ratio of groove depth to wall thickness  $A = 2G_d^*/(1 - D_i^*)$ . Similarly, the non-dimensional torsional pseudo-stiffness is:

$$K_{ts}^* = 0.245(G_d^{*1.1}) (G_w^{*-0.275 \ln(G_d^*)-0.35}) (N_g^{0.023G_d^{*-1.35}}) (L_s^{*-1})(\alpha^{3G_d^{*-1}}). \quad (8)$$

Equations (7) and (8) represent a simple power law for each non-dimensional parameter, with the power varying according to the depth of the groove. These functions can be used to collapse the data as shown in figure 2, where a linear least-squares fit results in  $y = 0.99x$  with a coefficient of determination of  $R^2 = 0.98$  for the axial stiffness, and  $y = x$  with a coefficient of determination of  $R^2 = 0.98$  for the torsional stiffness. These correlations demonstrate good agreement with the stiffness calculated using the finite element method as part of the PSM.

*3.5. Axial and Torsional Resonant Frequencies*

Having determined functions for all the parameters in equations (3) and (4), we can now apply the PFM to determine the relationship. For the fundamental axial resonant frequency, this results in:

$$\omega_a^* = 0.0474 (K_{ae}^*)^{0.42} (K_{ap}^*)^{-0.1} (K_{am}^*)^{0.1} \cdot (M_e^*)^{0.38} (M_p^*)^{-0.5} (M_m^*)^{-0.1}, \quad (9)$$

and for the fundamental harmonic torsional frequency:

$$\omega_t^* = 0.0232 (K_{te}^*)^{0.45} (K_{tp}^*)^{0.1} (K_{tm}^*)^{0.1} \cdot (I_{ze}^*)^{0.35} (I_{zp}^*)^{-0.5} (I_{zm}^*)^{-0.1}. \quad (10)$$

In a simple system the higher harmonics would be multiples of the functions described in equations (9) and (10). For this complex, non-linear system this is not the

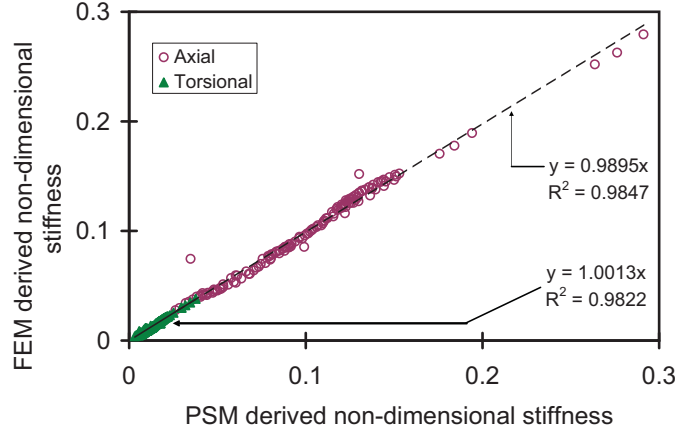


**Figure 2.** Collapse of the axial pseudo-stiffness and torsional pseudo-stiffness data, using equations (7) and (8), respectively. This shows good agreement with the stiffness calculated from the finite element method model as part of the PSM, thus validating our pseudo-stiffness model against the finite element method model.

case. The second and higher harmonics are affected by the geometry of the system and the coupling between the axial and torsional modes. Subsequently, a best fit approach was taken to derive a function for the second axial and torsional harmonic frequencies. This resulted in

$$\omega_{2a}^* = 1.5\omega_a^{*0.76}, \quad (11)$$

and

$$\omega_{2t}^* = \omega_t^{*0.56}, \quad (12)$$

where the subscript 2 refers to the second harmonic, and  $\omega_a^*$  and  $\omega_t^*$  can be found from equations (9) and (10), respectively.

Equations (9)–(12) can be used to collapse the data, as shown in figure 3. In general, this collapse demonstrates good agreement with the axial and torsional resonant frequencies calculated using the finite element method. We note that the collapse of the fundamental harmonic for both the axial and torsional modes is excellent, while the collapse for the second harmonic demonstrates some spread at high and low frequencies. This spread arises from the best fit outlined in equations (11) and (12), which work best for the bulk of the mid-range (design) frequencies. If it was beneficial for the motor to be designed with a high or low frequency, it would be necessary to change the approximations in equations (11) and (12) to allow for this. To more accurately model high frequencies, the exponent would need to be made smaller, with a larger exponent resulting in the more accurate modelling of lower frequencies.



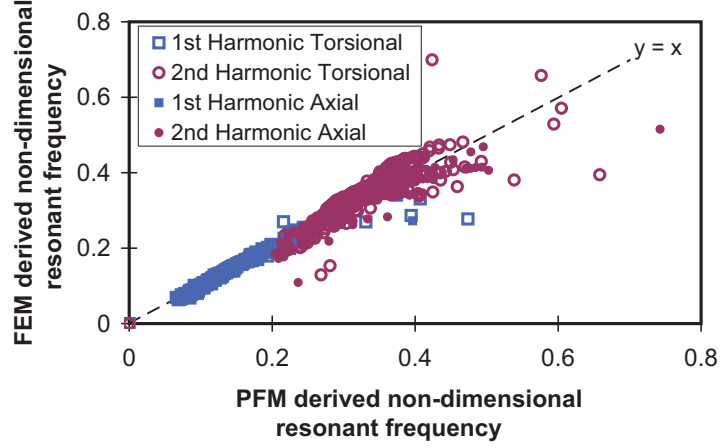


**Figure 3.** Collapse of the non-dimensional axial resonant and torsional resonant frequencies using equations (9)–(12) and those calculated using the FEM. The collapse shows good agreement, validating our model within the bounds of the FEM.

Applying the PFM with the additional parameters necessary to model the epoxy bonds, we obtain the following fundamental axial non-dimensional resonant frequency:

$$\begin{aligned} \omega_{aep}^* &= 0.0232 (K_{ae}^*)^{0.42} (K_{ap}^*)^{-0.1} (K_{am}^*)^{0.1} \cdot \\ &\quad (M_e^*)^{0.38} (M_p^*)^{-0.5} (M_m^*)^{-0.1} (K_{ace}^*)^{0.054} \cdot \\ &\quad (M_{ce}^*)^{-0.054} (K_{ane}^*)^{0.027} (M_{ne}^*)^{-0.027}, \end{aligned} \quad (13)$$

and the fundamental non-dimensional torsional frequency:

$$\begin{aligned} \omega_{tep}^* &= 0.0082 (K_{te}^*)^{0.45} (K_{tp}^*)^{-0.1} (K_{tm}^*)^{0.1} \cdot \\ &\quad (I_{ze}^*)^{0.35} (I_{zp}^*)^{-0.5} (I_{zm}^*)^{-0.1} (K_{tce}^*)^{0.061} \cdot \\ &\quad (I_{zce}^*)^{-0.061} (K_{tne}^*)^{0.031} (I_{zne}^*)^{-0.031}. \end{aligned} \quad (14)$$

As in the system without epoxy, a best fit approach was used to derive a relationship for the second axial and torsional harmonic frequencies:

$$\omega_{2aep}^* = 1.44 \omega_{aep}^{*0.86}, \quad (15)$$

and

$$\omega_{2tep}^* = 2.05 \omega_{tep}^*, \quad (16)$$

where  $\omega_{aep}^*$  and  $\omega_{tep}^*$  can be obtained from equations (13) and (14), respectively. These equations can be used to collapse the data as shown in figure 4, which shows good agreement with the frequency calculated using the finite element method.

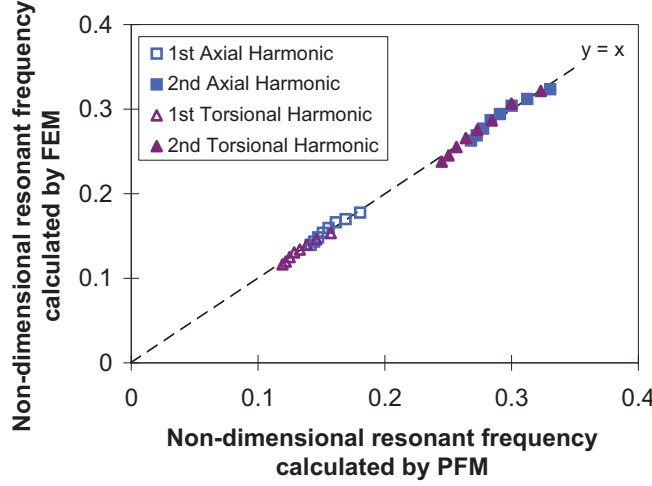


**Figure 4.** Collapse of the non-dimensional axial and torsional resonant frequencies using equations (13)–(16), showing good agreement with the frequency calculated from the finite element method

### 3.6. Sensitivity Analysis

Equations (9)–(12) use all the system parameters outlined in figure 1 to calculate the axial and torsional resonances. To reduce the number of parameters necessary to investigate a final design, the importance of each of these parameters in achieving matched axial and torsional resonances is examined. This is achieved by plotting the change in the ratio of the fundamental axial frequency to the second harmonic torsional resonant frequency due to geometric changes. We choose to examine the fundamental axial and second torsional resonances as these frequencies will match at a higher frequency than the two fundamental modes, and thus, are more likely to also be matched to the electro-mechanical resonance.

Figure 5 demonstrates how the frequency ratio is affected by changes to the system parameters, from which we note that the effect of  $G_w$ ,  $N_g$ ,  $D_i$ ,  $L_e$  and  $D_m$  is negligible. From equations (9) and (10) we note that the exponent of the non-dimensional stiffness groups that include the magnetic element parameters ( $K_{am}^*$ ,  $K_{tm}^*$ ) are the same and are the inverse of the exponent of the inertia groups that also include the magnetic element parameters ( $M_m^*$ ,  $I_{zm}^*$ ). This results in a cancelling of  $D_m$  within equations (9) and (10) leading to what we see in figure 5(d) with  $D_m$  having no effect. Similarly, the exponents of the non-dimensional groups that include the electrode parameters are close, but inverted, which results in  $L_e$  having a very small exponent demonstrated by the result in figure 5(c). Physically, this suggests that the location of the components strongly affects whether a parameter is important in the matching of the axial and torsional resonant frequencies.

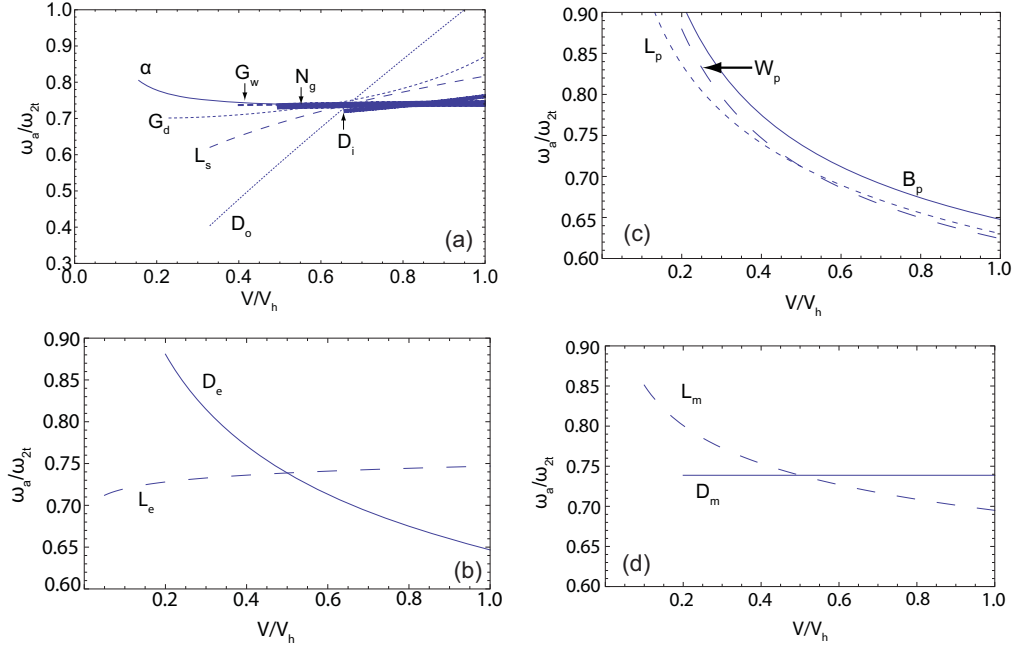


**Figure 5.** Sensitivity of the ratio of fundamental axial resonant frequency,  $\omega_a$  and the second harmonic torsional resonant frequency,  $\omega_{2t}$  to changes in the system's geometric parameters associated with (a) the stator (b) the electrode, (c) the piezoelectric element and (d) the magnetic element.  $V/V_h$  refers to the change in the value of the parameter between the high and low values in table 1 normalised by the high value  $V_h$ . These charts are used to determine which parameters are important in matching  $\omega_a$  and  $\omega_{2t}$ .

We also note that all of the non-dimensional groups in equations (9) and (10) are affected by the stator parameters. Holding all other component parameters constant, we can determine a function for how the ratio  $\omega_a/\omega_{2t}$  scales with the stator stiffness and inertia;

$$\frac{\omega_a}{\omega_{2t}} \propto \left( \frac{K_{as}^{0.08}}{K_{ts}^{0.084}} \right) \left( \frac{I_{zs}^{0.14}}{M_s^{0.28}} \right) = SI,$$

where  $S$  is the stiffness ratio and  $I$  is the inertia ratio. This demonstrates that the ratio of mass to second moment of inertia of the stator has a much larger effect on whether the frequencies can be matched than the relative stiffness.

We will fix the values of the parameters that have little effect on the frequency ratio:  $G_w$ ,  $N_g$ ,  $D_i$ ,  $L_e$  and  $D_m$  will be fixed at  $13.8 \mu\text{m}$ ,  $2$ ,  $106 \mu\text{m}$ ,  $15 \mu\text{m}$  and  $400 \mu\text{m}$ , respectively, based on availability and ease of manufacturing. Further, the availability of small scale stainless steel tubing will fix  $D_o$  at  $241 \mu\text{m}$ ,  $D_e$  will always be equal to the largest diameter of the motor to ensure practical use, and the commercial availability

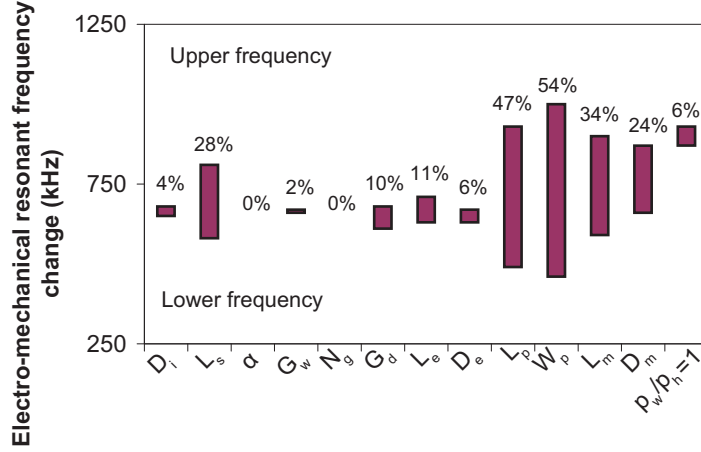


**Figure 6.** The change in electro-mechanical resonance for the parameter range defined in table 1. From this, we can determine which parameters are important for calculating the electro-mechanical resonant frequency.

of the piezoelectric element will fix  $B_p$ ,  $W_p$  and  $L_p$  at  $250 \mu\text{m}$ ,  $250 \mu\text{m}$ , and  $500 \mu\text{m}$ , respectively. This results in  $G_d$ ,  $L_s$ ,  $\alpha$  and  $L_m$  being the parameters of interest when finalising the prototype motor design.

### 3.7. Electro-Mechanical Resonant Frequency

To determine the relationship that describes how the electro-mechanical resonance of the system responds to changes in the geometric parameters, we begin by conducting a sensitivity analysis to determine which of the parameters are of importance. Similar to the process undertaken in Section 3.6, the sensitivity of the electro-mechanical resonant frequency to changes in the parameters is demonstrated by plotting the change in electro-mechanical resonant frequency for the range of a parameter outlined in table 1. However, the analysis is conducted based on the FEM rather than a model using the PFM, the results for which are shown in figure 6.

Figure 6 shows that the majority of the parameters have little effect on the electro-mechanical resonance, with the change in frequency being approximately 10% or less across the whole parameter range. We note that the majority of those with a change greater than 10%, and therefore of most importance, are the component lengths, as expected for an axially poled piezoelectric element. We also note that changes in the width of the piezoelectric element  $W_p$  (and therefore the breadth of the element  $B_p$  due to the rectangular cross-section) have a large effect on the electro-mechanical resonance. However, if the aspect ratio is kept constant at one ( $W_p/B_p = 1$ ), the effect of changes to  $W_p$  and  $B_p$  cancel each other, resulting in the ratio  $W_p/B_p = 1$  having little effect. Due to the axial poling of the piezoelectric element, we would expect the diameters

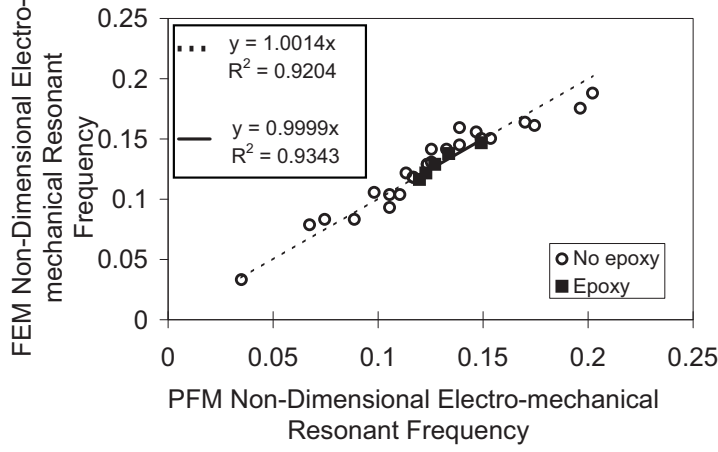


**Figure 7.** Comparison of the electro-mechanical resonant frequency as calculated using the FEM and equations (17) and (18) for the parameter space outlined in table 1.

of the magnetic element and electrode to have less effect than the component lengths, which is the case. We surmise that the larger effect of the magnetic element diameter, when compared with the geometrically similar electrode, is the overall volume of the component, as can be seen by the difference in  $L_e$  and  $L_m$  in table 1.

From figure 6 we note that only  $L_s$ ,  $L_p$ ,  $L_m$ ,  $D_m$  and  $W_p$  have a significant effect on the electro-mechanical resonant frequency. However, we will limit our analysis to a function that meets the requirement  $W_p/B_p = 1$ , allowing us to omit  $W_p$  from the analysis. This will reduce the available design geometries to a square cross-section, which is acceptable as it works well with the circular cross-section of the other components.

Using these parameters and the constant material properties, we can write a function for the electro-mechanical resonance:

$$\Omega^* = f(L_{sp}^*, L_{mp}^*, D_{mp}^*, E_{sp}^*, \rho_{sp}^*, E_{mp}^*, \rho_{mp}^*),$$

where the subscript p refers to a non-dimensionalisation by the piezoelectric element component parameters. Applying the PFM, and using constant values of  $E_{sp}^*$ ,  $\rho_{sp}^*$ ,  $E_{mp}^*$  and  $\rho_{mp}^*$ , yields the following relationship for the electro-mechanical resonance:

$$\Omega^* = 0.136(L_{sp}^* L_{mp}^* D_{mp}^*)^{\frac{1}{4}}. \quad (17)$$

Figure 7 demonstrates how well the model predicts the electro-mechanical resonance of the system by plotting the results from equation (17) against the FEM derived non-dimensional electro-mechanical resonant frequency. We see there is a good agreement with a coefficient of determination of  $R^2 = 0.92$ .

This model can be modified to include the epoxy bonds in the same way as the model for the axial and torsional resonant frequencies. Doing so, we find the following

function:

$$\Omega_{\text{ep}}^* = 0.0787(L_{\text{sp}}^* L_{\text{mp}}^* D_{\text{mp}}^*)^{\frac{1}{4}} (L_{\text{ep}}^*)^{-\frac{1}{10}}, \quad (18)$$

where  $\Omega_{\text{ep}}^*$  is the non-dimensional electro-mechanical resonant frequency of the prototype motor including the epoxy bonds. Figure 7 also demonstrates the correlation between the PFM derived resonant frequency and the FEM derived resonant frequency with the inclusion of epoxy. The limited number of data points arises due to the analysis only having to be conducted on the epoxy bond thickness.

### 3.8. Matching of Resonant Frequencies

Having demonstrated that equations (9)–(12) successfully model the first and second harmonics of the non-dimensional axial and torsional resonant frequencies, and that equation (17) models the electro-mechanical resonance, we examine the effect that changes to the system parameters have on these frequencies and the parametric relationships required to achieve matched axial, torsional and electro-mechanical resonant frequencies.

For the system frequencies of interest to be matched, we must have

$$\omega_a = \omega_{2t} = \Omega \Rightarrow \frac{\omega_a}{\omega_{2t}} = \frac{\omega_a}{\Omega} = \frac{\omega_{2t}}{\Omega}, \quad (19)$$

where  $\omega_a/\omega_{2t} = 1$ ,  $\omega_a/\Omega = 1$  and  $\omega_{2t}/\Omega = 1$ . From the sensitivity analysis (Section 3.6), only  $L_s$ ,  $G_d$ ,  $\alpha$  and  $L_m$  have a significant effect as to whether the fundamental axial and second torsional resonant frequencies can be matched ( $\omega_a/\omega_{2t} = 1$ ). By applying these same constraints to the model for the electro-mechanical resonance as defined by equation (17), we can plot the relationships in equation (19) and determine the design space for the parameters of interest to ensure the three resonances are matched. A 3-D contour plot demonstrating this is shown in figure 8. Each of the planes represents the changes in parameter relationship required to ensure either  $\omega_a/\omega_{2t} = 1$ ,  $\omega_a/\Omega = 1$  or  $\omega_{2t}/\Omega = 1$  is achieved. Holes in the planes represent where a ratio of one could not be achieved.

In figure 8 we see the three planes intersect along a line, which represents the design space of the motor to ensure we have matched axial, torsional and electro-mechanical resonances. When the magnetic element is short, as shown in figure 8(c), we can see that the design space is small. This increases as the magnetic element length increases (8(b), then 8(a)). This characteristic is driven by the importance of the magnetic element length in the ratios  $\omega_a/\omega_{2t}$ ,  $\omega_a/\Omega$  and  $\omega_{2t}/\Omega$ . Examining these ratios we find that  $\omega_a/\omega_{2t} \propto 1/L_m^{0.88}$ ,  $\omega_a/\Omega \propto 1/L_m^{0.45}$  and  $\omega_{2t}/\Omega \propto 1/L_m^{0.362}$ , demonstrating that the magnetic length of the element has a large effect on achieving equations (19). In general, a prototype with a small design envelope is difficult to fabricate, as it allows little room for manufacturing tolerances. For a larger magnetic element length, the design space incorporates a large range of stator lengths and groove depths. Given that a longer magnetic element is beneficial for the design space, in addition to being beneficial in terms of preload, we choose to use the full available magnet length of 950  $\mu\text{m}$  in the

*Piezoelectric motor for a micro-robotic applications*

17

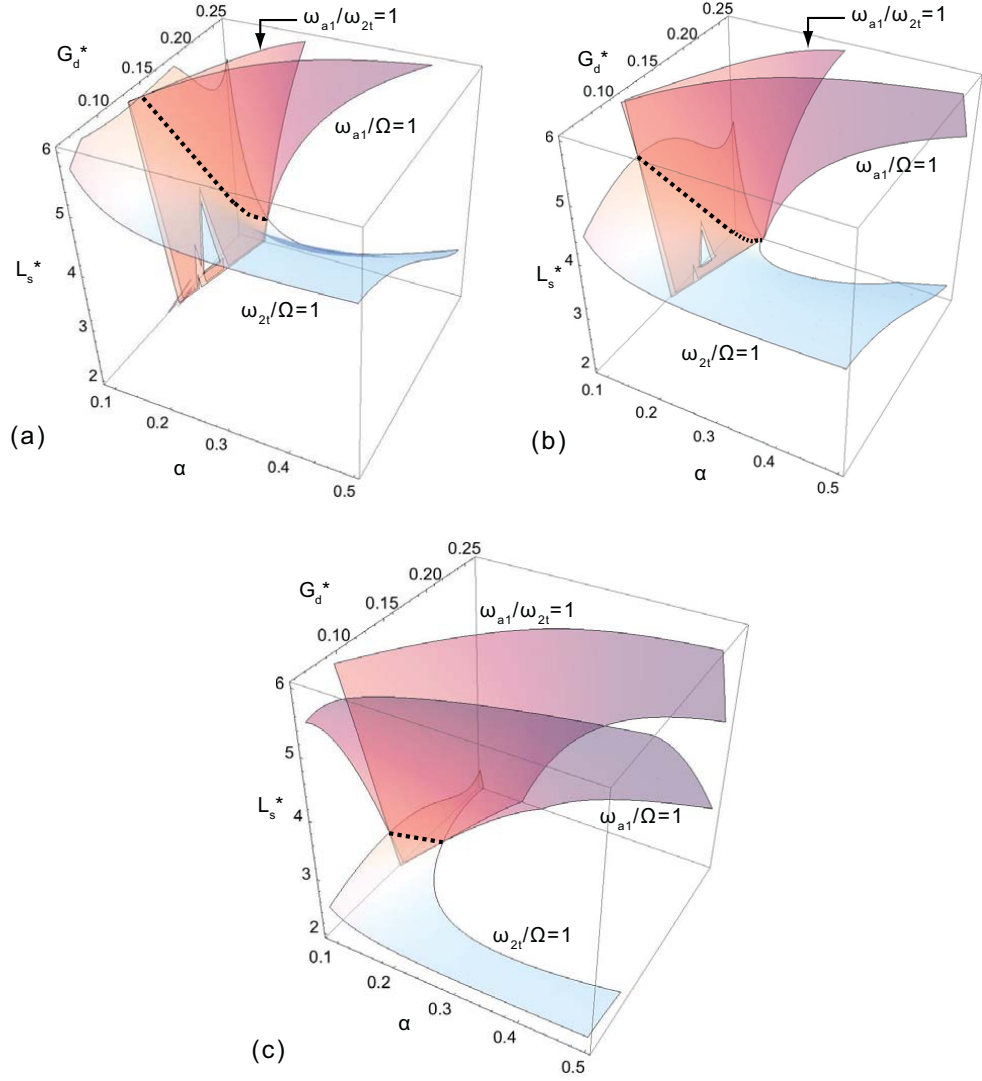


**Figure 8.** 3-D contour plots showing how the relationship between the parameters of importance need to change to ensure unity frequency ratios are achieved for a magnetic element length of (a) 950  $\mu\text{m}$ , (b) 550  $\mu\text{m}$ , and (c) 150  $\mu\text{m}$ . The dashed line represents the design space where the system resonant frequencies of interest are matched; equation (19).

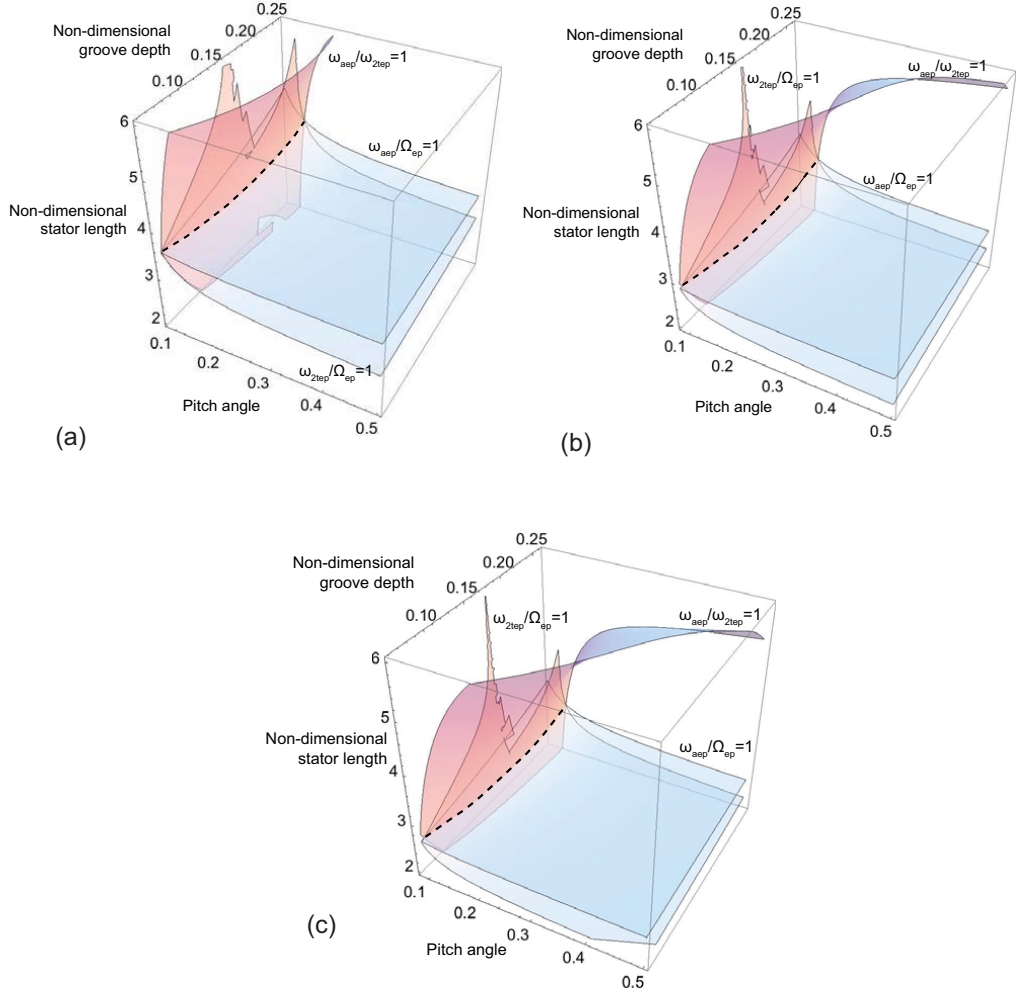


**Figure 9.** The addition of the epoxy bonds to the model changes the design space from figure 8(a) to the above for an epoxy thickness of (a)  $2.5 \mu\text{m}$ , (b)  $12.5 \mu\text{m}$  and (c)  $22.5 \mu\text{m}$ .

motor design. It is noteworthy that for all cases a small pitch angle is required. This results from the pitch angle having little effect on the electro-mechanical resonance, but being important in the matching of axial and torsional resonant frequencies.

Repeating this process for equations (13)–(16) we can identify the design space of the motor including epoxy bonds. As an outcome of the results in figure 8, the magnetic element length will be fixed at  $950 \mu\text{m}$ . Using the remaining three parameters and the thickness of the epoxy, we can visualise the design space of the motor; figure 9.

What we see is that to ensure matched resonances, the stator length is reduced to



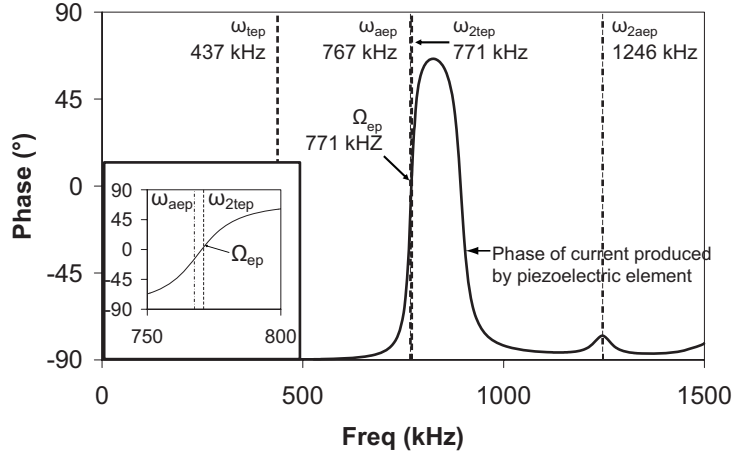


**Figure 10.** Modelling the final prototype design using the FEM demonstrates how closely matched the resonant frequencies of interest are, with the fundamental axial resonant frequency  $\omega_{aep}$ , second harmonic torsional resonant frequency  $\omega_{2tep}$  and electro-mechanical resonance frequency  $\Omega_{ep}$  all within 0.5%.

compensate for the increase in thickness of the epoxy. This results in the pitch angle and groove depth also requiring a change. Comparing the solution space in figure 8(a) with that produced in figure 9 we note that the introduction of the epoxy to the model has a significant effect. Effectively, the epoxy acts as a damper for the other parameters reducing the effect that each of the original parameters has on the system, which intuitively is easy to understand.

From the developed model, we can design a prototype motor that closely matches the axial, torsional and electro-mechanical resonant frequencies. Using the fixed material properties and the geometric parameters fixed by the work in Sections 3.6 and 3.7, this results in  $L_m=950 \mu\text{m}$ ,  $G_d=47 \mu\text{m}$ ,  $L_s=529 \mu\text{m}$   $\alpha=0.119$  radians and  $L_e=15 \mu\text{m}$ . Modelling the design using the FEM demonstrates how well the three resonances are matched, as shown in figure 10. Details on the fabrication and assembly of the motor are reported in Appendix A, with details on the motor mounting in Appendix B.

#### 4. FEM Validation

Figures 4 and 7 demonstrate that the three resonant frequencies of interest calculated using the PFM correlate well with those calculated using the FEM. To validate the FEM, and thus the PFM, we compare the fundamental and second harmonic axial resonant frequencies with epoxy  $\omega_{aep}$  and  $\omega_{2aep}$ , the fundamental and second torsional resonant frequencies with epoxy  $\omega_{tep}$  and  $\omega_{2tep}$ , and the electro-mechanical resonant frequency with epoxy  $\Omega_{ep}$  calculated with the FEM, with those experimentally measured using the prototype with parameters outlined in Section 3.8.

The mechanical resonant frequencies are determined using the method outlined by Friend et al. [20]. This method uses a Laser Doppler Vibrometer (LDV) (MSA-400, Polytec GmbH, Waldbronn, Germany) to record the out-of-plane displacement spectra for six points on the stator-tip, which return the spectra and subsequently the resonant frequencies as shown in figure 11. When necessary, the resonant frequencies were confirmed visually using the scanning function of the LDV. Comparing these with the resonant frequencies from the FEM, figure 11(a), we can see that the fundamental torsional and second axial resonant frequencies compare well with an error of approximately 0.5% and 1%, respectively. The fundamental axial frequency is acceptable with an error of approximately 5%; however, the second harmonic torsional shows an error of nearly 20%. This error comes from the difficulties in fabricating a stator with a known depth of groove, which is covered in Appendix A. If we reexamine the frequencies predicted by the FEM, but with an arbitrary groove depth of two-thirds of the original ( $G_d = 31 \mu\text{m}$ ). This is shown in figure 11(b), where we find the results improve to an average error of approximately 3%.

For the electro-mechanical resonance, we compare the resonant frequency calculated with the FEM and the resonant frequency of the fabricated prototype determined using an impedance analyser (Agilent 4294A, Agilent Technologies Australia Pty Ltd, Melbourne, Australia). The results in figure 12 demonstrate that the FEM accurately models the electro-mechanical resonance of the system, with an error of less than 1%. Figure 6 shows that the stator groove depth has little effect on the electro-mechanical resonance of the motor, and as such, a reduction in groove depth of the fabricated stator does not effect the electro-mechanical resonant frequency as it does for the mechanical resonances.

These results demonstrate that the FEM accurately models the axial, torsional and electro-mechanical resonance frequencies of our motor. From this we conclude that the FEM is validated against the prototype, and that the PFM is validated to within the accuracy afforded by the FEM comparison. Moreover, these results also inspire confidence in the scaling used to determine the mechanical properties of the epoxy bonds for the FEM and the damping ratios applied in the model.

## 5. Motor Performance

### 5.1. Experimental Method

To carry out performance measurements, the motor was positioned on a mounting that provided an electrical contact to the base of the magnetic element and the electrode of the motor. A detailed discussion of the mounting design is provided in Appendix B. As can be seen in figure 13(a), a laser beam was positioned to back-light the rotor, which was captured by a high-speed digital camera, figure 13(b) (Olympus iSpeed, Olympus Australia, Mount Waverley, Australia). Using a set-up that provided back lighting was found to improve motion tracking. The rotor was fabricated from a  $250 \mu\text{m}$  diameter

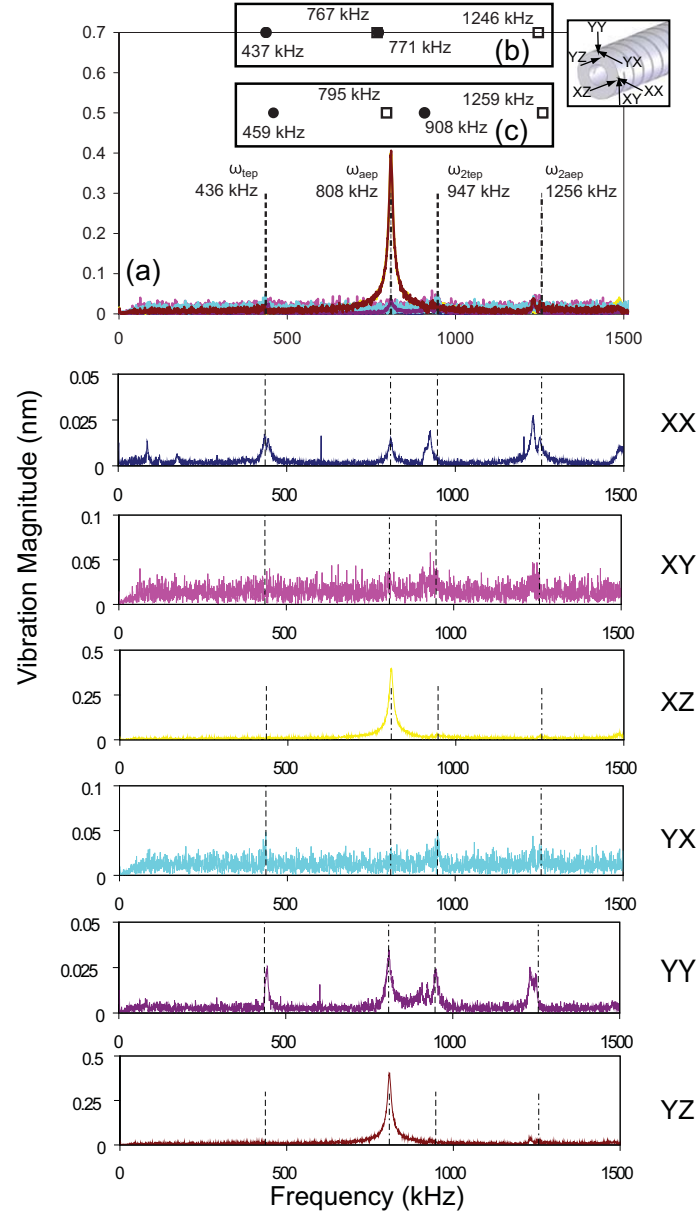


**Figure 11.** A comparison of resonant frequencies. (a) shows resonant frequencies measured using the vibration spectra for the fabricated prototype motor. (b) shows the FEM calculated resonant frequencies for a motor with the parameters outlined in Section 3.8 and (c) shows the FEM calculated resonant frequencies for a motor with a groove depth two-thirds of the original ( $G_d=31 \mu\text{m}$ ). Note: individual measured vibration spectra are shown for clarity in the plots XX–YZ.

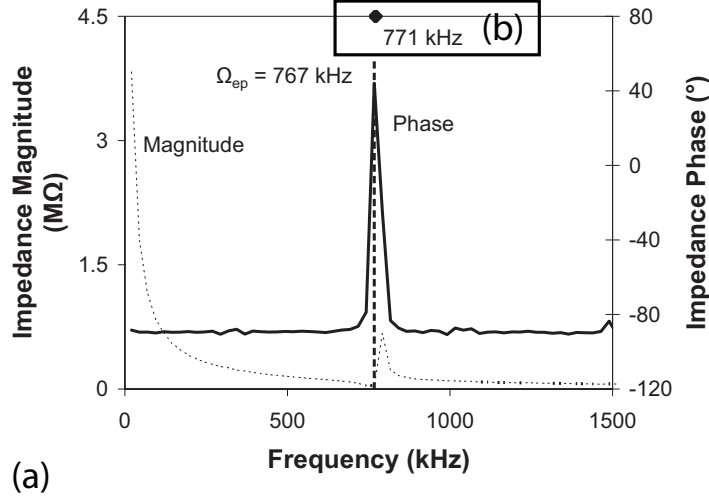


**Figure 12.** Comparison of electro-mechanical resonant frequencies. We see a close correlation between the (a) measured frequency and (b) the FEM derived frequency.

stainless steel ball and a 400  $\mu\text{m}$  diameter beryllium copper disk, with segments removed to allow for motion tracking.

The preload for the motor as designed (figure 13(c)) was  $F_p = 46.6 \mu\text{N}$ , as calculated using a finite element modelling package (COMSOL v3.3a, Technic Pty. Ltd., Hobart, Australia). Details of the model and verification are described in Appendix C. To increase the preload on the rotor, two magnets were added to the system. The first was a neodymium iron boron magnet, 0.5 mm in length and 0.4 mm in diameter, assembled as part of the rotor. The second, also a neodymium iron boron magnet, had dimensions of 10 mm x 10 mm x 2 mm and was placed under the motor mounting. This is shown in figure 13(e). By varying the position of the large magnet relative to the mounting base, we can vary the increased preload  $F_p$  in the system from 341  $\mu\text{N}$  to 2264  $\mu\text{N}$  and 3015  $\mu\text{N}$ . This is an increase of 7, 49 and 65 times the original preload of 46.6  $\mu\text{N}$ , respectively.

To measure the performance, the transient start-up response of the motor was recorded by the high-speed camera at 2000 or 4000 frames-per-second. The angular velocity as a function of time was then determined by tracking the rotor motion using the Olympus iSpeed image processing software (v1.16, Olympus Industrial America, Orangeburg, NY, USA).

### 5.2. Performance

The motor was found to operate most consistently at a frequency of 924 kHz. We believe this occurs as it is the frequency that coincidentally couples the fundamental harmonic axial mode (808 kHz) and the second harmonic torsional mode (947 kHz) to produce an

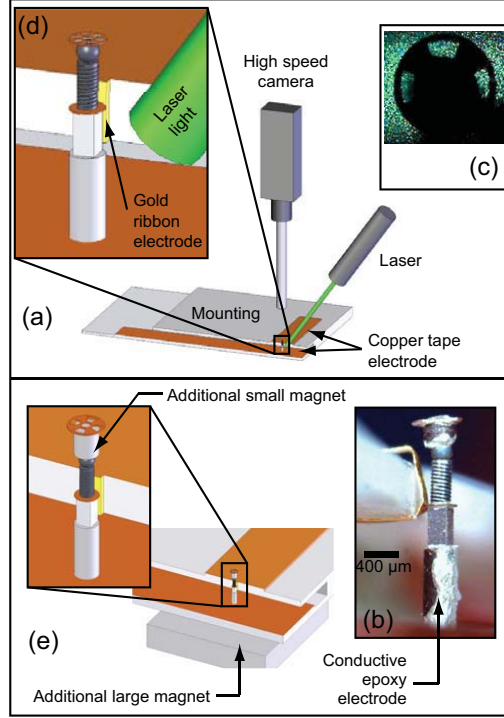


**Figure 13.** (a) The prototype motor was positioned on a mounting facilitating an electrical contact with the conductive epoxy electrode (b) and the base of the magnetic element and the electrode. A 532 nm wavelength laser was positioned to enable the beam to generate back-lighting, resulting in (c) the rotor being recorded as a shadow. The designed motor (d) used a single sphere and the integral magnet to generate preload. Two additional magnets were added to the experimental set up (e) to increase the motor preload. Varying the distance between the large magnet and the mounting changes the preload on the motor.

elliptical stator tip motion. Unfortunately, due to the scale of the rotor, the positioning of the rotor, and the need for it to be magnetic, it is impossible to accurately measure the stator tip motion with the rotor in place.

Using a signal generator and amplifier (Rhode & Schwarz-SML 01 and NF-HSA 4501, North Ryde, NSW, Australia), a voltage  $V_{in}$  of 85 V<sub>p-p</sub> at 924 kHz was applied to the mounting, as measured with an oscilloscope (LeCroy WaveJet 334, Chestnut Ridge, NY, USA). To measure the transient start-up of the motor, the voltage was applied as a step input, resulting in the angular velocity–time curve shown in figure 14.

The motor performance was determined using the method derived by Nakamura et al. [21]. For this, a curve of the form

$$\Omega = \Omega_o \left( 1 - \exp \left( -\frac{t}{\tau_r} \right) \right) \quad (20)$$

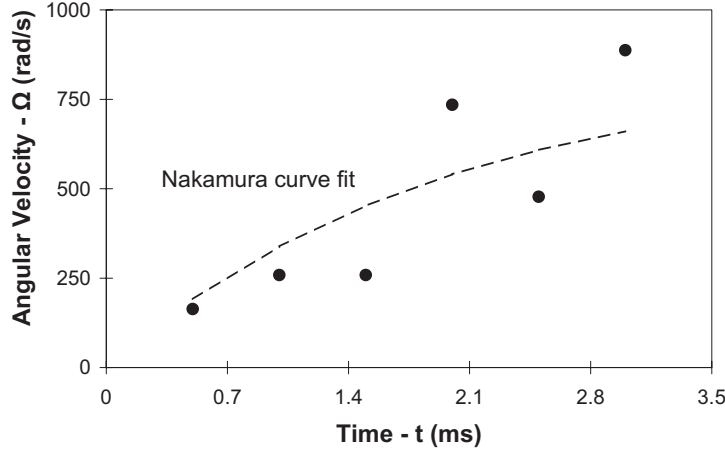


**Figure 14.** The transient start-up speed as a function of time recorded using the high-speed camera at an input voltage of 85 V<sub>p-p</sub> and a frequency of 924 kHz. The motor performance is calculated using the “Nakamura curve fit” [21].

was fitted to the measured data, where  $\Omega$  is the angular velocity,  $\Omega_o$  is the maximum angular velocity,  $t$  is the time and  $\tau_r$  is the rise time. Subsequent frames of the high speed camera recording then revealed a maximum velocity of 838 rad/s. Using a least squares fit for equation (20), a rise time of 1.93 ms was calculated. We thus calculate the start-up torque of the motor  $T$  to be 1.2 nNm, with a maximum output power  $P_o$  of 0.25  $\mu$ W.

Using the cross-sectional area of the rotor sphere as the normalising area of the performance, produces a start-up torque  $T_n$  of 23.8 nNm/mm<sup>2</sup> and power  $P_{no}$  of 5  $\mu$ W/mm<sup>2</sup>. Comparing this with our desired design values of 15 nNm/mm<sup>2</sup> and 65  $\mu$ W/mm<sup>2</sup> from Section 1 we see that our design has met the torque requirement, but only makes 7.5% of the power requirement.

Increasing the preload resulted in an increase in performance. A typical performance curve for the increased preload is shown in figure 15. We can see the measured data has large errors, which results from difficulties with manually tracking the rotor. The randomised repeated runs carried out will ensure the calculated performance is a good approximation of the true motor performance. A periodic variation in the angular velocity of the rotor was also noted. The periodic variation stems in part from a small eccentricity in the positioning of the beryllium copper disk in the rotor relative to the centre line of the motor. It may also be an indication of the bouncing stator-rotor interaction described in [22]. To determine the relative effect of each, it would be necessary to develop a method of measuring the stator and rotor motion simultaneously. To do this would require a transparent rotor that still provided enough preload for operation.

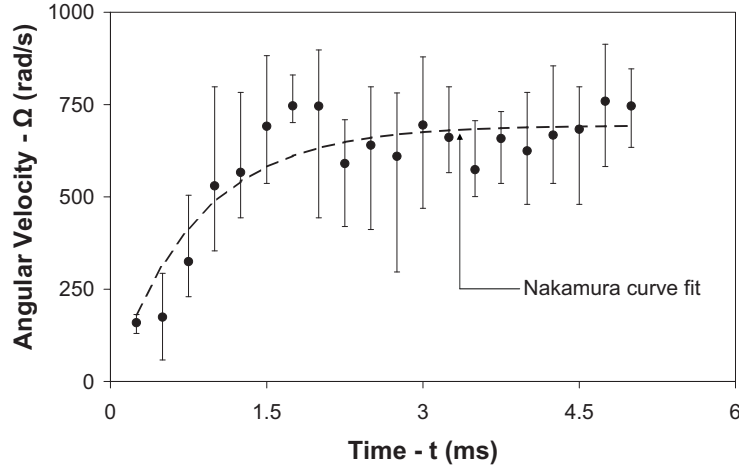


**Figure 15.** The angular velocity with respect to time curve for the motor with a preload of  $2264 \mu\text{N}$  and an input voltage of  $76.5 V_{p-p}$ . This is a typical result for all motor cases with increased preload.

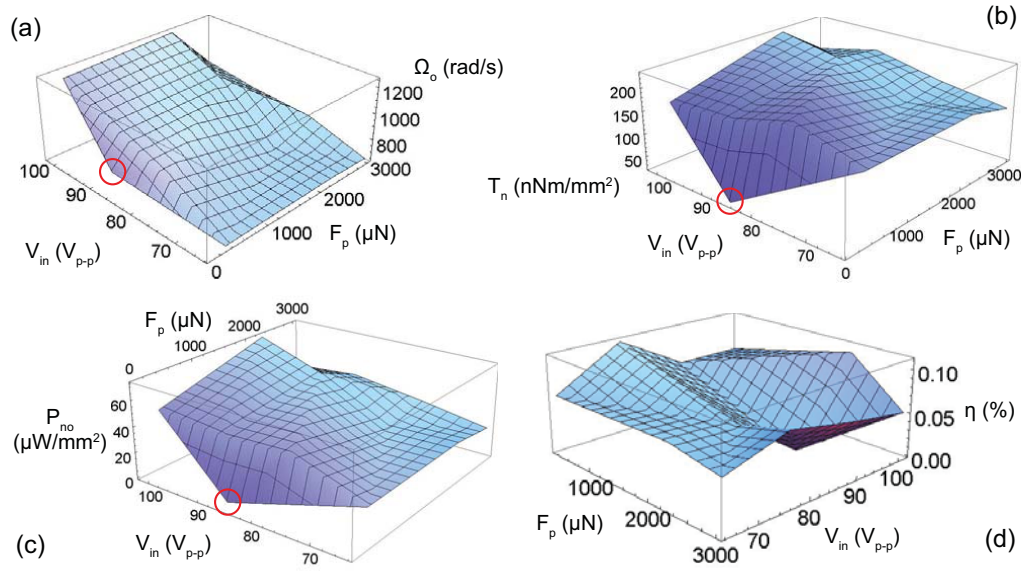


**Figure 16.** (a) The maximum angular rotor velocity  $\Omega_o$  for the full range of motor preloads  $F_p$  and input voltages  $V_{in}$ , (b) the start-up torque normalised by the area of the magnetic element in the rotor  $T_n$ , (c) the normalised motor output power  $P_{no}$  and (d) the motor efficiency  $\eta$ . The circled data point refers to the original motor performance from Section 5.2

Figure 16 parts (a), (b), (c) and (d) show the results for the maximum angular velocity, start-up torque, output power and motor efficiency, respectively, for the entire range of tested preloads and input voltages. Figure 16(a), shows that changes to the preload have little effect on the maximum angular velocity achieved by the motor, as highlighted by the comparable performance of the low preload motor and indicated by the circled data point in figure 16(a). In addition, we see that there is an almost linear relationship between the input voltage and the maximum angular velocity of the motor, which has been found for other piezoelectric ultrasonic micro-motor designs [23, 24].

For the start-up torque, figure 16(b), we see that both the preload and the input voltage have an effect. The maximum start-up torque is found for a combination of a preload of  $2264 \mu\text{N}$  and an input voltage of  $101.6 V_{p-p}$ , where the normalised torque is  $230.4 \text{ nNm/mm}^2$ . This results is normalised by the cross-sectional area of the small magnet, which is 2.5-times larger than the cross-sectional area of the sphere used to normalise the results for the as-designed motor. We note that, in general, the measured torque increases as the preload is increased from  $46.6 \mu\text{N}$  to  $2264 \mu\text{N}$  and then decreases as the preload is further increased to  $3015 \mu\text{N}$ . This suggests that the peak preload for torque performance is approximately equal  $2264 \mu\text{N}$  and that further increases in preload will not improve the performance. The input voltage required to reach peak start-up torque varies with the preload in the system, with it being in the range of  $76.5\text{--}101.6 V_{p-p}$ .

Figure 16(c) shows that the power performance follows an almost identical trend to that of the start-up torque. Performance improves from a low preload to a peak at a preload of  $2264 \mu\text{N}$  and drops off as preload increases further. Peak performance once again is achieved at an input voltage of  $101.6 V_{p-p}$ , where the output power, normalised by the magnet cross-sectional area, is  $72.4 \mu\text{W/mm}^2$ .

An almost identical peak efficiency for the motor occurs at two places in the experimental space. At the point of peak performance,  $101.6 V_{p-p}$  and  $2264 \mu\text{N}$ , the motor operates at an efficiency of 0.1%. At an electrical input of  $76.5 V_{p-p}$  and a preload of  $341 \mu\text{N}$ , the efficiency is 0.11%. The low efficiency is derived from several sources. In terms of design, the use of multiple epoxy bonds reduces the effectiveness of the energy transfer from the piezoelectric element to the stator. This, coupled with fabrication accuracy limitations that result in the resonances not being ideally matched as designed, affected efficiency and produced an electro-mechanical coupling coefficient of 0.06 and a quality factor of 9.96. In terms of the experimental method, the use of the mounting and electrode contacts, although enabling the motor to run using free-free boundary conditions as designed, also affected the motor efficiency. The use of this mounting technique, in conjunction with the conductive epoxy bonds, resulted in a system resistance measured to be  $9.6 \text{ k}\Omega$ . This resistance is more than 30 times larger than the approximately  $300 \Omega$  of the piezoelectric element by itself, and resulted in the necessity to use a much larger input voltage to enable the motor operation leading to reduced efficiency.

Comparing the peak performance results obtained using an increased preload with



the requirements outlined in Section 1, we see that at an input voltage of  $101.6 V_{p-p}$  and a preload of  $2264 \mu N$ , the motor exceeds the torque requirement by 15 times and the power requirement by approximately 10%.

## 6. Conclusion and Future Work

We have successfully designed, fabricated and tested a piezoelectric ultrasonic resonant micro-motor with dimensions that make it suitable for use as the drive system of a *in vivo* tetherless swimming micro-robot. As designed, the motor produces  $1.2 nNm$  of torque at start-up and a maximum output power of  $0.25 \mu W$  with a preload of  $46.6 \mu N$  and an input voltage of  $85 V_{p-p}$ . Normalising these results by the cross-sectional area of the rotor, we obtain a start-up torque of  $23.8 nNm/mm^2$  and a peak output power of  $5 \mu W/mm^2$ . In this configuration, the motor torque exceeds the torque requirement to propel a swimming micro-robot by more than 50%, but generates less than 10% of the power requirement.

Increasing the preload on the motor to  $2264 \mu N$  and the input voltage to  $101.6 V_{p-p}$ , the motor performance is improved to a start-up torque of  $230.4 nNm/mm^2$  ( $29 nNm$ ) and an output power of  $72.4 \mu W/mm^2$  ( $9.1 \mu W$ ) as normalised by the small magnet cross-sectional area. This is an improvement in torque of 16% and power of 262%, when compared with the next smallest comparable piezoelectric ultrasonic resonant micro-motor [23]. In this configuration, the motor meets the requirements to drive a swimming micro-robot upstream in the anterior cerebral artery, as calculated by Liu [8]. The maximum diameter of the motor is  $400 \mu m$ , which was determined by the commercial availability of the magnetic element. This diameter could be reduced to the size of the next largest cross-sectional dimension, i.e.  $250 \mu m$ , without loss in performance. At this dimension, the motor approximately meets the dimensional requirements to travel within the anterior cerebral artery and is five times smaller than the next smallest micro-motor by Kanda et al. [23].

To successfully generate a design that matches the fundamental axial, second torsional and electro-mechanical resonance of the motor, we applied a novel extension to the modelling technique first reported in [13]. This technique uses scaling techniques to reduce the number of finite element runs necessary to achieve the desired design parameters. Using this modelling technique, it was possible to significantly reduce the computational time associated with the motor design, whilst acquiring an intuitive understanding of how the characteristic parameters of the motor affected the resonant frequencies of interest. Moreover, it was possible to include the effects associated with the inclusion of the epoxy bonds.

Future work in this research falls broadly into two categories: preload modifications and performance improvements. Preload modifications arise from the need to increase the preload in the motor from  $46.6 \mu N$  to approximately  $2264 \mu N$  to ensure that the motor performance meets the requirements outlined in Section 1, whilst ensuring the dimensions of the motor remain small enough to be practical for the desired application.

This may be achieved by modifying the types or size of magnets used in the system, or by redesigning the motor to use a mechanical preload system.

There are several areas that could be modified to increase motor performance. Firstly, performance could be improved with further improvements in the machining accuracy of the stator groove depth to ensure all three resonant frequencies are as closely matched as designed. Secondly, changes to the epoxy bonds to improve the quality factor and electro-mechanical coupling of the motor would increase performance. Lastly, the friction coupling can be optimised to ensure the greatest energy transfer to the rotor, with the least amount of loss.

With the necessary modifications to the preload and improvements such as those discussed to improve motor performance, this motor would meet all the requirements to drive a tetherless swimming micro-robot within the human body.

### Acknowledgments

This work was made possible in part by grants SM/07/1616 and SM/06/1208 from the CASS Foundation, grant DP0773221 from the Australian Research Council, and the New Staff and Small Grant Scheme funds from Monash University. Special thanks goes to Ben Johnston at Laser Micromachining Solutions for his help in the fabrication of motor components and the NanoRobotics Laboratory at Carnegie Mellon University for their assistance in the modelling and validation of the motor preload.

### Appendix A. Fabrication and Assembly of Motor

As shown in figure 1, the motor is made up of four key components; the stator, the piezoelectric element, the electrode and the magnetic element. The stator is fabricated from 32-gauge, 304 stainless steel hypodermic tubing (SDR Clinical Technology, Sydney, Australia). The geometry is machined using a 532 nm YAG laser (Q201-HD, JDS Uniphase, Milpitas, USA) and is carried out at Laser Micromachining Solutions (Macquarie University, North Ryde, Australia). The depth of the helical grooves in the tube is determined by a combination of laser power and laser rotation speed. For the motor fabricated and tested in this paper, a power of 34.5 mW and a rotation speed of 900°/min was used. This value was arrived at using a process of elimination, whereby a range of rotation speeds were used to fabricate the stators. Motors were subsequently fabricated, and an estimation of the groove depth was determined from the resonant frequencies of the resulting system. This process was repeated, reducing the range of rotation speeds, to arrive at the final design.

Due to the aspect ratio of the grooves, direct measurement of the groove depth was impossible with the equipment available. However, the use of fabricated motors to derive the groove depth introduces a number of variables that can affect the resulting groove depth estimate. Multiple tests of each laser rotation speed helped to alleviate this; however, obtaining an accurate assessment of the groove depth remained a challenge.

The electrode was also laser machined by Laser Micromaching Solutions and was fabricated from beryllium copper sheet. The piezoelectric element was C203 lead zirconate titanate (Fuji Ceramics, Tokyo, Japan) and the magnetic element was neodymium iron boron (Yuxiang Micro Magnet, Xiamen, China).

The motor was hand assembled. To generate the electrical contact at the base of the magnetic element, an electrode along the length of the magnetic element and onto the base was created from the conductive epoxy Epotek H20E (Elecsys LLC, Providence, RI, USA). This is shown in figure 13(b).

The conducting epoxy was used to bond the magnetic element and the piezoelectric element as well as the electrode and the piezoelectric element. To determine the thickness of these bonds for modelling purposes, a SEM image was taken and the bond thickness measured. A non-conducting epoxy, Araldite 5min (Shelleys, Padstow, NSW, Aust.), was used to bond the stator to the electrode.

## Appendix B. Design and Testing of Motor Mounting

The motor outlined in this paper has been designed to operate with free-free boundary conditions, on the assumption that this is the most likely case when it is used in a tetherless swimming microbot. Generally, a free-free boundary condition is approximated by placing the motor mounting at a motor vibration node. However, due to the design using a fundamental axial and second torsional vibration mode during operation, there was no suitable node for mounting.

To overcome this, a mounting was designed that approximated the free-free boundary conditions of the model. The mounting used a small magnetic element to attract the magnetic element of the motor. Figure 13 shows this set-up. A comparison of the measured electrical impedance of the mounting with the measured impedance of a motor with free-free boundary conditions (the motor held by two light wires) showed good agreement (see figure S2 in the supplementary information). The use of this mounting design is also validated by the results obtained as part of the FEM validation reported in Section 4.

## Appendix C. Determination of Motor Preload: Model and Validation

### *Appendix C.1. Motor Preload*

To determine the approximate preload applied to the rotor due to the magnetic elements in the system, a finite element model was generated (COMSOL v3.3a, Technic Pty. Ltd., Hobart, Australia). The system components were modelled as an axisymmetric structure. Lagrange quadratic elements were used with approximately 1800 elements, although, this number varied due to the auto mesh function used.

The symmetrical axis was assumed to be a perfect insulator, as were the boundaries of the external space. Table C1 outlines the constitutive equations and parameters for the system. Note that all stainless steel elements and all magnetic elements are assumed

to be the same, and all other components are assumed to have to not be affected. (Figure S3 in the supplementary material shows the typical axisymmetric structure of the model.)

**Table C1.** The constitutive equations for magnetic flux density ( $\vec{B}$ ) and associated scalar parameters for the finite element model used to determine the motor preload.  $\mu_r$  is the relative permeability,  $M$  is the magnetisation and  $B_z$  is the z-component of the magnetic flux density.

Component	Constitutive equation	Parameter
Stator	$\vec{B} = \mu_o \mu_r \vec{H}$	$\mu_r = 1.07 \times \exp(-4.661 B_z)$
Rotor sphere	$\vec{B} = \mu_o \mu_r \vec{H}$	$\mu_r = 1.07 \times \exp(-4.661 B_z)$
Piezoelectric element	$\vec{B} = \mu_o \mu_r \vec{H}$	$\mu_r = 1$
Air	$\vec{B} = \mu_o \mu_r \vec{H}$	$\mu_r = 1$
Mounting	$\vec{B} = \mu_o \mu_r \vec{H}$	$\mu_r = 1$
Small magnetic elements	$\vec{B} = \mu_o \vec{H} + \mu_o \vec{M}$	$M = 225000 \text{ A/m}$
Large magnetic elements	$\vec{B} = \mu_o \vec{H} + \mu_o \vec{M}$	$M = 90000 \text{ A/m}$

The preload on the rotor is the component of the rotor magnetisation in the direction of the direction of the axis of symmetry. The magnetisation is determined from

$$\vec{M}_{fz} = \int_v d(\vec{M}_z \times \vec{B}_z),$$

where  $\vec{M}_{fz}$  is the magnetic force in the z-direction,  $\vec{M}_z$  is the magnetisation in the z-direction,  $\vec{B}_z$  is the magnetic flux density in the z-direction and the resultant cross-product is integrated across the volume of the rotor sphere  $v$ .

#### Appendix C.2. Model Validation

To validate the magnetisation FEM, the preload was experimentally measured for a test case. The preload force was measured using an automated stage with an in-built load cell (GSO-50, Transducer Techniques, Temecula, USA). The rotor was connected to the load cell with a light-weight line, the stage was then raised and the force recorded.

The average peak pull-off force recorded was 12.8 mN. If we reproduce the test case in the FEM, we find that the axial component of the magnetisation is 12.4 mN. We see from these results that the FEM produces a good approximation of the measured preload. The experimental results are shown in Figure S4 of the supplementary material.

**References**

- [1] F. Tendick, S.S. Sastry, R.S. Fearing, and M. Cohn. Applications of micromechatronics in minimally invasive surgery. *IEEE/ASME Transactions on Mechatronic*, 3:34–42, 1998.
- [2] M.C. Çavuşoğlu, W. Williams, F. Tendick, and S.S. Sastry. Robotics for telesurgery: Second generation berkeley UCSF laparoscopic telesurgical workstation and looking towards the future applications. *Industrial Robot*, 30:22–29, 2003.
- [3] M.J. Mack. Minimally invasive and robotic surgery. *Journal of the American Medical Association*, 285(5), 2001.
- [4] E.J. Hanly and M.A. Talamini. Robotic abdominal surgery. *The American Journal of Surgery*, 188:19S–26S, October 2004.
- [5] R.A. Li, J. Jensen, and J.C. Bowersox. Microvascular anastomoses performed in rats using a microsurgical telemanipulator. *Computer Aided Surgery*, 5:326–332, 2000.
- [6] M. Hashizume, T. Yasunaga, K. Tanoue, S. Ieiri, K. Konishi, K. Kishi, H. Nakamoto, D. Ikeda, I. Sakuma, M. Fujie, and T. Dohi. New real-time MR image-guided surgical robotic system for minimally invasive precision surgery. *International Journal of Computer Assisted Radiology and Surgery*, 2:317–325, 2008.
- [7] M. Sitti. Voyage of the microbots. *Nature*, 458:1121–11221, 2009.
- [8] K.-C. Liu. *The Dynamics of Combined Axial-Torsional Standing-wave Ultrasonic Motors*. PhD thesis, Faculty of Engineering, 2010.
- [9] B. Watson, J. Friend, and L. Yeo. Piezoelectric ultrasonic micro/milli-scale actuators. *Sensors and Actuators A*, 152:219–233, 2009.
- [10] W. Zhang, G. Meng, and H. Li. Electrostatic micromotor and its reliability. *Microelectronics Reliability*, 45:1230–1242, 2005.
- [11] K. Hori, T. Miyagawa, and K. Ito. Development of ultra-small sized servo actuator with brushless DC motor, planetary gear drive and optical rotary encoder. *International Journal of the Japan Society for Precision Engineering*, 31:1–5, 1997.
- [12] Y. Suzuki, K. Tani, and T. Sakuhara. Development of a new type piezoelectric micromotor. *Sensors and Actuators A*, 83:244–248, 2000.
- [13] B. Watson, J. Friend, and L. Yeo. A study on axial and torsional resonant mode matching for a mechanical system with complex non-linear geometries. *Review of Scientific Instruments*, Accepted, 2010.
- [14] B. Watson, J. Friend, and L. Yeo. Piezoelectric resonant micromotor with a stator diameter of less than 250µm: The proteus motor. *Journal of Micromechanics and Microengineering*, 19:022001–022005, 2009.
- [15] K. Uchino. Piezoelectric ultrasonic motors: Overview. *Smart Material Structures*, 7:273–285, 1998.
- [16] T. Kanda, A. Makino, L. Suzumori, T. Morita, and M.K. Kurosawa. A cylindrical micro ultrasonic motor using a micro-machined bulk piezoelectric transducer. In *IEEE Ultrasonics Symposium*, 2004.
- [17] B.R. Munson, D.F. Young, and T.H. Okiishi. *Fundamentals of Fluid Mechanics*. John Wiley & Sons, Inc., 3rd edition, 1998.
- [18] R.G. Grimes, J.G. Lewis, and H.D. Simon. A shifted block lanczos algorithm for solving sparse symmetric generalized eigenproblems. *SIAM Journal Matrix Applications*, 15:228–272, 1994.
- [19] H. Cease, P.F. Derwent, H.T. Diehl, J. Fast, and D. Finley. Measurement of mechanical properties of three epoxy adhesives at cryogenic temperatures for ccd construction. Internet, November 2006.
- [20] J. Friend, K. Nakamura, and S. Ueha. A piezoelectric micromotor using in-plane shearing of PZT elements. *IEEE/ASME Transactions on Mechatronics*, 9(3):7, 2004.
- [21] K. Nakamura, M. Kurosawa, H. Kurebayashi, and S. Ueha. An estimation of load characteristics of an ultrasonic motor by measuring transient responses. *IEEE Transactions on Ultrasonics*,

*Piezoelectric motor for a micro-robotic applications*

32

- Ferroelectrics and Frequency Control*, 38(5):481–485, 1991.
- [22] K.-C. Liu, J. Friend, and L. Yeo. Rotating bouncing disks, tossing pizza dough, and the behavior of ultrasonic motors. *Physical Review E*, 80:046201, 2009.
- [23] T. Kanda, A. Makino, T. Ono, K. Suzumori, T. Morita, and M.K. Kurosawa. A micro ultrasonic motor using a micro-machined cylindrical bulk PZT transducer. *Sensors and Actuators A: Physical*, 128:1, 2008.
- [24] H. Zhang, S. Dong, S. Zhang, T. Wang, Z. Zhang, and L. Fan. Ultrasonic micro-motor using miniature piezoelectric tube with diameter of 1.0 mm. *Ultrasonics*, 44:e603–e606, 2006.

## Conclusions and Future Work

### 5.1 Conclusions

In this thesis we have demonstrated that by developing a new design methodology for piezoelectric ultrasonic resonant motors, it is possible to realise a motor with geometry and performance suitable for use as a drive system for a tetherless *in vivo* micro-robot. To do so, we have developed three prototypes that experimentally validate our hypotheses, validate the developed modelling techniques and characterise the motor performance.

The key contributions of this thesis are as follows:

- A thorough review of existing micro-actuator designs led to the development of a new actuator classification system based on the underlying physics of the actuator driving force. This, for the first time, allowed a structured examination of the benefits and disadvantages associated with each class of actuator. This examination highlighted that the design of the largest classes of existing piezoelectric ultrasonic resonant micro-motors have numerous disadvantages associated with the stator being fabricated from the piezo-

electric ceramic.

- An understanding of the disadvantages associated with existing designs led to the definition of a new design methodology for piezoelectric ultrasonic resonant micro-motors. This outlined the concept of using the piezoelectric element as a vibration generator, as a means to simplifying the design and allowing a reduction in the overall size. A proof of concept prototype demonstrated the feasibility of this methodology, using commercially available techniques to produce a motor with a stator diameter one-third the size of the next smallest.
- Two novel modelling techniques, the helical spring model and the pseudo-stiffness model, were developed to understand how the parameters of a component with non-linear geometries affect the mechanical resonant frequencies. Analytical modelling techniques are complex and often ineffectual, with finite element modelling being computationally time consuming. The development of the two techniques allowed an intuitive understanding of how the geometric parameters affect the resonant frequencies of interest, while greatly reducing the time and the complexity of the analysis. The modelling techniques were validated using a prototype motor, which also demonstrated the performance improvement gained by closely matching the resonant frequencies of operation. The pseudo-stiffness technique in particular shows great potential as a generalised tool for the analysis and design of a multitude of complex non-linear mechanical systems. The methodology could be applied to other systems where the resonant vibra-



tion is important such as other ultrasonic motor designs, micro-cantilever beam designs, or possibly other classes of motors such as electrostatic. Moreover, the methodology may be used to investigate other parameters, such as the output force or tip displacement of thermal actuators.

- An extension of the pseudo-stiffness model, to create the pseudo-function model, generalised the analysis to encompass the parameters of all the system components. This novel approach to modelling a complex compound system greatly improves the understanding of the system over traditional finite element modelling. The benefits of the technique were demonstrated through a prototype motor design that matched the fundamental axial, second harmonic torsional and electro-mechanical resonant frequencies to within 0.5%.
- For the first time, a piezoelectric ultrasonic resonant micro-motor was fabricated and characterised that could meet the requirements of a drive system for a tetherless *in vivo* microbot. The maximum motor dimension was  $400\text{ }\mu\text{m}$ , driven by the commercial availability of a magnetic element. A reduction in size of this element to  $250\text{ }\mu\text{m}$ , equal to the maximum cross-sectional dimension of the other components, would have a limited effect on the performance and would approximate the geometric requirements outlined in Section 1.3. The maximum recorded start-up torque of the motor was 15 times that required, with the maximum output power 10% greater than the requirement outlined in Table 1.1. To achieve these results, it was necessary to increase the motor preload from the designed  $46.6\text{ }\mu\text{N}$

to 2264  $\mu\text{N}$ .

## 5.2 Future Work

Future research based on the work reported in this thesis falls broadly into three areas: performance improvement, fundamental understanding and applications. Here we broadly outline areas of potential research for each of these areas.

### Performance Improvement

For a motor to be suitable for a prototype tetherless *in vivo* microbot, it is necessary to reduce the overall dimensions of the motor and increase the designed preload. To reduce the motor dimensions requires the design and fabrication of bespoke motor components. If this is carried out, further reductions in the size of the motor below the maximum 250  $\mu\text{m}$  cross-sectional dimension of the fabricated prototype may be possible. An increase in designed preload may come from alternative magnetic element selection, but is most likely to result from a switch to a mechanical preload system. This would require a redesign of the motor to ensure the resonant frequencies remain matched, and would be possible using the pseudo-function model.

Direct performance improvements can arise from changes in two key areas. First, further improvements to the machining of the stator grooves would ensure that the fabricated stator was closer to the design. This would result in more closely matched frequencies in the fabricated motor and a performance improvement. Second, improvements in the bonding of the motor components to improve

the quality factor and electro-mechanical coupling of the motor would increase performance, specifically efficiency. It would also aid reproducibility in the assembled motors.

### **Fundamental Understanding**

Research into an improved fundamental understanding of the motor would also bring improvements in performance. In addition, it would provide useful information to a more generalised motor research audience. One of the key areas for this research is the stator–rotor interaction during operation. An improved understanding of this system could greatly improve the design of the friction coupling, which is the greatest point of inefficiency in the design of a piezoelectric ultrasonic micro-motor.

An extension to the pseudo-function model to include the effects of a rotor and preload would also benefit performance. Such a model should predict the change in resonant frequency due to the introduction of the stiffening preload force. This would give an intuitive understanding of the stiffening effect in motor design, whilst ensuring that the resonant operation frequencies are matched during operation.

### **Applications**

With the availability of a practical micro-motor with a volume of less than  $1\text{ mm}^3$ , numerous applications could be explored. The key application, and the design

aim of this thesis, is the development of a prototype tetherless *in vivo* swimming microbot.

## Bibliography

- [1] U. N. D. of Economic and S. A. P. Division, "World population ageing: 1950-2050," 2002.
- [2] M. Booth, T. Chey, M. Wake, K. Norton, K. Hesketh, J. Dollman, and I. Robertson, "Change in the prevalence of overweight and obesity among young australians, 19691997," *American Journal of Clinical Nutrition*, vol. 77, pp. 29–36, 2003.
- [3] A. Wendelboe, K. Hegmann, J. Biggs, C. Cox, A. Portmann, J. Gildea, L. Gren, and J. Lyon, "Relationships between body mass indices and surgical replacements of knee and hip joints," *American Journal of Preventive Medicine*, vol. 25, pp. 290–295, 2003.
- [4] M. Hawn, J. Bian, R. Leeth, G. Ritchie, N. Allen, K. I. Bland, and S. Vickers, "Impact of obesity on resource utilization for general surgical procedures," *Annals of Surgery*, vol. 241, pp. 821–828, 2005.
- [5] M. Çavuşoğlu, W. Williams, and F. T. S. Sastry, "Robotics for telesurgery: Second generation berkeley/ucsf laparoscopic telesurgical workstation and

- looking towards the future applications," *Industrial Robot*, vol. 30, pp. 22–29, 2003.
- [6] F. Tendick, S. Sastry, R. Fearing, and M. Cohn, "Applications of micromechanics in minimally invasive surgery," *IEEE/ASME Transactions on Mechatronic*, vol. 3, pp. 34–42, 1998.
- [7] M. Mack, "Minimally invasive and robotic surgery," *Journal of the American Medical Association*, vol. 285, no. 5, 2001.
- [8] N. Nguyen, D. Follette, B. Wolfe, P. Schneider, P. Roberts, and J. G. Jr, "Comparison of minimally invasive esophagectomy with transthoracic and transhiatal esophagectomy," *Archives of Surgery*, vol. 135, pp. 920–925, 2000.
- [9] E. Hanly and M. Talamini, "Robotic abdominal surgery," *The American Journal of Surgery*, vol. 188, pp. 19S–26S, October 2004.
- [10] R. Li, J. Jensen, and J. Bowersox, "Microvascular anastomoses performed in rats using a microsurgical telemanipulator," *Computer Aided Surgery*, vol. 5, pp. 326–332, 2000.
- [11] M. Hashizume, T. Yasunaga, K. Tanoue, S. Ieiri, K. Konishi, K. Kishi, H. Nakamoto, D. Ikeda, I. Sakuma, M. Fujie, and T. Dohi, "New real-time MR image-guided surgical robotic system for minimally invasive precision surgery," *International Journal of Computer Assisted Radiology and Surgery*, vol. 2, pp. 317–325, 2008.

- [12] D. Oleynikov, M. Rentschler, A. Hadzialic, J. Dumpert, S. R. Platt, and S. Farritor, "Miniature robots can assist in laparoscopic cholecystectomy," *Surgical Endoscopy*, vol. 19, pp. 473–476, 2005.
- [13] Y. Haga and M. Esashi, "Biomedical microsystems for minimally invasive diagnosis and treatment," *Proceedings of the IEEE*, vol. 92, no. 1, pp. 98–114, 2004.
- [14] N. Birkmeyer, D. Charlesworth, F. Hernandez, B. Leavitt, C. Marrin, J. Morton, E. Olmstead, and G. O'Connor, "Obesity and risk of adverse outcomes associated with coronary artery bypass surgery," *Northern New England Cardiovascular Disease Study Group*, 1998.
- [15] C. Hollands and L. Dixey, "Applications of robotic surgery in pediatric patients," *Surgical Laparoscopy, Endoscopy & Percutaneous Techniques*, vol. 12, no. 1, pp. 71–76, 2002.
- [16] P. Bergman and J. van der Linden, "Atherosclerosis of the ascending aorta as a major determinant of the outcome of cardiac surgery," *Nature Clinical Practice Cardiovascular Medicine*, vol. 2, no. 5, pp. 246–51, 2005.
- [17] R. Fernandes and D. Gracias, "Toward a miniaturized mechanical surgeon," *Materials Today*, vol. 12, 2009.
- [18] A. Freeman and E. Mayhew, "Targeted drug delivery," *Cancer*, vol. 58, pp. 573–583, 1986.
- [19] Y. Lu, J. Yang, and E. Sega, "Issues related to targeted delivery of proteins and peptides," *AAPS Journal*, vol. 8, pp. E466–E478, 2006.

- [20] E. Unger, E. Hersh, M. Vannan, T. Matsunaga, and T. McCreery, "Local drug and gene delivery through microbubbles," *Progress in Cardiovascular Diseases*, vol. 44, pp. 45–54, 2001.
- [21] B. Behkam and M. Sitti, "Design methodology for biomimetic propulsion of miniature swimming robots," *ASME Journal of Dynamic Systems and Measurement Control*, vol. 128, pp. 36–43, 2006.
- [22] M. Manghi, X. Schlagberger, and N. R.R., "Propulsion with a rotating elastic nanorod," *Physical Review Letters*, vol. 96, pp. 68 101–1 – 68 101–4, 2006.
- [23] P. Koeneman, J. Busch-Vishniac, and K. Wood, "Feasibility of micro power supplies for MEMS," *Journal of Microelectromechanical Systems*, vol. 6, no. 4, p. 8, 1997.
- [24] M. Guanying, Y. Guozheng, and H. Xiu, "Power transmission for gastrointestinal microsystems using inductive coupling," *Physiological Measurement*, vol. 28, pp. N9–N18, 2007.
- [25] A. Kurs, A. Aristeidis Karalis, R. Moffatt, J. Joannopoulos, P. Fisher, and M. Soljacic, "Wireless power transfer via strongly coupled magnetic resonances," *Sciencexpress*, June 2007.
- [26] K.-C. Liu, "The dynamics of combined axial-torsional standing-wave ultrasonic motors," Ph.D. dissertation, Faculty of Engineering–Monash University, 2010.



- [27] M. Mehregany, P. Nagarkar, S. Senturia, and J. Lang, "Operation of micro-fabricated harmonic and ordinary side-drive motors," *Proceedings of the IEEE Micro-Electro-Mechanical Systems Workshop*, p. 8, 1990.
- [28] S. Mishihiro, "Rotary ultrasonic motor," *U.S. Patent Number 4,697,117*, vol. U.S. Patent Number 4,697,117, September 1987.
- [29] K. Nakamura, M. Kurosawa, H. Kurebayashi, and S. Ueha, "An estimation of load characteristics of an ultrasonic motor by measuring transient responses," *IEEE Transactions on Ultrasonics, Ferroelectrics and Frequency Control*, vol. 38, no. 5, pp. 481–485, 1991.
- [30] D. Wajchman, D. Liu, J. Friend, and L. Yeo, "An ultrasonic piezoelectric motor utilising a non-circular cross sectioned twisted beam," *IEEE Transactions on Ultrasonics, Ferroelectrics and Frequency Control*, vol. 55, no. 4, pp. 832–840, 2008.



## Publications

### A.1 List of Publications

#### Journal Papers

1. **B. Watson**, J. Friend and L. Yeo, "Piezoelectric ultrasonic resonant motor with stator diameter less than 250  $\mu\text{m}$ : the *Proteus* motor", *Journal of Micromechanics and Microengineering*, 2009, 19, 022001
2. **B. Watson**, J. Friend and L. Yeo, "Piezoelectric ultrasonic micro/milli-scale actuators", *Sensors and Actuators A: Physical*, 2009, 152, 219-233
3. **B. Watson**, L. Yeo and J. Friend, "A Study on axial and torsional resonant mode matching for a mechanical system with complex non-linear geometries", *Review of Scientific Instruments*, 2010, 81, 063901
4. **B. Watson**, J. Friend and L. Yeo, "Modelling and Testing of a Piezoelectric Ultrasonic Micro-Motor Suitable for *In Vivo* Micro-Robotic Applications", *Journal of Micromechanics and Microengineering*, 2010, In review

## Conference Papers

1. **Brett Watson**, James Friend and Leslie Yeo, "Micromotor of Less Than 1 mm<sup>3</sup> Volume for In Vivo Medical Procedures", Proceedings of ICQNM, 2009, 81-85
2. **Brett Watson**, James Friend, Leslie Yeo and Metin Sitti, "Piezoelectric Ultrasonic Resonant Micromotor with a Volume of Less Than 1 mm<sup>3</sup> for use in Medical Microbots", 2009 IEEE International Conference on Robotics and Automation - Kobe, Japan, 12-17 May 2009

## Patents

1. **Brett Watson**, James R. Friend and Leslie Y. Yeo, Piezoelectric actuator for use in micro engineering applications, *Australian Provisional Patent*, # 2007905256, filing date: 20 November 2007.
2. **Brett Watson**, James R. Friend and Leslie Y. Yeo, Piezoelectric actuator for use in micro engineering applications, *United States Provisional Patent*, # 12/644958, filing date: 22 December 2009.

## **A.2 Third International Conference on Quantum, Nano and Micro Technologies – Paper**

### **Micromotor of Less Than 1 mm<sup>3</sup> Volume for In vivo Medical Procedures**

**Brett Watson, James Friend and Leslie Yeo**

*Cancun, Mexico*

February 1–7, 2009

Copyright © 2009 IEEE

DOI 10.1109/ICQNM.2009.14

## Micromotor of Less Than 1 mm<sup>3</sup> Volume for In Vivo Medical Procedures

Brett Watson

James Friend

Leslie Yeo

Monash University  
Dept. of Mechanical Engineering  
Micro/Nanophysics Research Laboratory  
Clayton, Victoria, 3800, Australia  
Brett.Watson@eng.monash.edu.au

### Abstract

*The body's stress response to surgery has been cited as a primary cause of post-operative morbidity and has prompted growth in minimally invasive surgical techniques. The future of such techniques lies in the use of in vivo procedures, but is currently limited by the availability of motors with a volume of less than 1 mm<sup>3</sup>.*

*In response to this we present a piezoelectric ultrasonic resonant micromotor with a volume of approximately 0.75 mm<sup>3</sup>. The motor has a novel helically cut stator that couples axial and torsional resonant frequencies, excited by a lead zirconate titanate element 0.03 mm<sup>3</sup> in volume. The motor performance reaches a start-up torque of 47 nNm and no load angular velocity of 830 rad/s. This gives the motor a power density of 18.4 kW/m<sup>3</sup>. This performance is on the order necessary to propel a swimming microbot in small human arteries.*

### 1. Introduction

The body's stress response to surgery has been cited as a primary cause of post-operative morbidity and complications during post-operative care [14], which has led researchers to search for methods to reduce the stress caused by major surgical traumas [14],[3]. A successful method has been the use of minimally invasive surgery (MIS), which has been shown to reduce the stress caused by major procedures, and has led to new techniques in every speciality of surgical medicine [6].

Currently, catheters and endoscopes are the instruments most widely used during MIS. The instruments are introduced to the body by the surgeon, and require a high level of skill to control [8]. Despite the advances made and successes achieved with these instruments, in many circumstances MIS is not considered to be better than traditional

cut and sew techniques. In such circumstances, current minimally invasive techniques are seen to lead to a loss of dexterity, feel and a compromised view of the procedure, even in the most complex and expensive systems [9].

To rectify this, research is being carried out on systems that will permit procedures to be conducted on the micro-scale using remotely operated micro-robots (microbots). Medical procedures using these devices will require only a small, or possibly no, incision in the body and will permit in vivo techniques to be used. The ultimate aim of such in vivo microbots is to carry out complex tasks including observation, sampling, drug delivery and surgical procedures within the cardiovascular, digestive and lymphatic systems [2].

To work effectively inside the human body, these microbots must be sub-millimetre in size, be able to move rapidly and accurately and conduct procedures with low power consumption. One of the major obstacles to realising such designs is the availability of a practical micromotor with a volume of less than 1 mm<sup>3</sup> to act as a drive system. Numerous methods have been proposed to realise the goal of a motor with a volume of less than 1 mm<sup>3</sup>, the most successful of which include electrostatic [20], electromagnetic [12] and piezoelectric ultrasonic resonant [13] designs. If we examine the driving force used as the basis of design of these motors (electrostatic force, electromagnetic force and the converse piezoelectric effect), we can demonstrate that piezoelectric ultrasonic resonant motors have favourable scaling characteristics [18], high torque low speed outputs and simple construction, leading to the best potential for use as a practical micro-motor.

Some small scale piezoelectric ultrasonic resonant motors have been produced [13, 19], but due to a range of shortcomings common to current piezoelectric ultrasonic resonant designs, a rotational motor with a volume of significantly less than 1 mm<sup>3</sup> has not been achieved. Such shortcomings include the fragility of the motor due to the stator being fabricated from a piezoelectric ceramic, the in-

creased motor complexity arising from requiring multiple electrical input signals and difficulties in fabrication. With a novel stator design, we have been able to simplify current piezoelectric ultrasonic resonant actuators, overcoming many of these shortcomings.

## 2. Basis of Operation

Piezoelectric ultrasonic resonant motors make use of the displacement associated with the excitation of a resonant mode or coupled modes within the motor stator. The carefully selected modes result in an elliptical cyclic motion at the point of contact between the stator and rotor (the stator tip). In conjunction with a friction coupling [16], this ensures a larger angular displacement is imparted on the rotor during one half of the vibration cycle, resulting in a net angular displacement after a complete cycle. The resonant mode(s) of the stator are excited by a harmonic loading from a piezoelectric element, arising from the converse piezoelectric effect.

Research to date has focussed on the use of coupled orthogonal bending modes to elicit elliptical motion at the stator tip [13, 19]. In general, bending modes are excited through the application of two electrical driving signals to a stator fabricated from a piezoelectric material. This results in the shortcomings outlined in Section 1.

For the motor design detailed in this paper, we use coupled axial and torsional resonant modes in place of the orthogonal bending modes. The coupled axial and torsional modes are to be excited by a lead zirconate titanate (PZT) piezoelectric element external to the stator. Fig. 1 demonstrates how the combination of the coupled mode shapes and the phase difference between the axial and torsional components, produces the desired elliptical motion at the stator tip. This methodology allows us to simplify the overall motor which has the following benefits:

- **Reduced complexity** – By coupling the axial and torsional resonant modes through the stator geometry, only one driving signal is required to run the motor.
- **More robust** – The piezoelectric element in the design is not part of the stator. This reduces the proportion of the motor that is fabricated from a piezoelectric ceramic, improving the robustness of the design.
- **Improved fabrication** – The piezoelectric element required is only a simple rectangular prism, making for easier fabrication. Other parts are fabricated by laser micro-machining, a method common in micro-stent and surgical implant fabrication.

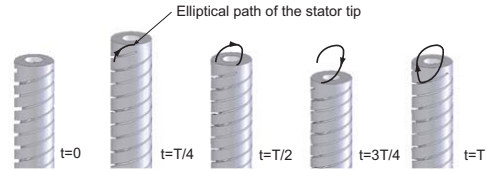


**Figure 1. The axial and torsional resonant modes are coupled through the introduction of helical cuts to the stator. The coupled modes result in the elliptical stator tip motion as shown for one complete vibration cycle. Note:  $t$  is time and  $T$  is period.**

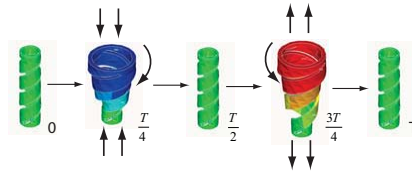


**Figure 2. The exaggerated ANSYS output confirming the motion of the stator during one cycle of period  $T$ .**

## 3 DESIGN AND FABRICATION

An initial helix angle of  $30^\circ$  was chosen based on the study by Wajchman et al. [17]. The study investigated the helix angle of a “twisted beam” and its effect on the coupling of axial and torsional resonance modes. A limited parametric study on the proposed stator geometry was carried out using the finite element analysis program ANSYS V10.0 (ANSYS Inc., Canonsburg, PA, USA). This study included the cut width, cut length and number of cuts (helix starts), and confirmed the elliptical stator tip motion. The exaggerated ANSYS output highlights the coupling of the axial and torsional motion as shown in Fig. 2. The finite element analysis also showed that using a helix angle of  $30^\circ$  lead to a stator design that had only weakly coupled axial and torsional resonant modes, with the axial resonant frequency approximately 30% higher than the equivalent torsional harmonic.

We hypothesise that a design that more closely matches the resonant modes would improve the motor performance. By focusing the parametric study on the number of helix revolutions (the helix angle) it was possible to determine

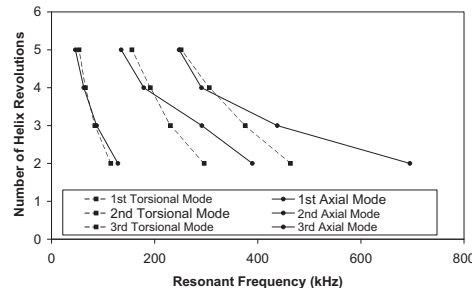


**Figure 3.** The axial and torsional resonant frequencies for the first three harmonics for a stator with three helical cuts and varying helix revolutions. The intersection of the curves identifies a stator geometry that closely matches the axial and torsional resonances.

stator geometries that more closely matched the axial and torsional resonant frequencies. Fig 3 is an extract from this study, demonstrating how the axial and torsional resonant frequencies vary with the number of revolutions in the helical cut. The intersection of the curves identifies a geometry that closely matches the torsional and axial resonant frequencies.

From the study, a stator geometry using 3.5 helix revolutions and three identical helical cuts was selected; Fig. 4 details the geometry dimensions. The motor prototype was fabricated from a 304 stainless steel tube with the helical cuts laser cut at equal circumferential spacing (fabricated by Laser Micromachining Solutions, Macquarie University, NSW, Aust.). A magnetic preload was used as part of the friction coupling, and was measured to be  $53 \mu\text{N}$ . The resonant modes were excited by a  $0.25 \text{ mm} \times 0.25 \text{ mm} \times 0.5 \text{ mm}$  lead zirconate titanate (PZT) element (C203, Fuji Ceramics, Tokyo, Japan). The motor setup is shown in Fig. 5. The motor was trialled for each of the finite element model derived axial/torsional coupled resonant frequencies using a bandwidth of 5% to allow for manufacturing tolerances. The motor demonstrated bi-directional operation with clockwise rotation at the third harmonic, 732 kHz and counterclockwise rotation at the second harmonic, 526 kHz.

To confirm the study results, the ANSYS model was validated using a modified version of the method outlined by Friend et al. [4]. To experimentally determine the resonant modes, this method compares laser doppler vibrometer (LDV) measured displacement spectra at six points on the stator tip. With sensible application, this method allows the resonant modes to be classified directly from these spec-

Object	Dimension ( $\mu\text{m}$ )
Base Tube	
Inside Diameter	200
Outside Diameter	241
Length	985
Helical Cut	
Width	28
Pitch	440
Length	880



**Figure 4.** The stator geometry chosen to closely match the axial and torsional resonant frequencies while ensuring the overall volume remained less than  $0.25 \text{ mm}^3$ .

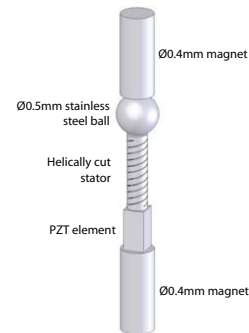


**Figure 5.** The motor set-up included the helically cut  $240 \mu\text{m}$  diameter stator, a  $0.5 \text{ mm}$  diameter stainless steel ball as the rotor, a  $0.25 \text{ mm} \times 0.25 \text{ mm} \times 0.5 \text{ mm}$  PZT element, and two  $0.4 \text{ mm}$  diameter magnets to provide preload, resulting in a motor with a volume of less than  $1 \text{ mm}^3$ .

tra. These results are then compared with those produced by ANSYS. Fig. 6 shows the recorded spectra and comparable ANSYS results for a stator with five helix rotations and two cuts.

## 4 Results

Motor performance was determined using the method by Nakamura et al. [15]. Rotor motion was recorded using a laser doppler velocimeter (Canon LV-20Z, Kiyohara-Kogyodanchi, Utsunomiya-shi, Tochigi-ken, Japan). A maximum clockwise angular velocity of  $830 \text{ rad/s}$  ( $7,925 \text{ rpm}$ ) was recorded at an input of  $20 V_{p-p}$  and  $732 \text{ kHz}$ . Based on the curve in Fig. 7, the average clock-

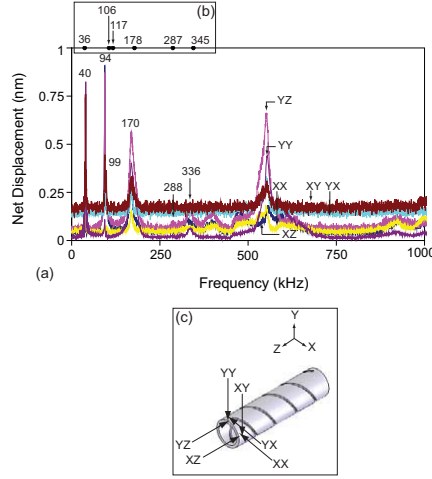


**Figure 6. Finite element analysis validation through the comparison of stator resonant frequencies obtained from (a) LDV recorded displacement spectra and (b) ANSYS calculated frequencies using the measurement positions detailed in (c) for a stator with five helix revolutions and two helical cuts.**

wise start-up torque was 47 nNm with a peak of 51 nNm and a minimum of 39.8 nNm. The fitted exponential curve is derived from the standard curve for a piezoelectric ultrasonic motor [15]. The average braking torque was calculated to be 17.8 nNm. A maximum counterclockwise angular velocity of 1600 rad/s (15,280 rpm) at 32.1 V<sub>p-p</sub> and 526 kHz was recorded; however, the inconsistent nature of the operation prevented the measurement of the complete motor performance.

## 5 Discussion

The reported motor demonstrated bidirectional operation, however, counterclockwise motion was unreliable when compared with clockwise operation. When making use of two sequential torsional modes to obtain bidirectional motion, as is the case here, we expect the clockwise direction to be superior due to the tendency of the stator to “uncurl” in that direction during extension of the stator. This is a result of the helical geometries used in the design and will benefit the performance of the motor through an increased tangential displacement for each cycle. By matching the

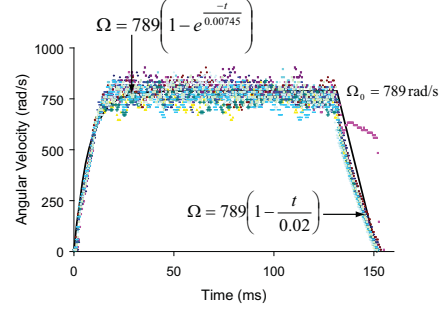


**Figure 7. The angular velocity vs. time curve, as derived by the method in [15], for an applied step voltage of 20 V<sub>p-p</sub>, preload of 53 μN and an operating frequency of 732 kHz. The fitted curve is average obtained across all runs as recorded by the points.**

desired operational frequencies of the motor to the resonant mode of the piezoelectric element we will ensure the maximum motor performance, which will enable a consistent bi-directional operation to be achieved. Further research into the exact geometry mechanisms driving the changes in the axial/torsional resonant frequencies is required to realise the successful matching of piezoelectric and stator resonant modes.

We now give an example of how such a motor may be used for in vivo medical procedures. We examine a “swimming microbot” that uses an E.coli-like flagella as a means of propulsion. Such microbots have been highlighted as having great potential for use in in vivo medical procedures due to the low Reynolds number propulsion system [1]. We use Higdon’s model for flagellar propulsion [11], to determine the average power required for swimming in small human arteries:

$$\bar{P} = 6\pi\mu A\bar{U}^2\eta_0^{-1}K$$

where blood has a viscosity of approximately  $\mu = 0.004$  Pa·s [7];  $A$ , is the radius of the swimming microbot which we assume to be approximately the size of the motor, 150 μm,  $K$  is the Stokes’ law correction for a prolate spheroid, 2.7 [10], and  $\eta_0^{-1} = 200$  from Higdon’s results. For useful operation, the device should at least swim as fast as the blood flow, in the case of the right central retinal artery—a suitable example of a location both difficult to reach by other means and presumably one where this device would be used— $\bar{U} \approx 6.0$  cm/s [5], giving a required input power of 24 μW.

The average power output of the motor is approximately



$(\phi_{max}T_{max})/4 = 9.75 \mu\text{W}$ , where  $\phi_{max}$  is the maximum clockwise velocity and  $T_{max}$  is the average start-up torque. Although this power is smaller than what is required, it is potentially not out of reach of such a device.

## 6 Conclusion and Future Work

We have demonstrated a motor with potential applications in in vivo medical procedures. The novel stator design coupling axial and torsional resonant modes simplifies current piezoelectric ultrasonic resonant designs and results in a motor volume of less than  $1 \text{ mm}^3$ . The motor has a peak torque of  $51 \text{ nNm}$  and a maximum rotational velocity in excess of  $15,000 \text{ rpm}$ . The motor performance was theoretically shown to be significant enough to propel a swimming microbot in the human body.

Future work on this design will focus on two areas; improved performance and reliability, and applications. To improve the performance of the motor, further research will be conducted to develop an analytical model of the motor. This model will act as a design tool to allow the axial and torsional stator resonances to be more closely matched to the thickness resonance of the piezoelectric element. This is expected to improve the motor performance and produce stable bi-directional operation. Research will also be conducted into creating a more reliable and compact rotor/preload arrangement, ensuring the motor is ready to be used in a range of applications. Of a main interest in application trials will be to trial the motor in conjunction with a flagella propulsion system, confirming the theoretical prediction outlined in Section 5.

## References

- [1] B. Behkam and M. Sitti. Design methodology for biomimetic propulsion of miniature swimming robots. *ASME Journal of Dynamic Systems and Measurement Control*, 128:36–43, 2006.
- [2] F. Cepolina, B. Challacombe, and R. Michelini. Trends in robotic surgery. *Journal of Endourology*, 19(8):940–951, 2005.
- [3] J. Desborough. The stress response to trauma and surgery. *British Journal of Anaesthesia*, 85(1):109–117, 2000.
- [4] J. Friend, K. Nakamura, and S. Ueha. A torsional transducer through in-plane shearing of paired planar piezoelectric elements. *IEEE Transactions on Ultrasonics, Ferroelectrics, and Frequency Control*, 51(7):870–877, 2004.
- [5] G. Fuchsiger-Mayrl, K. Polak, A. Luksch, E. Polska, G. Dorner, G. Rainer, H.-G. Eichler, and L. Schmetterer. Retinal blood flow and systemic blood pressure in healthy young subjects. *Graefes' Archive for Clinical and Experimental Ophthalmology*, 239(9):673–677, 2001.
- [6] K. Fuschs. Minimally invasive surgery. *Endoscopy*, 34:154–159, 2002.
- [7] J. Galduróza, H. Antunesb, and R. Santos. Gender- and age-related variations in blood viscosity in normal volunteers: A study of the effects of extract of allium sativum and ginkgo biloba. *Phytomedicine*, 14:447–451, 2007.
- [8] Y. Haga and M. Esashi. Biomedical microsystems for minimally invasive diagnosis and treatment. *Proceedings of the IEEE*, 92(1):98–114, 2004.
- [9] E. Hanly and M. Talamini. Robotic abdominal surgery. *The American Journal of Surgery*, 188:19S–26S, October 2004.
- [10] J. Happel and H. Brenner. *Low Reynolds Number Hydrodynamics*. Prentice Hall, Englewood Cliffs, NJ, 1965.
- [11] J. Higdon. The hydrodynamics of flagellar propulsion: Helical waves. *Journal of Fluid Mechanics*, 94:331–351, 1978.
- [12] K. Hori, T. Miyagawa, and K. Ito. Development of ultra-small sized servo actuator with brushless DC motor, planetary gear drive and optical rotary encoder. *International Journal of the Japan Society for Precision Engineering*, 31:1–5, 1997.
- [13] T. Kanda, A. Makino, L. Suzumori, T. Morita, and M. Kurosawa. A cylindrical micro ultrasonic motor using a micro-machined bulk piezoelectric transducer. In *IEEE Ultrasonics Symposium*, 2004.
- [14] H. Kehlet and D. W. Wilmore. Fast-track surgery. *British Journal of Surgery*, 92(1):3–4, 2005.
- [15] M. Nakamura, K. and Kurosawa and S. Ueha. Characteristics of a hybrid transducer-type ultrasonic motor. *IEEE Transactions on Ultrasonics, Ferroelectrics, and Frequency Control*, 38(3):6, 1991.
- [16] K. Uchino. Piezoelectric ultrasonic motors: Overview. *Smart Material Structures*, 7:273–285, 1998.
- [17] D. Wajchman, D. Liu, J. Friend, and L. Yeo. An ultrasonic piezoelectric motor utilising a non-circular cross sectioned twisted beam. *IEEE Transactions on Ultrasonics, Ferroelectrics and Frequency Control*, 55(4):832–840, 2008.
- [18] Z. Wang. Nanopiezotronics. *Advanced Materials*, 19:889–892, 2007.
- [19] H. Zhang, S. Dong, S. Zhang, T. Wang, Z. Zhang, and L. Fan. Ultrasonic micro-motor using miniature piezoelectric tube with diameter of  $1.0 \text{ mm}$ . *Ultrasonics*, 44:e603–e606, 2006.
- [20] W. Zhang, G. Meng, and H. Li. Electrostatic micromotor and its reliability. *Microelectronics Reliability*, 45:1230–1242, 2005.

### **A.3 2009 IEEE International Conference on Robotics and Automation – Paper**

Piezoelectric Ultrasonic Resonant Micromotor with a  
Volume of Less Than 1 mm<sup>3</sup> for use in Medical  
Microbots

**Brett Watson**, James Friend, Leslie Yeo and Metin Sitti

*Kobe, Japan*

May 12–17, 2009

Copyright © 2009 IEEE

2009 IEEE International Conference on Robotics and Automation  
Kobe International Conference Center  
Kobe, Japan, May 12-17, 2009

## Piezoelectric Ultrasonic Resonant Micromotor with a Volume of Less Than $1 \text{ mm}^3$ for use in Medical Microbots

Brett Watson, James Friend, Leslie Yeo and Metin Sitti

**Abstract**—To improve on current methods of minimally invasive surgery, research is being carried out on systems that will permit procedures to be conducted on the micro-scale using remotely operated micro-robots. One of the major stumbling blocks to meeting this need has been the absence of a practical micromotor with a volume of less than  $1 \text{ mm}^3$  with which to drive these devices. To rectify this, we present a piezoelectric ultrasonic resonant micromotor with a volume of approximately  $0.75 \text{ mm}^3$ . The motor uses a novel helically cut stator that matches axial and torsional resonant frequencies, excited by a lead zirconate titanate element  $0.03 \text{ mm}^3$  in volume. An earlier motor using the same stator design, but a larger overall volume, achieved a start-up torque of  $47 \text{ nNm}$  and no load angular velocity of  $830 \text{ rad/s}$ . This performance is on the order necessary to propel a swimming microbot in small human veins.

### I. INTRODUCTION

By 2050, the United Nations Department of Economic and Social Affairs Population Division reports that the number of older persons ( $>60$  years) in the world will exceed the number of young persons ( $<15$  years) for the first time in history [1]. Such an increase in the percentage of older persons will have a profound effect on the health care system. One method to help alleviate this is the increased use of minimally invasive surgery (MIS). MIS has been shown to decrease operation times and reduce hospital stays [2], alleviating some of the increased demand for hospital resources that comes with an ageing population.

To improve on current minimally invasive methods, research is being carried out on systems that will permit procedures to be conducted on the micro-scale in vivo, using remotely operated micro-robots (microbots). The ultimate aim of in vivo microbots is to carry out complex tasks including observation, sampling, drug delivery and performing surgical procedures within the cardiovascular, digestive and lymphatic systems. To facilitate the development of such devices, a practical micromotor with a volume of less than  $1 \text{ mm}^3$  must be realised. These motors would be used not only to drive potential microbots, but also for the actuation of any tools that may be necessary to carry out the procedures (forceps, scalpel etc.).

Numerous designs have been proposed for small scale motors, the most successful of which include electrostatic [3], electromagnetic [4] and piezoelectric ultrasonic resonant [5] designs. By examining the physics of operation of the various

motor designs, specifically the driving force used as the basis of design (electrostatic, electromagnetic and converse piezoelectric effect), it can be demonstrated that piezoelectric ultrasonic resonant motors have the largest potential for use as a practical micro-motor at sub-millimeter scales.

Despite having a large potential and despite some small scale piezoelectric ultrasonic resonant motors having been developed [5], [7], a practical sub-millimeter scale motor has not been achieved. We attribute this to a range of shortcomings that is common to current piezoelectric ultrasonic resonant designs. These include:

- Fragility – The stator of current designs is fabricated from a piezoelectric material. This makes the motors fragile to handle and potentially fragile during operation.
- Complex – Existing designs use multiple driving signals which lead to a complexity of control and the difficulty associated with multiple stator electrodes.
- Difficult to fabricate – The fabrication of small scale stators from a piezoelectric ceramic, with multiple electrodes is difficult, with the difficulty increasing as the scale decreases.

Through the use of a novel stator design that couples axial and torsional resonant frequencies, we have overcome many of these shortcomings. This has allowed us to take a significant step towards a practical motor with a volume of less than  $1 \text{ mm}^3$ .

### II. BASIS OF OPERATION

Piezoelectric ultrasonic resonant motors make use of the converse piezoelectric effect. Specifically, a harmonic electrical input is applied to the piezoelectric element, which results in a harmonic strain in the direction of piezoelectric polarisation. With careful selection of electrical input frequency, the harmonic strain will excite a resonant mode (or modes) within the stator.

The goal of all stator designs is to effectively use the excited resonant modes to produce an elliptical motion at the stator tip (the point of contact between the stator and rotor, see Fig. 4). An elliptical stator tip motion is desirable as it results in the stator imparting both a contact (normal) and driving (tangential) force on the rotor, resulting in the rotor being driven by friction.

The method by which this is achieved is known as the friction coupling. The principle of the friction coupling is to ensure that a larger contact force is exerted between the rotor and the stator for one half of the vibration cycle than the other half. Using a coulombic friction model, we can see

B. Watson, J. Friend and L. Yeo are with the Department of Mechanical and Aerospace Engineering, Monash University, Clayton, Vic, 3800, Australia. james.friend@eng.monash.edu.au  
M. Sitti is with the NanoRobotics Laboratory, Carnegie Mellon University, Forbes Avenue, Pittsburgh, PA 15213 USA

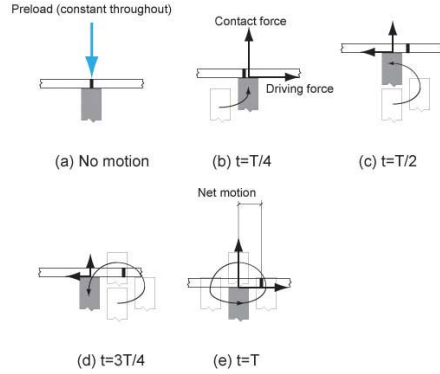


Fig. 1. By applying a "preload" to the rotor, it remains in contact with the stator for the complete cycle, ensuring a repeatable output. The elliptical motion provides a greater contact (and hence driving force) is applied during part of the cycle (b) and (e), than the other (c) and (d), resulting in a net motion.

that the cyclic contact force leads to a cyclic frictional force which, when time averaged across one stator cycle, results in a net work at the rotor in a given direction. This leads to a net motion of the rotor. We can see this illustrated in Fig. 1.

To ensure a constant contact force and repeatable rotor motion, a preload is used. This is a normal force on the rotor in the opposite direction to that imposed by the stator and is usually a magnetic, weight or spring force.

The most successful and popular designs to date use coupled orthogonal bending modes to elicit the elliptical motion at the stator tip [5], [7]. In general, the orthogonal modes are excited through the application of two electrical driving signals to a piezoelectric stator with multiple electrodes. Such designs carry the shortcomings described in Section I.

The design reported in this paper couples axial and torsional resonant modes of the stator. These modes are excited by a lead zirconate titanate (PZT) piezoelectric element external to the stator, which results in the desired elliptical stator tip motion. Fig. 2 demonstrates how the combination of the coupled mode shapes and the phase difference between the axial and torsional components, produces the desired elliptical motion at the stator tip. This methodology allows us to simplify the overall motor which has the following benefits:

- Less fragile – The proportion of piezoelectric ceramic used in the motor is greatly reduced, improving the robustness of the design. Also, the piezoelectric element is only used to excite a resonant mode, and does not operate at resonance itself. This improves the service life of the motor.
- Less complex – By coupling the axial and torsional resonant modes through the stator geometry, only one driving signal is required to run the motor.
- Easier to fabricate – The piezoelectric element is only

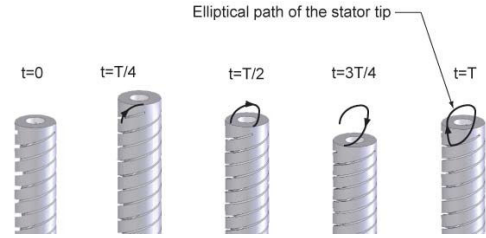


Fig. 2. The helical cuts in the stator allow the axial and torsional resonant modes to be coupled. This results in the desired elliptical stator tip motion as illustrated for one complete cycle. Note:  $t$  is time and  $T$  is period.

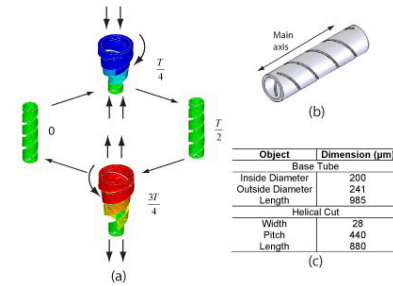


Fig. 3. The (a) exaggerated ANSYS output confirming the motion of the stator during one cycle of period  $T$  as a consequence of the (b) helically-slotted tubular geometry of the stator. The (c) dimensions of the stator are on the order of hundreds of micrometers providing an overall stator volume of approximately  $0.04 \text{ mm}^3$ .

a simple rectangular prism, making for easier fabrication. Other parts are fabricated by laser micro-machining, a method common in micro-stent and surgical implant fabrication.

### III. DESIGN AND TESTING

Based on the work by Wajchman et al. [9] an initial stator design using two helical revolutions (a helix angle of  $30^\circ$ ) was selected. The finite element analysis program ANSYS V10.0 (ANSYS Inc., Canonsburg, PA, USA) was used to conduct a limited parametric study on the proposed stator geometry, including cut width, cut length and number of cuts (helix starts). This study was used to determine a robust, geometric design and confirm the elliptical stator tip motion; the design however, is to be optimized at a later stage. Fig. 3 shows the resultant motion obtained through the selected stator design. The exaggerated ANSYS output highlights the coupling of the axial and torsional motion.

The fabricated design consists of a 304 stainless steel tube, with two diametrically opposite helical cuts removed (fabricated by Norman Noble Inc., Highland Heights, OH, USA), as detailed in Fig. 3. The piezoelectric element is a hard composition lead zirconate titanate (PZT) (C203, Fuji Ceramics, Tokyo, Japan), 3.5 mm in length, 2.5 mm in width, 0.27 mm in thickness, thickness poled, and was chosen due

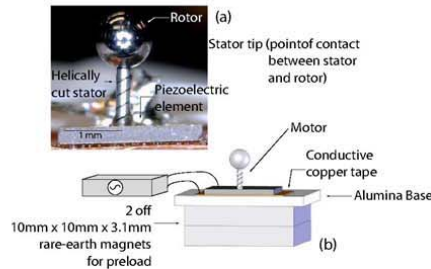


Fig. 4. A photograph of the motor (a), with a  $\varnothing 241$  m helically cut stator,  $\varnothing 1$  mm stainless steel ball (the rotor) and C203 PZT element. The motor is (b) connected to a signal generator, with copper tape atop an alumina base and magnets beneath to provide preload.

to availability. This was bonded by epoxy to one end of the helically cut stator to excite the stator's coupled resonant modes. A conductive copper tape was used to attach the PZT/stator component to an alumina base for testing.

Due to the small scale, a magnetic friction coupling was chosen. A stainless steel ball, 1 mm in diameter, served as a rotor, and was acted on by the magnetic preload. The arrangement of the motor components is shown in Fig. 4.

The axial response spectrum was recorded using a scanning laser doppler vibrometer (LDV) and associated software (MSA-400, Polytec GmbH, Waldbronn, Germany). The LDV measured the displacement of the stator tip in the direction of the stator's main axis (see Fig. 3) while simultaneously exciting all frequencies in the 0-1 MHz band. Peaks in the axial motion of the stator tip, are stator resonant frequencies. The axial spectrum is shown in Fig. 5. The mode at each resonant frequency was further analyzed using the scanning LDV to record the stator tip profile during one vibration cycle. Using the displacement profile, the resonant mode could be classified into an axial or bending based mode. As demonstrated in Fig. 5, an axial mode has an approximately uniform displacement across the tip. In comparison, a bending mode has a displacement change from positive to negative across the tip. Following the classification of modes, the motor was trialled at all modes that were axially based (axial/torsional coupled). Using a signal generator and amplifier (Rohde & Schwarz-SML 01 and NF-HSA 4501, North Ryde, NSW, Aust.), the PZT element was driven at each resonant frequency, and the performance was recorded.

Performance was determined using the method outlined by Nakamura et al. [11]. Rotor motion was recorded using a digital high speed camera (Olympus i-speed, Olympus Australia, Mount Waverley, Vic, Aust) at 1000 frames per second. The angular velocity vs. time data points were determined using the Olympus i-speed image processing software (V1.16, Olympus Industrial America, Orangeburg, NY, USA). The motor was found to have the highest start-

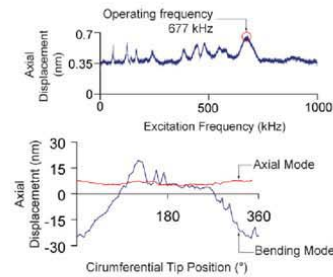


Fig. 5. Scanning LDV outputs including (a) the axial response spectrum for the stator tip that highlights resonant frequencies through spectral peaks and (b) the uniform stator tip profile of an axial mode (77 kHz, 19.3  $V_{p-p}$ ) and the varying profile of a bending mode (197 kHz, 20.3  $V_{p-p}$ ).

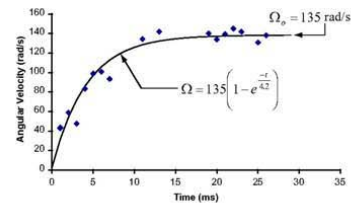


Fig. 6. Angular velocity vs. time results for an applied step voltage of 28.1  $V_{p-p}$  and an operating frequency of 677 kHz. The fitted curve is derived using the method outlined in [11].

up torque and rotational velocity when driven at the stator axial based resonance with the largest amplitude, 677 kHz. Applying a step input of 28.1  $V_{p-p}$  as measured with an oscilloscope (LeCroy WaveJet 334, Chestnut Ridge, NY, USA), resulted in the angular velocity vs. time curve shown in Fig. 6. The fitted exponential curve is derived from the standard curve for a piezoelectric ultrasonic motor [11].

The no load angular velocity recorded for the motor was 135 rad/s (1295 rpm). Using this as an input for the method outlined in [11] the maximum start-up torque, based on the curve shown in Fig 6, was calculated to be 13 nNm. For the chosen operating mode, the motor had an operating frequency range of 652–682 kHz. The performance of this prototype compares well with other piezoelectric ultrasonic micro-motors, with 52% of the torque achieved at 32% of the size of the most comparably sized stator [5].

#### IV. IMPROVED PERFORMANCE THROUGH MORE STRONGLY COUPLED RESONANT MODES

From the initial study we can see that a motor design that couples axial and torsional resonant modes achieves a similar performance to existing motor designs, but at a smaller scale. However, during the analysis it was found that the axial and torsional modes of the initial design were only weakly coupled, with the axial resonant frequency approximately 30% higher than the equivalent torsional harmonic. This



arose from the initial design being based on a “twisted beam” structure. We hypothesise that a design that more strongly matches the axial and torsional modes would improve motor performance.

To achieve such a design, we carried out a finite element parametric study using ANSYS V10.0 (ANSYS Inc., Canonsburg, PA, USA). The aim of the study was to determine the set of stator geometric parameters required to strongly couple the axial and torsional resonant modes. The parameters examined were:

- Stator Length ( $L_z$ )
- Ratio of internal to external diameter ( $\frac{D_i}{D_o}$ )
- Cut width (CW)
- Number of cuts ( $N_c$ )
- Number of helix turns (helix pitch) ( $N_r$ )

Internal and external diameter of the stator were fixed at the values of a 32-gauge tube (smallest commercially available tube). Material density ( $\rho$ ) was kept constant for stainless steel.

By using a modified version of Wittrick’s spring stiffness model [18] we were able to reduce the parameters to only include the stator length ( $L_z$ ) and the stator’s equivalent axial ( $K_x$ ) or torsional ( $K_r$ ) spring stiffness. Using Buckingham’s Pi theorem we were then able to collapse the data using equation 1. The collapsed data is shown in Fig. 7.

$$\text{Log}\left(\frac{F_x}{n}\right) = \frac{1}{2} \text{Log}\left(\frac{K_x}{\rho}\right) - \frac{3}{2} \text{Log}(L_z) \quad (1)$$

where  $F$  is the resonant frequency,  $n$  is the harmonic number associated with the resonant frequency and  $x = e$  (axial) or  $x = r$  (torsional). We refer to the left-hand side of the equation as the “Non-dimensional resonant frequency” and the right hand side of the equation as the “Non-dimensional geometric parameter”.

From the study we found it was possible to obtain a multiple sets of geometric parameters that match the axial and torsional resonant frequencies. We also noted that the number of helix turns and number of helical cuts being the most important parameters in achieving this.

To validate the ANSYS model and confirm the study results, a modified version of the method outlined by Friend et al. [12] was used. This method compares LDV measured displacement spectra at six points on the stator tip. With sensible application, this method allows the mode to be classified directly from these spectra. Fig. 8 shows the recorded spectra and comparable ANSYS results for a stator with five helix rotations and two cuts.

From the study, a stator geometry using 3.5 helix revolutions and three identical helical cuts was chosen. Geometry dimensions are detailed in Fig. 9. The revised prototype was fabricated from a 304 stainless steel tube with the helical cuts laser cut at equal circumferential spacing (Laser Micromachining Solutions, Macquarie University, NSW, Aust.). The magnetic preload was increased through the use of an

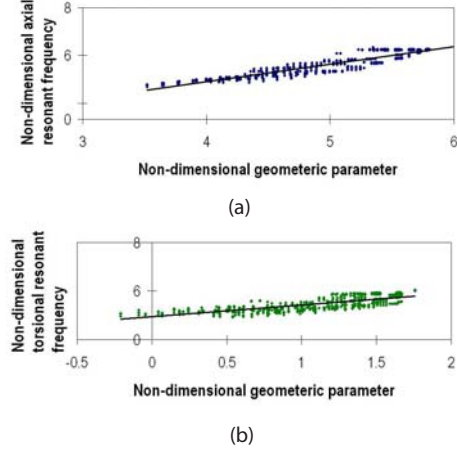


Fig. 7. Finite element analysis was used to determine the axial and torsional resonant frequencies of the stator whilst varying the geometric design parameters. These results were then collapsed using Buckingham’s Pi Theorem (equation 1) to give the non-dimensionalised axial (a) and torsional (b) results shown here.

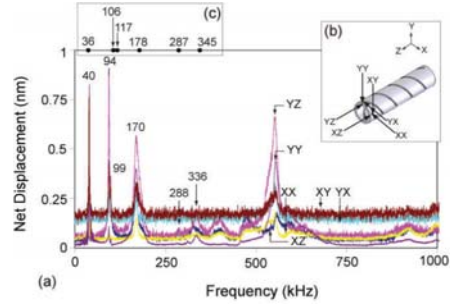


Fig. 8. Comparison of stator resonant frequencies obtained from (a) LDV recorded displacement spectra, using the measurement positions detailed in (b), and (c) ANSYS calculated frequencies for a stator with five helix revolutions and two helical cuts.

additional NdFeB magnet, 0.4 mm in diameter and 1 mm in length. This was necessary to cope with the increase in performance of the revised design. All other aspects of the set up were the same as for the motor described in Section III.

The motor was trialled for each of the finite element model derived axial/torsional coupled resonant frequencies using a bandwidth of  $\pm 5\%$  to allow for manufacturing tolerances. The motor demonstrated bi-directional operation with clockwise rotation at the third harmonic, 732 kHz and counterclockwise rotation at the second harmonic, 526 kHz. As in Section III motor performance was determined using the method by Nakamura et al. [11]. Rotor motion was recorded using a laser doppler velocimeter (Cannon LV-20Z, Kiyohara-Kogyodanchi, Utsunomiya-shi, Tochigi-ken,

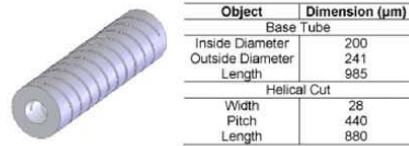


Fig. 9. Revision of the stator geometry following further analysis allowed the axial and torsional resonant frequencies to be more closely matched.

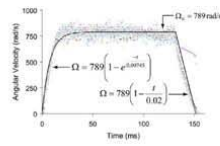


Fig. 10. Angular velocity vs. time results for an applied step voltage of  $20 V_{p-p}$  and an operating frequency of 732 kHz. The fitted curve is derived from the method in [11] and is the average obtained across all runs.

Japan). A maximum clockwise angular velocity of 830 rad/s (7,925 rpm) was recorded at an input of  $20 V_{p-p}$  and 732 kHz. Based on the curve in Fig. 10, the average clockwise start-up torque was 47 nNm with a peak of 51 nNm and a minimum of 39.8 nNm. The average breaking torque was calculated to be 17.8 nNm. A maximum counterclockwise angular velocity of 1600 rad/s (15,280 rpm) at  $32.1 V_{p-p}$  and 526 kHz was recorded; however, the inconsistent nature of the operation prevented the measurement of the complete motor performance.

#### V. SMALL SCALE MOTOR

The most recent motor set up makes use of this increased performance to produce a design with a volume of approximately  $0.75 \text{ mm}^3$ . It must be noted that this volume excludes the second large rare earth magnet used for the preload.

In this design, the original piezoelectric element is replaced with a PZT element with dimensions  $250 \mu\text{m} \times 250 \mu\text{m} \times 500 \mu\text{m}$ . Epotek H20E (Elecsys LLC, Providence, RI, USA) silver conducting epoxy is used to provide the connections between the PZT element and electrical wiring and PCB mounting board. Fig. 11 shows the experimental setup. The motor was operated in the clockwise and counterclockwise directions.

#### VI. DISCUSSION

By using a stator geometry that more strongly couples the axial and torsional resonant modes, the motor performance was substantially improved. Angular velocity has been improved by a minimum of 5.5 times across all runs, with the start-up torque increased by a minimum of 3 times. A proportion of this improvement can be attributed to the increased preload; however, the increase in preload is considered to be substantially less than the improvement in performance.

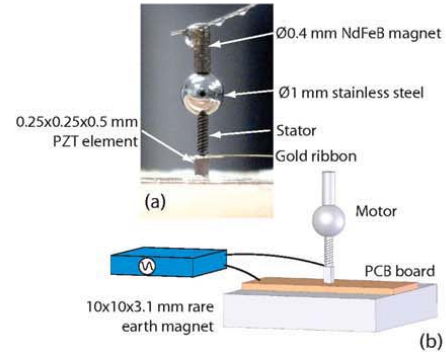


Fig. 11. A photograph of the motor (a), that uses a small lead zirconate titanate (PZT) element, reducing the motor volume to approximately  $0.75 \text{ mm}^3$ . The motor is (b) connected to a signal generator, using gold ribbon and a PCB board with silver conducting epoxy connection.

The revised stator geometry also demonstrated bi-directional operation, an improvement over the initial tested design. Counterclockwise operation however, was unreliable when compared with clockwise operation. This can be attributed to the increased angular displacement achieved during each cycle in the clockwise direction due to the stator's tendency to uncurl in that direction during axial displacement. This same tendency will hinder motion in the counterclockwise direction. By ensuring future motors match the PZT thickness resonance with the operating frequencies, this will be less pronounced, enabling reliable bi-directional operation to be achieved.

The motor design has been demonstrated to work using a micro-scale piezoelectric element. It is not expected that this new design will lose performance over the older, larger designs due to the increase in the thickness of the piezoelectric element. This will allow the stator and PZT resonance modes to be more easily matched and enable the use of higher input voltages. However, to complete the design a revised friction coupling not using a large magnetic element must be arrived upon.

To give an example of the potential application for such a motor, we examine a "swimming microbot" that uses an E.coli like flagella as a means of propulsion. Such microbots have been highlighted as having a great potential for use in *in vivo* medical procedures due to the low Reynolds number propulsion system [13]. These robots are prime candidates for the next generation of MIS discussed in Section I. The flagellum would be attached directly to the rotor of the piezoelectric motor discussed in this paper. A concept design is illustrated in Fig. 12.

Using Higdon's model for flagellar propulsion [14], we may determine the average power required for swimming in small human arteries from:

$$\bar{P} = 6\pi\mu A\bar{U}^2\eta_0^{-1}K$$

where blood has a viscosity of approximately  $\mu = 0.0035 \text{ Pa}\cdot\text{s}$

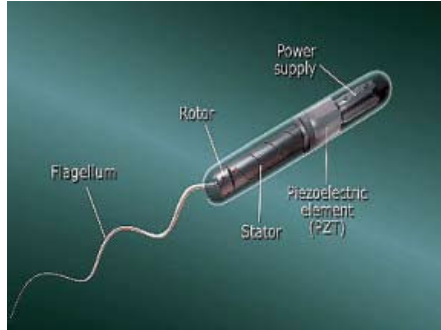


Fig. 12. A concept design of a "swimming microbot" using the piezoelectric ultrasonic resonant micromotor.

s [15],  $A$ , is the radius of the swimming microbot which we'll assume to be approximately the size of the motor –  $150\text{ }\mu\text{m}$ ,  $K$  is the Stoke's law correction for a prolate spheroid – 2.7 [16], leaving only the swimming speed  $\bar{U}$  to be defined, if we take Higdon's results and set  $\eta_0^{-1} = 200$ . If we assume the device should swim at a nominal velocity of  $2\text{ cm/s}$  against the blood flow, and consider a vein in the eye as a suitable example of a location both difficult to reach by other means and presumably one where this device would be used,  $\bar{U} \approx 2 + 1.9\text{ cm/s}$  [17], giving a required input power of  $8.1\text{ }\mu\text{W}$ .

The average power output of the motor is approximately  $(\phi_{max}T_{max})/4 = 9.75\text{ }\mu\text{W}$ , where  $\phi_{max}$  is the maximum clockwise velocity and  $T_{max}$  is the average start-up torque. As can be seen, this is in excess of what is required in the above example.

## VII. CONCLUSION

We have demonstrated a motor with a volume of less than  $1\text{ mm}^3$ . This was achieved through the use of a novel stator design that coupled axial and torsional resonant modes, simplifying current piezoelectric ultrasonic resonant designs and making use of the thus far unfulfilled potential of this class of motors. Motor performance was shown to increase greatly by ensuring the fundamental axial and torsional resonant modes were strongly coupled through careful geometric design. This level of performance was demonstrated to be enough to theoretically propel a swimming microbot in the human body. A continued improvement in this motor may lead to the advances in minimally invasive surgery necessary to help overcome the strains that will be placed on the health care systems of the world as the population continues to age.

## VIII. ACKNOWLEDGMENTS

This work was made possible in part by grants SM/07/1616 and SM/06/1208 from the CASS Foundation, grant DP0773221 from the Australian Research Council, and the New Staff and Small Grant Scheme funds from Monash University. "This work was performed in part at the Macquarie/ATP node of the Australian National Fabrication

Facility. A company established under the National Collaborative Research Infrastructure Strategy to provide nano and microfabrication facilities for Australia's researchers. [sic]"

## REFERENCES

- [1] United Nations Department of Economic and Social Affairs Population Division, "World Population Ageing: 1950-2050", 2002 *World Assembly on Ageing*, 2002
- [2] N.T. Nguyen and D.M. Follette and B.M. Wolfe and P.D. Schneider and P. Roberts and J.E. Goodnight Jr, Comparison of Minimally Invasive Esophagectomy With Transthoracic and Transhiatal Esophagectomy, *Archives of Surgery*, vol. 135, 2000, pp 920-925.
- [3] M. Mehregany and P. Nagarkar and S.D. Senturia and J.H. Lang, Operation of Microfabricated Harmonic and Ordinary Side-Drive Motors, *Proceedings of the IEEE Micro-Electro-Mechanical Systems Workshop*, 1990, pp 1-8
- [4] K. Hori and T. Miyagawa and L. Ito, Development of Ultra-Small Sized Servo Actuator with Brushless DC Motor, Planetary Gear Drive and Optical Rotary Encoder, *International Journal of the Japan Society for Precision Engineering*, vol. 31, 1997, pp 1-5
- [5] T. Kanda and A. Makino and L. Suzumori and T. Morita and M.K. Kurosawa, A Cylindrical Micro Ultrasonic Motor using a Micro-machined Bulk Piezoelectric Transducer, *IEEE Ultrasonics Symposium*, 2004
- [6] Z.L. Wang, Nanopiezotronics, *Advanced Materials*, vol. 19, 2007, pp 889-892
- [7] H. Zhang and S. Dong and S. Zhang and T. Wang and Z. Zhang and L. Fan, Ultrasonic Micro-motor using Miniature Piezoelectric Tube with Diameter of 1.0 mm, *Ultrasonics*, vol. 44, 2006, pp e603-e606
- [8] K. Uchino, Piezoelectric Ultrasonic Motors: Overview, *Smart Material Structures*, vol. 7, 1998, pp 273-285
- [9] D. Wajchman and D. Liu and J. Friend and L. Yeo, An Ultrasonic Piezoelectric Motor Utilising a Non-Circular Cross Sectioned Twisted Beam, *IEEE Transactions on Ultrasonics, Ferroelectrics and Frequency Control*, 2008, vol. 55, 2008, pp 832-840
- [10] J. Tsujino, Ultrasonic Motor Using a One-Dimensional Longitudinal-Torsional Vibration Converter with Diagonal Slits, *Smart Material Structures*, vol. 7, 1998, pp 345-351
- [11] K. Nakamura and M. Kurosawa and H. Kurebayashi and S. Ueha, An Estimation of Load Characteristics of an Ultrasonic Motor by Measuring Transient Responses, *IEEE Transactions on Ultrasonics, Ferroelectrics and Frequency Control*, vol. 38, 1991, pp 481-485
- [12] J. Friend and K. Nakamura and S. Ueha, A Torsional Transducer through In-Plane Shearing of Paired Planar Piezoelectric Elements, *IEEE Transactions on Ultrasonics, Ferroelectrics, and Frequency Control*, vol. 51, 2004, pp 870-877
- [13] B. Behkam and M. Sitti, Design Methodology for Biomimetic Propulsion of Miniature Swimming Robots, *ASME Journal of Dynamic Systems and Measurement Control*, vol. 128, pp 36-43
- [14] J.J.L. Higdon, The Hydrodynamics of Flagellar Propulsion: Helical Waves, *Journal of Fluid Mechanics*, vol. 94, 1978, pp 331-351
- [15] P.W. Rand and E. Lacombe and H.E. Hunt and W.H. Austin, Viscosity of normal human blood under normothermic and hypothermic conditions, *Journal of Applied Physiology*, vol. 19, 1964, pp 117-122
- [16] J. Happel, H. Brenner, *Low Reynolds Number Hydrodynamics*, Prentice Hall, Englewood Cliffs, NJ; 1965
- [17] T. Tanaka, C. Riva, I. Ben-Sira, Blood Velocity Measurements in Human Retinal Vessels, *Science*, vol. 186(4166), 1974, pp 830-831.
- [18] W.H. Wittrick, On Elastic Wave Propagation in Helical Springs, *International Journal of Mechanical Sciences*, vol. 8, 1966, pp 25-47



## Supplementary Material for Chapter 4

The paper reproduced in Chapter 4 refers to figures held in the supplementary material. These figures are reproduced below.

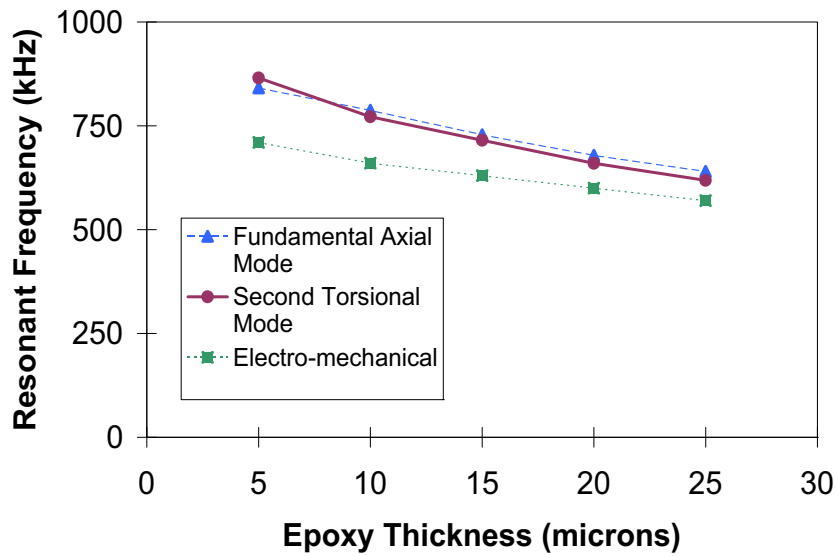


Figure S.1: The effect of the epoxy bond thickness on system resonant frequencies is generally disregarded in piezoelectric motor design. However, for the design in this paper we can see a significant effect on each of the resonances of interest.

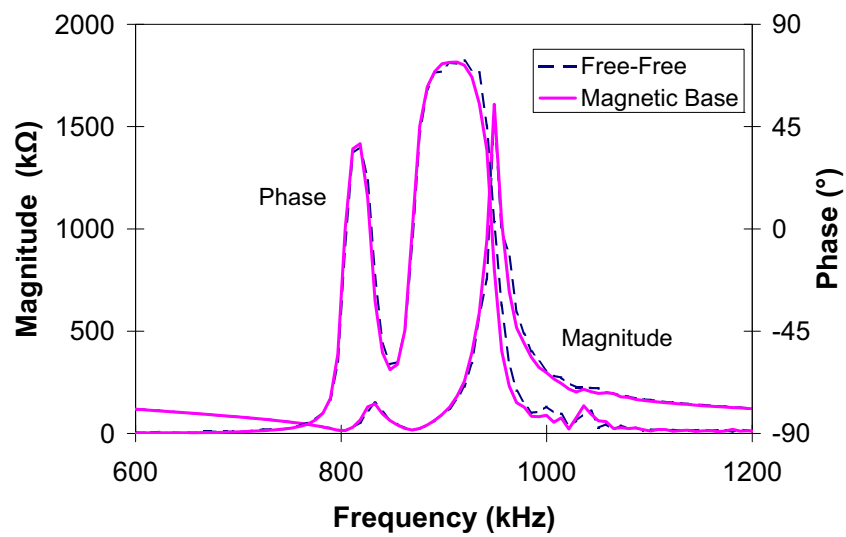


Figure S.2: Difference between the impedance magnitude and phase when comparing a motor test-piece mounted in a free-free configuration and that employing an additional magnetic element attracting the motor's magnetic element.

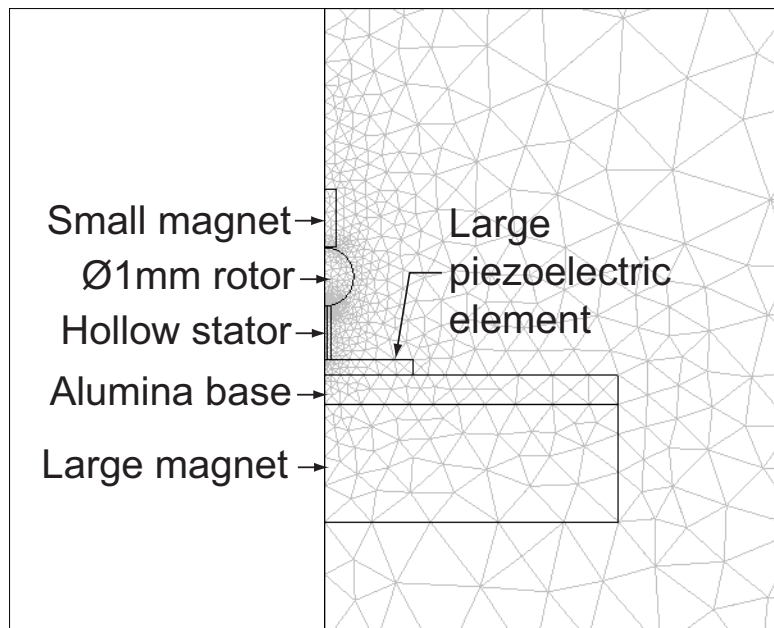


Figure S.3: The finite element model configuration for the preload model and validation.

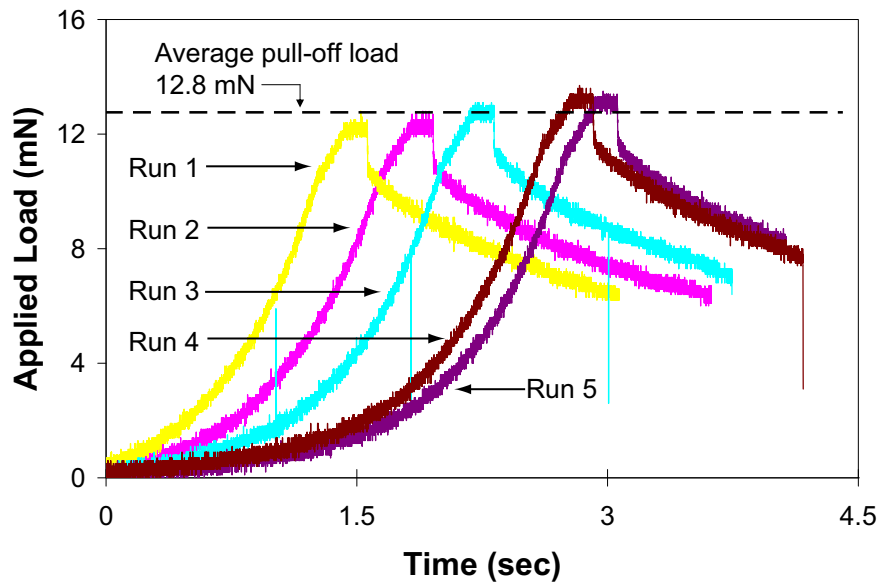


Figure S.4: Applied pull-off force for as a function of time. The peak pull-off load measured is the preload in the system.